Published in final edited form as:

*Geochim Cosmochim Acta*. 2019 September 1; 260: 133–160. doi:10.1016/j.gca.2019.06.023.

# Extended chondrule formation intervals in distinct physicochemical environments: Evidence from Al-Mg isotope systematics of CR chondrite chondrules with unaltered plagioclase.

**Travis J. Tenner**[1,2], **Daisuke Nakashima**[1,3], **Takayuki Ushikubo**[1,4], **Naotaka Tomioka**[4], **Makoto Kimura**[5,6], **Michael K. Weisberg**[7,8], **Noriko T. Kita**[1]

[1]WiscSIMS, Department of Geoscience, University of Wisconsin-Madison, Madison, WI 53706, USA.

[2]Chemistry Division, Nuclear and Radiochemistry, Los Alamos National Laboratory, MSJ514, Los Alamos, NM 87545, USA.

[3]Department of Earth and Planetary Material Sciences, Faculty of Science, Tohoku University, Aoba, Sendai, Miyagi 980-8578, Japan.

[4]Kochi Institute for Core Sample Research, Japan Agency for Marine-Earth Science and Technology (JAMSTEC), 200 Monobe Otsu, Nankoku, Kochi 783-8502, Japan.

[5]Faculty of Science, Ibaraki University, Mito 310-8512, Japan.

[6]National Institute of Polar Research, Tokyo 190-8518, Japan.

[7]Kingsborough Community College and Graduate Center, The City University of New York, 2001 Oriental Boulevard, Brooklyn, NY 11235-2398, USA.

[8]American Museum of Natural History, Central Park West at 79th Street, New York, NY, 10024-5192, USA.

## Abstract

Al-Mg isotope systematics of twelve FeO-poor (type I) chondrules from CR chondrites Queen Alexandra Range 99177 and Meteorite Hills 00426 were investigated by secondary ion mass spectrometry (SIMS). Five chondrules with Mg#'s of 99.0 to 99.2 and $\Delta^{17}$O of −4.2‰ to −5.3‰ have resolvable excess $^{26}$Mg. Their inferred $(^{26}\mathrm{Al}/^{27}\mathrm{Al})_0$ values range from $(3.5 \pm 1.3) \times 10^{-6}$ to $(6.0 \pm 3.9) \times 10^{-6}$. This corresponds to formation times of 2.2 (–0.5/+1.1) Myr to 2.8 (−0.3/+0.5) Myr after CAIs, using a canonical $(^{26}\mathrm{Al}/^{27}\mathrm{Al})_0$ of $5.23 \times 10^{-5}$, and assuming homogeneously distributed $^{26}$Al that yielded a uniform initial $^{26}\mathrm{Al}/^{27}\mathrm{Al}$ in the Solar System. Seven chondrules lack resolvable excess $^{26}$Mg. They have lower Mg#'s (94.2 to 98.7) and generally higher $\Delta^{17}$O (−0.9‰ to −4.9‰) than chondrules with resolvable excess $^{26}$Mg. Their inferred $(^{26}\mathrm{Al}/^{27}\mathrm{Al})_0$ upper limits range from $1.3 \times 10^{-6}$ to $3.2 \times 10^{-6}$, corresponding to formation >2.9 to >3.7 Myr after CAIs. Al-Mg isochrons depend critically on chondrule plagioclase, and several characteristics indicate the chondrule plagioclase is unaltered: (1) SIMS $^{27}\mathrm{Al}/^{24}\mathrm{Mg}$ depth profile patterns match those from anorthite standards, and SEM/EDS of chondrule SIMS pits show no foreign inclusions; (2) transmission electron microscopy (TEM) reveals no nanometer-scale micro-inclusions and no alteration due to thermal metamorphism; (3) oxygen isotopes of chondrule plagioclase match those of coexisting olivine and pyroxene, indicating a low extent of thermal metamorphism; and (4) electron microprobe data show chondrule plagioclase is anorthite-rich, with excess structural silica and high MgO, consistent with such plagioclase from other petrologic type 3.00–3.05 chondrites. We conclude that the resolvable $(^{26}Al/^{27}Al)_0$ variabilities among chondrules studied are robust, corresponding to a formation interval of at least 1.1 Myr.

Using relationships between chondrule $(^{26}Al/^{27}Al)_0$, Mg#, and $\Delta^{17}O$, we interpret spatial and temporal features of dust, gas, and $H_2O$ ice in the FeO-poor chondrule-forming environment. Mg# ≥ 99, $\Delta^{17}O$ ~−5‰ chondrules with resolvable excess $^{26}Mg$ initially formed in an environment that was relatively anhydrous, with a dust-to-gas ratio of ~100×. After these chondrules formed, we interpret a later influx of $^{16}O$-poor $H_2O$ ice into the environment, and that dust-to-gas ratios expanded (100× to 300×). This led to the later formation of more oxidized Mg# 94–99 chondrules with higher $\Delta^{17}O$ (−5‰ to –1‰), with low $(^{26}Al/^{27}Al)_0$, and hence no resolvable excess $^{26}Mg$.

We refine the mean CR chondrite chondrule formation age via mass balance, by considering that Mg# ≥ 99 chondrules generally have resolved positive $(^{26}Al/^{27}Al)_0$ and that Mg# < 99 chondrules generally have no resolvable excess $^{26}Mg$, implying lower $(^{26}Al/^{27}Al)_0$. We obtain a mean chondrule formation age of 3.8 ± 0.3 Myr after CAIs, which is consistent with Pb-Pb and Hf-W model ages of CR chondrite chondrule aggregates. Overall, this suggests most CR chondrite chondrules formed immediately before parent body accretion.

## 1. INTRODUCTION

The presence of $^{26}Al$ in the early Solar System (e.g. Lee et al., 1976) can be used to infer the relative ages of materials formed during that epoch. Extinct parent $^{26}Al$ is measured as excess daughter $^{26}Mg$ in early Solar System materials. As $^{26}Al$ has a half-life of 0.705 Myr (Norris et al., 1983) it is a well-resolved chronometer, assuming (1) $^{26}Al$ was homogeneously distributed in the Solar System prior to formation of materials of interest; and (2) there was no later addition of $^{26}Al$. Ca- and Al-rich inclusions (CAIs), chondrules, and achondrites have $^{26}Al$-$^{26}Mg$ systematics that are generally concordant with other isotope systems, including $^{207}Pb$-$^{206}Pb$, $^{53}Mn$-$^{53}Cr$, and $^{182}W$-$^{182}Hf$ (e.g. Jacobsen et al., 2008; Nyquist et al., 2009; Spivak-Birndorf et al., 2009; Amelin et al., 2002; 2010; Bouvier and Wadhwa, 2010; Schiller et al., 2010; 2015; Bouvier et al., 2011a; 2011b; Kleine et al., 2012; Kita et al., 2013; Wadhwa et al. 2014; Budde et al., 2016; 2018; Schrader et al., 2017 with some exceptions such as $^{53}Mn$-$^{53}Cr$ in some CAIs (e.g. Bogdanovski et al., 2002; Papanastassiou et al.; 2002; Nyquist et al., 2009). Among these materials, many CAIs have the highest inferred initial $^{26}Al/^{27}Al$, or $(^{26}Al/^{27}Al)_0$, with a canonical value of $\sim 5.2 \times 10^{-5}$ (e.g. Jacobsen et al., 2008; Larsen et al., 2011; MacPherson et al., 2010). As such, the canonical CAI $(^{26}Al/^{27}Al)_0$ serves to anchor the Al-Mg isotope system, and the agreement among multiple isotope systems from different types of early Solar System materials supports homogeneous $^{26}Al$ distribution when and after canonical CAIs formed (Kita et al., 2013 and references therein). However, this assumption is actively debated, mainly in two ways. The first considers homogeneous $^{26}Al$ distribution at the time of canonical CAIs, but that isotopically anomalous and $^{26}Al$-poor CAIs, with no evidence of disturbance from secondary processing, formed prior to homogeneous $^{26}Al$ distribution (e.g. Makide et al., 2013; Kuffmeier et al., 2016; Park et al., 2017). The second considers disk-wide $^{26}Al$

heterogeneity, based on inconsistencies between Pb-Pb ages and Al-Mg isotope systematics among some CAIs, chondrules, and achondrites (Larsen et al., 2011; Connelly et al., 2012; Schiller et al., 2015; Olsen et al., 2016; Van Kooten et al., 2016 Bollard et al., 2015; 2017). While recognizing the merits of both sides to this debate, we operate under the assumption that $^{26}$Al was homogeneously distributed after canonical CAI formation, and use the Al-Mg isotope system to calculate the age of chondrule formation relative to canonical CAIs.

Secondary ion mass spectrometry (SIMS) is a powerful analytical tool for early Solar System chronology, because it provides the ability to measure isotope ratios of small meteoritic components in-situ, with micron-scale resolution. Based on SIMS measurements, chondrules have lower ($^{26}$Al/$^{27}$Al)$_0$ than canonical CAIs, as those from the least metamorphosed chondrites, Acfer 094 (ungr. C3.00), Yamato 81020 (CO3.05), and Semarkona (LL3.01) (classifications: Kimura et al., 2008), have values ranging from $0.24 \times 10^{-5}$ to $1.6 \times 10^{-5}$ (Nagashima et al., 2018 and references therein; Fig. 1a). Using the aforementioned $^{26}$Al half-life and canonical ($^{26}$Al/$^{27}$Al)$_0$, these ($^{26}$Al/$^{27}$Al)$_0$ values correspond to formation ages of 1.2 to 3.1 Myr after CAIs, (Fig. 1b, shaded region). Among CO and Acfer 094 chondrites, FeO-poor chondrules with anorthite-rich plagioclase formed over an even narrower interval (mean relative age: 2.14 ± 0.27 [1SD] Myr after CAIs; Kurahashi et al., 2008a; Ushikubo et al., 2013). SIMS Al-Mg isotope systematics have also been measured in CR chondrite chondrules, and within analytical uncertainties approximately one-third (10 of 35) have resolvable excess $^{26}$Mg (Fig. 1b, solid symbols). Their inferred ($^{26}$Al/$^{27}$Al)$_0$ values are generally within the range of chondrules from Acfer 094, CO, and LL3 chondrites. However, roughly two-thirds (25 of 35) of CR chondrite chondrules studied have no resolvable excess $^{26}$Mg (e.g. Fig. 1b, open symbols). In particular, SIMS data from Nagashima et al. (2014) and Schrader et al. (2017) indicate that, when applying ($^{26}$Al/$^{27}$Al)$_0$ upper limits, several chondrules formed at least 0.5 Myr after those from Acfer 094, CO, and LL3 chondrites (Fig. 1b).

Among currently available data from CR chondrite chondrules, there appears to be no correlation between their Al-Mg isotope systematics and properties related to the physicochemical environment from which they formed (Schrader et al., 2017). This is an important consideration, because CR chondrite chondrules (1) have mass-independent fractionated oxygen isotope ratios; and (2) become systematically depleted in $^{16}$O as their Mg#'s decrease (where Mg# = mol.% MgO/[MgO + FeO] of chondrule ferromagnesian silicates) (Connolly and Huss, 2010; Tenner et al., 2015; Schrader et al., 2013, 2014a; 2017). As lower chondrule Mg#'s correspond to more oxidized formation environments, based on metal-silicate phase equilibria (e.g. Kring, 1988; Zanda et al., 1994; Ebel and Grossman 2000), Connolly and Huss (2010) suggested this Mg# versus oxygen isotope relationship was caused by variable proportions of $^{16}$O-depleted $H_2O$ ice (e.g. Sakamoto et al., 2007) and relatively $^{16}$O-rich material within chondrule precursors. Similar correlations of decreasing Mg#'s and $^{16}$O-depletion among chondrule populations are observed in other carbonaceous chondrites (e.g. Russell et al., 2010; Rudraswami et al., 2011; Ushikubo et al., 2012; Tenner et al., 2013; 2017; Chaumard et al., 2018; Hertwig et al., 2018; Yamanobe et al., 2018). Therefore, it is worthwhile to investigate further Al-Mg isotope systematics of CR chondrite chondrules with known Mg# and O-isotope signatures, to better understand if excess $^{26}$Mg, or the lack thereof, (1) was related to the abundance of $H_2O$ ice within the CR chondrite chondrule-forming environment, and (2) indicates timing similarities and/or differences to other chondrite chondrule-forming environments.

In order to use Al-Mg isotope systematics of early Solar System materials for chronology, well-defined internal isochrons should be established by plotting $^{27}Al/^{24}Mg$ versus excess $^{26}Mg$ (i.e. $\delta^{26}Mg^*$; defined in Section 2.5) with a large range of $^{27}Al/^{24}Mg$ ratios, where the slope corresponds to $(^{26}Al/^{27}Al)_0$ (e.g. Fig. 1a). A caveat of this approach for chondrules is that their isochrons depend almost solely on measurements of glassy mesostasis or plagioclase, which are the only constituent phases with sufficient $^{27}Al/^{24}Mg$ to resolve excess $^{26}Mg$ (olivine and pyroxene Al-Mg isotope systematics define the end at the origin). It is uncommon that glass and plagioclase coexist within a single chondrule. Glass and plagioclase often do not have large ranges of $^{27}Al/^{24}Mg$ ratios within a single chondrule, meaning isochron regressions are made based nearly on a “two-point line”. Therefore, any problems related to the closure of the glass or plagioclase isotope decay system will compromise chondrule isochrons. This is evident among thermally metamorphosed, petrologic type ≥3.2 chondrites, where chondrule plagioclase or glass data with significantly high $^{27}Al/^{24}Mg$ (>100) and with limited-to-no excess $^{26}Mg$ (e.g. Huss et al., 2001; Kita et al., 2004a; 2004b) are interpreted as representing a late disturbance of the Al-Mg isotope system. Furthermore, if only considering chondrule plagioclase or glass with excess $^{26}Mg$, such data by themselves are often as consistent with a horizontal line as they are with an isochron. As pointed out by Alexander and Ebel (2012), a horizontal line would indicate a late disturbance (after all $^{26}Al$ decayed) that modified Al/Mg ratios and/or re-equilibrated Mg isotopes in glass or plagioclase. Thus, although Al-Mg isotope systematics of chondrules from petrologic type ~3.0 chondrites are considered robust (e.g. Kita and Ushikubo, 2012), more critical assessments pertaining to the reliability of plagioclase or glass data used for chondrule chronology are beneficial.

Here, we present SIMS Al-Mg isotope systematics of chondrules from Queen Alexandra Range (QUE) 99177 and Meteorite Hills (MET) 00426, which are two of the least altered CR chondrites (petrologic type 2.6 to 3.0; Abreu and Brearley, 2010; Alexander et al., 2013; Harju et al., 2014; Howard et al., 2015). For all chondrules studied, their O-isotope ratios and Mg#’s were previously determined (Tenner et al., 2015), allowing for comparisons to their Al-Mg isotope systematics. We also investigated several attributes of chondrule plagioclase, including elemental relationships, Raman spectra, and characterization by focused ion beam/transmission electron microscopy (FIB/TEM), to determine its reliability with respect to closure of the $^{26}Al$-$^{26}Mg$ decay system.

## 2. SAMPLES AND METHODS

Twelve chondrules, Q7, Q13, Q15, Q16, Q19, Q35, Q36, Q38, Q44, M3, M6, and M23 (as labeled in Tenner et al., 2015) were investigated for SIMS Al-Mg isotope systematics, from thin sections QUE 99177,49 and MET 00426,46. These chondrules were chosen because they have several regions of plagioclase that could be analyzed with 5–10 μm SIMS spot sizes, and cover an appreciable range of O-isotope ratios. Their chondrule Mg#’s range from 94.2 to 99.2, and their $\Delta^{17}O$ values range from –0.9‰ to –5.3‰ (where $\Delta^{17}O = \delta^{17}O - 0.52 \times \delta^{18}O$; $\delta^{17,18}O = [(R_{sample}/R_{VSMOW}) - 1] \times 1000$; $R = {}^{17,18}O/^{16}O$; and VSMOW = Vienna

Standard Mean Ocean Water; Baertschi, 1976). All chondrules studied are within 0.8‰ of the slope-1 $\delta^{18}$O versus $\delta^{17}$O primitive chondrule mineral (PCM) line defined by Acfer 094 chondrule phenocrysts (Ushikubo et al., 2012). Chondrules Q13 and Q36 have compound textures (barred olivine interiors surrounded by porphyritic exteriors), and chondrule Q15 is layered, with a porphyritic texture but containing smaller chondrules along the periphery. The other chondrules have porphyritic textures (Fig. 2). In addition to the chondrules described above, plagioclase from a single Acfer 094 chondrule, G15 (as labeled in Ushikubo et al., 2012), was evaluated by transmission electron microscopy (TEM; described below), for comparison to plagioclase from CR chondrite chondrules.

### 2.1. Scanning electron microscopy

Backscattered electron (BSE) images of chondrule olivine, pyroxene and plagioclase were collected with a Hitachi S-3400 N SEM equipped with an energy dispersive X-ray spectrometer (EDS). Minerals that were free of cracks, inclusions, and pits, and that could accommodate a 5−15 μm SIMS spot analysis were identified as regions of interest.

### 2.2. Electron microprobe analysis

Prior to SIMS, major element oxide compositions ($SiO_2$, $TiO_2$, $Al_2O_3$, $Cr_2O_3$, FeO, MnO, MgO, CaO, $Na_2O$, and $K_2O$) of chondrule silicate minerals were measured by electron probe microanalysis (EPMA) using a Cameca SX-51 instrument at the University of Wisconsin-Madison. Operating conditions included a 15 kV accelerating voltage, a 10 nA beam current, a 1–2 μm diameter beam, and peak and background count times of 10 and 5 seconds, respectively. Standards were olivine ($Fo_{0,}$ $Fo_{83,}$ $Fo_{89,}$ $Fo_{100}$), pyroxene (enstatite, diopside, wollastonite, augite, jadeite, and omphacite), plagioclase ($An_{0,}$ $An_{18,}$ $An_{49,}$ $An_{67,}$ $An_{78,}$ $An_{95}$), rutile, hornblende, chromite, hematite, tephroite, and microcline. Carbon coat thicknesses of standards and thin sections were ~20 nm (indigo red on polished brass; Kerrick et al., 1970). Using a φ(ρZ) matrix correction, data were reduced with Probe for Windows software. Detection limits (99% confidence) were 0.06, 0.05, 0.05, 0.06, 0.09, 0.08, 0.05, 0.04, 0.05, and 0.03 wt.%, for respective oxides listed above. Olivine and pyroxene data are reported in Tenner et al. (2015). For plagioclase, Na count rates were monitored using albite-rich standards and no appreciable decrease was observed. Plagioclase standards were intermittently analyzed as unknowns, to ensure appropriate totals were achieved (99–101 wt.%), and to verify cations were within 0.01 units of their known stoichiometry (Table 1). For all plagioclase data (Table 1; Appendix EA1), endmembers, including $Ca(Fe,Mg)Si_3O_8$, $KAlSi_3O_8$, $NaAlSi_3O_8$, $CaAl_2Si_2O_8$, $(Fe,Mg)Al_2Si_2O_8$, and $[\ ]Si_4O_8$, are calculated using methods described in Beaty and Albee (1980).

### 2.3. Raman spectroscopy of chondrule plagioclase

Structural characteristics of chondrule plagioclase were determined by laser micro-Raman spectroscopy, using a Renishaw inVia spectrometer and a JASCO spectrometer at the National Institute of Polar Research (NIPR) in Japan. A microscope focused the excitation laser beam (532 nm) to a 2 micron spot size, and 200 to 1400 $cm^{-1}$ Raman spectra were acquired.

### 2.4. Transmission electron microscopy of chondrule plagioclase

Regions of chondrule plagioclase were investigated by transmission electron microscopy (TEM) at the Kochi Institute for Core Sample Research, JAMSTEC. Samples were processed into thin films by a $Ga^+$-ion beam after deposition of carbon protection layers in a focused ion beam apparatus (FIB: Hitachi SMI4050). The films (~150 nm in thickness) were mounted onto Cu grids by carbon deposition and were positioned with a FIB-equipped micro-manipulator. The TEM instrument (JEOL JEM-ARM200F) operated at an accelerating voltage of 200 kV, and samples were characterized with bright-field transmission electron imaging and by high-angle annular dark field scanning transmission electron imaging (HAADF-STEM). Crystal structures were identified using selected area electron diffraction (SAED). Chemical compositions of the samples were obtained by EDS with a 100 $mm^2$ silicon-drift detector in STEM mode.

### 2.5. Secondary ion mass spectrometry

Among chondrule minerals, the three stable isotopes of Mg, as well as $^{27}Al/^{24}Mg$ ratios, were measured by SIMS, using the WiscSIMS Cameca IMS 1280. Analytical conditions are similar to those reported by Ushikubo et al. (2013). A primary $O^-$ beam sputtered samples to detect secondary $Mg^+$ and $Al^+$ ions by applying −13kV and +10KV primary and secondary voltages, respectively. Secondary ions were aligned with a transfer lens magnification of 200×, and with a coupling lens operating in circular mode. The entrance slit width was 90 μm. As detailed below, other settings depended on appropriate conditions for the analysis of mafic minerals (olivine and pyroxene) versus plagioclase, as they have different secondary $Mg^+$ ion intensities. Reduction of SIMS Al-Mg isotope data is similar to methods reported in Ushikubo et al. (2017).

**2.5.1. Multi-Faraday cup analyses of olivine and low-Ca pyroxene—**Olivine and pyroxene were analyzed in a single session. Analyses employed a ~10 μm spot size with a primary beam intensity of ~2.5 nA. Secondary $^{24}Mg^+$, $^{25}Mg^+$, $^{26}Mg^+$, and $^{27}Al^+$ ions were counted simultaneously with four Faraday cups, with an exit slit width of 500 μm. All Faraday cups employed $10^{11}$ Ohm feedback resistors, and $^{24}Mg^+$ count rates for olivine and pyroxene ranged from 1.7 to $2.1 \times 10^8$ cps. Each analysis duration was approximately 10 minutes. The mass resolving power at 10% peak height was ~2500. Contributions from $^{48}Ca^{2+}$ and $^{24}MgH^+$ to $^{24}Mg^+$ and $^{25}Mg^+$ peaks, respectively, were less than 0.01‰. Terrestrial reference $^{25}Mg/^{24}Mg$ and $^{26}Mg/^{24}Mg$ values (0.12663 and 0.13932, respectively; Catanzaro et al., 1966) were used to convert measured (raw) ratios to delta notation ($\delta^{25}Mg_m$ and $\delta^{26}Mg_m$). For olivine, San Carlos ($Fo_{89}$) was used as the bracketing standard, and $Fo_{100}$ and $Fo_{60}$ standards were also measured; their respective $\delta^{25}Mg$ values on the DSM3 scale are –0.072‰ ± 0.089‰ (2SD), –0.366‰ ± 0.086‰, and –0.013‰ ± 0.062‰ (Kita et al., 2016). For low-Ca pyroxene, SP79–11 ($En_{97}$) was the bracketing standard and IG-Opx ($En_{89}$) was also measured; their $\delta^{25}Mg$ values on the DSM3 scale are –0.058‰ ± 0.055‰ (2SD) and –0.037‰ ± 0.079‰, respectively (Kita et al., 2016).

SIMS instrumental biases of olivine and pyroxene $\delta^{25}Mg$ were determined from measurements of standards listed above, and range from –3.6‰ to +0.5‰ (Tables EA2–1 and EA2–2). Repeated analyses of standards were reproducible within 0.1‰, and $\delta^{25}Mg$

biases increase with decreasing Fo and En endmembers, respectively (Figs. EA2–1 and EA2–2). For natural and instrumental mass dependent fractionations, we apply a power law function of 0.5128 from Davis et al. (2015). The mass independent term $\Delta^{26}$Mg is defined as $\Delta^{26}\mathrm{Mg} = [(1 + \delta^{26}\mathrm{Mg}/1000)/(1 + \delta^{25}\mathrm{Mg}/1000)^{1/\beta} - 1] \times 1000$, where $\beta = 0.5128$. SIMS measured $\Delta^{26}\mathrm{Mg}_m$ values of standards were consistently biased to slight positive values (~0.2‰; Table EA2–1; Table EA2–2), similar to those reported in Ushikubo et al. (2013; 2017). $\Delta^{26}$Mg values of unknowns were corrected for this bias, based on bracketing standard analyses. $\Delta^{26}$Mg uncertainties of unknown data are propagated, combining (1) the maximum of the bracketing standard 2SD versus the internal error of a single analysis (i.e. 2SE of 30 cycles per analysis), and (2) the bracketing standard 2SE. External reproducibilities (2SD) of $\Delta^{26}\mathrm{Mg}_m$ values for San Carlos olivine and Sp79–11 pyroxene bracketing analyses were 0.08–0.12‰ and 0.06–0.10‰, respectively ($n$: four brackets consisting of 8 analyses per bracket; Tables EA3–1 and EA3–2). Raw $^{27}\mathrm{Al}/^{24}\mathrm{Mg}$ ratios of chondrule olivine and pyroxene were corrected by applying a SIMS relative sensitivity factor RSF= $[(^{27}\mathrm{Al}/^{24}\mathrm{Mg}_m)/[(^{27}\mathrm{Al}/^{24}\mathrm{Mg}_{true})]$ of 0.87, which was based on repeated measurements of SP79–11 reference pyroxene (Table EA3–2). We apply a conservative 10% uncertainty to RSF-corrected chondrule olivine and pyroxene $^{27}\mathrm{Al}/^{24}\mathrm{Mg}$ values (which is approximately an order of magnitude larger than the 2SE uncertainty of raw $^{27}\mathrm{Al}/^{24}\mathrm{Mg}$ values; Tables EA3–1 and EA3–2), particularly because olivine may not have the same RSF as pyroxene; in absolute terms this uncertainty is small, as RSF-corrected chondrule olivine and pyroxene $^{27}\mathrm{Al}/^{24}\mathrm{Mg}$ values range from 0.0003 to 0.0742.

For analyses of olivine in chondrules, we observe that their SIMS $^{24}$Mg yields (1) are approximately 5 to 10% higher than those of terrestrial standards with similar Fo contents (Fig. EA3–1a); and (2) are systematically higher than terrestrial standards as a function of $\delta^{25}\mathrm{Mg}_m$ (Fig. EA3–1b). This suggests a matrix effect in chondrule olivine analyses that is not properly corrected by analyses of terrestrial olivine reference materials. In the case of chondrule pyroxenes, their SIMS $^{24}$Mg yields are also slightly higher than those of terrestrial standards as a function of En and $\delta^{25}\mathrm{Mg}_m$ (Figs. EA3–2a and EA3–2b). As such, we do not employ instrumental bias corrected $\delta^{25}$Mg values for chondrule olivine and pyroxene. Instead, we make an assumption that their $\delta^{25}$Mg values are the same as the mean value of terrestrial igneous rocks (–0.13‰ DSM-3 scale; Teng et al., 2010; Hu et al., 2016) and we assign a conservative uncertainty of ±2‰ (Tables EA3–1 and EA3–2); for reference, this uncertainty corresponds to a maximum added error of 0.0005‰ to the $\delta^{26}$Mg* data from chondrule olivine and pyroxene. Under this assumption, the excess $\delta^{26}$Mg* data from chondrule olivine and pyroxene are indistinguishable from their $\Delta^{26}$Mg values because of the formula; $\delta^{26}\mathrm{Mg}^* = [(1+ \delta^{26}\mathrm{Mg}/1000) - (1 + \delta^{25}\mathrm{Mg}/1000)^{1/\beta}] \times 1000 = \Delta^{26}\mathrm{Mg} \times (1 + \delta^{25}\mathrm{Mg}/1000)^{1/\beta}$.

After analyses, SIMS pits were investigated by SEM. Some show evidence of overlapping small cracks, pinholes, or slivers of an FeO-rich phase (Appendix EA4). However, EDS of the cracks and pinholes gave the same spectra as the olivine or low-Ca pyroxene targeted, suggesting no foreign phase(s) present. Per chondrule, isotope data from SIMS pits with cracks, pinholes or FeO-rich phases are indistinguishable relative to data from pits that appear clean; therefore, such data are not excluded from isochrons.

**2.5.2. Plagioclase analyses—**Mg-isotopes and $^{27}Al/^{24}Mg$ ratios of chondrule plagioclase were collected in three sessions. A primary beam intensity of 20–100 pA was employed, corresponding to spot sizes (5–10 microns in diameter) that could accommodate the small regions of chondrule plagioclase. As a result of the low primary beam current, it was necessary to count for ~3.5 hours per analysis for desired analytical precision. A 50 µm diameter mass aperture was used along with a 100 µm beam aperture, to project a Köhler-illuminated 5 µm diameter spot with sharp edges onto the sample surface (i.e. 0.1× magnification). However, spot analysis diameters gradually increased to 10 µm or more within 2–3 days, due to continuous sputter-enlargement of the mass aperture hole. In our final session, we used a custom mass aperture strip that was thicker (75 µm-thick molybdenum, versus the standard 25 µm-thickness), which decelerated sputter-enlargement of the mass aperture hole, keeping spot analysis diameters between 5 and 8 µm over a 7 day period. We note there were no systematic effects on the instrumental bias or RSF due to (1) variability in the primary beam current, and (2) sputter enlargement of the mass aperture hole. The mass resolving power was set to 4000, allowing for separating $^{24}Mg^+$ and $^{25}Mg^+$ peaks from $^{48}Ca^{2+}$ and $^{24}Mg^1H^+$ interferences, respectively. Secondary $Mg^+$ ions were detected by an axial electron multiplier (EM) that operated by peak jumping. During measurement of $^{25}Mg^+$, secondary $^{27}Al^+$ ions were simultaneously collected by a Faraday cup located on the high-mass side of the axial EM. All analyses were corrected for a 23 ns EM dead time. Count rates for $^{24}Mg^+$ ranged from $2.0 \times 10^4$ to $1.2 \times 10^5$ cps. Count durations per cycle were as follows: for $^{24}Mg^+$ it was 3 seconds, and for $^{25}Mg^+$, $^{26}Mg^+$, and $^{27}Al^+$ the durations were each 10 seconds. Cycles per analysis were either 300 (first two sessions) or 400 (the third session).

Data reduction for plagioclase Al-Mg isotopes are similar to those for olivine and pyroxene described above. Instrumental bias was determined by measuring Mg isotope ratios and $^{27}Al/^{24}Mg$ from three synthetic anorthite glasses with 0.1, 0.6 and 1 wt.% MgO; each have a $\delta^{25}Mg$ of –1.77‰ (DSM3 scale; Kita et al., 2012). Based on measurements of the 1 wt. % MgO anorthite glass used as the running standard, the relative sensitivity factor for each session was constant, with a value of 1.04 (Table EA2–3), and external reproducibilities (2SD) of $\delta^{25}Mg_m$ and $\Delta^{26}Mg_m$ ranged from 0.77‰ to 1.09‰ and 0.70‰ to 0.99‰, respectively, similar to internal errors. The $\delta^{25}Mg_m$ and $\Delta^{26}Mg_m$ grand averages from running standard measurements were determined for each session; their uncertainties ($2SE_{std}$; standard error of the mean), ±0.19‰ to ±0.32‰, and ±0.13‰ to ±0.32‰, respectively, were used to correct unknown data (Table EA2–3). For unknowns, uncertainties are calculated as $[(2SE_{internal})^2 + (2SE_{std})^2]^{1/2}$ for $\delta^{25}Mg$ and $2SE_{internal}$ for $\delta^{26}Mg^*$, where $2SE_{internal}$ is the internal error of an individual unknown analysis.

Plagioclase $^{24}Mg$ signal stability was monitored by plotting $^{27}Al/^{24}Mg$ versus cycle number (e.g. Fig. 3). For reference glasses, $^{27}Al/^{24}Mg$ changed systematically over the first 30 cycles and then stabilized for the remainder of cycles, which could reflect implantation of oxygen ions from the primary beam into the sample matrix. In most cases, such depth profile patterns among unknowns matched those produced in anorthite glass running standards (e.g. Figs. 3a–3c), suggesting (1) chondrule plagioclase was the only phase analyzed; and (2) Mg concentrations were homogeneous within the volume analyzed. However, three of the 60 plagioclase analyses, two from chondrule Q36 and one from chondrule M23, had cycles removed because the measurements inadvertently profiled into high-Ca pyroxene grains. This was easily distinguishable, because when such a grain became part of the spot analysis the $^{27}$Al/$^{24}$Mg ratio dropped precipitously over the course of a few cycles; the presence of such grains was also verified by SEM imaging of the sputtered analysis area (e.g. Fig. 3d). We removed cycles with anomalously low $^{27}$Al/$^{24}$Mg, as it is possible the increased $^{24}$Mg signal from high-Ca pyroxene could cause inaccurate EM dead time corrections or lead to quasi-simultaneous arrival (QSA) effects that would compromise the accuracy of Mg isotope ratios. We note that a reduced number of cycles may cause changes to the $^{27}$Al/$^{24}$Mg relative sensitivity factor, and we did not account for this because our correction scheme uses the grand averaged $^{27}$Al/$^{24}$Mg values of all running standards for a given session. However, we evaluated this effect by reducing the cycle numbers of standards that bracketed shortened unknown analyses (to the same number of cycles as the shortened unknown analyses), and find that (1) changes to the bracketing standard analysis $^{27}$Al/$^{24}$Mg RSF values are small (–0.002 to +0.012), and that therefore (2) changes to the grand averaged $^{27}$Al/$^{24}$Mg RSF changes are minimal (max: 0.003). We also note that depth profile patterns from SIMS pits containing FeO-rich veins are not systematically different than those from SIMS pits without such veins; e.g., in Fig. 3c, the relatively flat $^{27}$Al/$^{24}$Mg pattern after the first 100 cycles most likely reflects natural variability observed in chondrule M23 plagioclase.

Following analytical sessions SIMS pits were evaluated by SEM and EDS. Most SIMS pits reveal only plagioclase was analyzed (e.g. image affiliated with Fig. 3b; Appendix EA4). In several cases SIMS pits show that they overlapped thin bands of an FeO-rich phase, but this did not diminish the quality of $^{27}$Al/$^{24}$Mg monitored during cycles (e.g. Fig 3c; Appendix EA4). Therefore, such data were not excluded. In chondrules Q36 and M23, EDS confirmed small grains of high-Ca pyroxene were present in three SIMS pits from analyses with anomalously low $^{27}$Al/$^{24}$Mg cycle values (e.g. image affiliated with Fig. 3d; Appendix EA4).

**2.5.3. Chondrule isochrons and relative ages—**$^{27}$Al/$^{24}$Mg (x-axis) versus $\delta^{26}$Mg* (y-axis) values of chondrules were used to construct $^{26}$Al-$^{26}$Mg isochrons with Isoplot 3.00 (Ludwig, 2003). All isochrons employed a model 1 fit. For each chondrule, $(^{26}\mathrm{Al}/^{27}\mathrm{Al})_0$ values and their uncertainties (95% confidence) are inferred from the slope of the isochron regression. Specifically, $(^{26}\mathrm{Al}/^{27}\mathrm{Al})_0$ = slope × 0.13932/1000, where 0.13932 is the terrestrial reference $^{26}$Mg/$^{24}$Mg value (Catanzaro et al., 1966). Relative ages are calculated as:

$$\Delta t(\mathrm{Myr}) = \ln\left[\left(\frac{^{26}\mathrm{Al}}{^{27}\mathrm{Al}}\right)_{0;\ \mathrm{CAI}} \Big/ \left(\frac{^{26}\mathrm{Al}}{^{27}\mathrm{Al}}\right)_{0;\ \mathrm{chondrule}}\right] \times \frac{0.705}{\ln(2)} \qquad (1)$$

using the canonical CAI $(^{26}\mathrm{Al}/^{0027}\mathrm{Al})_0$ of $5.23 \times 10^{-5}$ (Jacobsen et al., 2008; MacPherson et al., 2010), and where 0.705 is the half-life (in Myr) of $^{26}$Al (Norris et al., 1983). Relative age uncertainties also employ eqn. 1, using slopes of isochron error envelopes that represent upper and lower age limits.

# 3. RESULTS

## 3.1. Plagioclase electron microprobe and Raman spectroscopy results

Chondrule plagioclase electron microprobe data are given in Table 1. Averaged anorthite contents range from 81 to 99. MgO concentrations range from 0.5 to 1.4 wt.%. Oxide totals range from 99.5 to 100.5 wt.%. However, cation totals, normalized to 8 oxygens, are generally low; ten of twelve chondrules have plagioclase with cation values between 4.92 and 4.97, and two chondrules have plagioclase with cation totals of 4.987 and 5.011. These results occur even though measurements of $An_{78}$ and $An_{95}$ standards within the same sessions have appropriate oxide totals and have stoichiometric values between 4.994 and 5.001 (Table 1). According to Beaty and Albee (1980), plagioclase EPMA data with element totals at/near 100%, but with too much Si, too little Al, and low amounts of singly and doubly charged cations (e.g. Ca, Na, K), indicate the presence of a $[\ ]Si_4O_8$ endmember component, consisting of a vacancy and excess silica. The “excess silica” component comprises up to 8% of the endmember composition of QUE 99177 and MET 00426 plagioclase studied (Table 1).

Raman spectra from chondrule plagioclase show prominent peaks at 484 and 503 $cm^{-1}$ (Appendix EA5). In many scans peaks at 281, 400, 427, 553, 681, 756, and 974 $cm^{-1}$ are also present. These peaks are consistent with crystalline anorthite (Matson et al., 1986), and are not indicative of polymorphs such as dmisteinbergite. Chondrule Q38 plagioclase has an additional peak near 1020 $cm^{-1}$, consistent with pyroxene (Appendix EA5).

## 3.2. SIMS Al-Mg isotope systematics

Chondrule Al-Mg isotope data are given in Table 2. Chondrule isochrons are shown in Fig. 4. $^{27}Al/^{24}Mg$ ratios of olivine and low-Ca pyroxene range from 0.0003 to 0.0742. Their $\delta^{26}Mg^*$ values range from −0.07‰ to 0.13‰, with typical 2SE uncertainties of ~0.1‰. Olivine and low-Ca pyroxene data have no resolvable deficiencies in $\delta^{26}Mg^*$ relative to terrestrial standard values. Based on these characteristics, olivine and pyroxene data represent origins of chondrule isochrons. The measured $\delta^{26}Mg^*$ values of chondrule plagioclase range from −1.3‰ to 2.0‰, with typical 2SE uncertainties of ~1‰. Their $^{27}Al/^{24}Mg$ ratios are between 24.8 and 62.2 (Table 2), consistent with CR type I chondrule plagioclase in previous studies, but lower than Al-rich and type II chondrules, with values that can exceed 250 (Hutcheon et al., 2009; Nagashima et al., 2014; Schrader et al., 2017). Per chondrule, measured plagioclase $^{27}Al/^{24}Mg$ ratios do not significantly vary; in chondrules Q7 and M3 the ranges are ~9 and ~13 units, respectively, and in the other chondrules the ranges are 8 units or less (Table 2). When available, plagioclase Al/Mg ratios by EPMA and SIMS at the same locations generally match (Fig. 5). Two data points with the highest Al/Mg ratios in Fig 5, both from chondrule M3, have higher values by EPMA when compared to those by SIMS. This could reflect variability in the Al/Mg of chondrule M3 plagioclase that was sampled by the EPMA interaction volume, but was not sampled by the shallower depth of SIMS analyses.

Chondrule mineral isochrons have mean square weighted deviations (MSWD) of 0.2 to 2.1, below the threshold value of 2.5 for rejecting straight-line isochrons, according to Brooks et al. (1972). Five of twelve chondrules, Q7, Q16, Q38, M6, and M23, have resolvable excess $^{26}$Mg, with ($^{26}$Al/$^{27}$Al)$_0$ values of (3.5 ± 1.3) × $10^{-6}$ to (6.0 ± 3.9) × $10^{-6}$ (Fig. 4; Table 2). Including uncertainties, this corresponds to their formation 1.7 to 3.3 Myr after CAIs (eqn. 1). These chondrules have Mg#'s ranging from 99.0 to 99.2, and have a narrow range of $\Delta^{17}$O, from –4.2‰ to –5.3‰ (Table 2). The other seven chondrules, Q13, Q15, Q19, Q35, Q36, Q44, and M3, lack resolvable excess $^{26}$Mg. Using maxima of isochron uncertainties, their ($^{26}$Al/$^{27}$Al)$_0$ upper limits range from 1.3 × $10^{-6}$ to 3.2 × $10^{-6}$, corresponding to their formation >2.9 to >3.7 Myr after CAIs (eqn. 1). These chondrules have lower Mg#'s (94.2 to 98.7) and generally higher $\Delta^{17}$O values (–0.9 to –4.9‰), relative to chondrules with excess $^{26}$Mg (Table 2). The total range of ($^{26}$Al/$^{27}$Al)$_0$ generally agrees with prior CR chondrite chondrule data (e.g. Fig. 1b).

### 3.3 Plagioclase TEM results

After SIMS, two chondrules, one with resolvable excess $^{26}$Mg, M6, and one with no resolvable excess $^{26}$Mg, Q44, were selected for analysis by FIB sectioning and TEM (Figs. 6 and 7, respectively). Each chondrule has plagioclase with a resolvable [ ]$Si_4O_8$ endmember component (Table 1), meaning TEM analysis provides information regarding the nature of excess Si in chondrule plagioclase. For comparison to a sample with minimum thermal/aqueous metamorphism, a third FIB section was made from Acfer 094 chondrule plagioclase (chondrule G15, as labeled in Ushikubo et al., 2012), and was analyzed by TEM (Appendix EA6). This plagioclase also has a resolvable [ ]$Si_4O_8$ endmember component (Appendix EA1), and has resolvable excess $^{26}$Mg (Ushikubo et al. 2013).

The FIB section of M6 plagioclase (Figs. 6a & 6b) is a single crystal, based on thin-foil TEM imaging (Fig. 6c). HAADF-STEM Z-contrast imaging (e.g. Fig. 6d) shows chemical homogeneity (as does EDS mapping; Appendix EA6). SAED reveals a pattern consisting only of an unmodified anorthite structure, with no superlattice reflections (Fig, 6e). High-resolution TEM shows no inclusions down to the nanometer-scale (Fig 6f). These features are consistent with those from the Acfer 094 chondrule plagioclase FIB section (Appendix EA6).

The Q44 FIB section (Figs. 7a & 7b) consists of plagioclase and low-Ca pyroxene, based on TEM imaging (Fig. 7c) and EDS analysis. The plagioclase has two domains divided by a subgrain boundary consisting of dislocation arrays (e.g. dashed line with arrow in Fig 7c). Plagioclase domain 1 in Fig. 7c has a small number of free dislocations (circled regions in Fig. 7c), and a weathering vein was identified (Appendix EA6). Plagioclase domain 2 has no defect structures (Fig. 7c). HAADF-STEM Z-contrast imaging shows both plagioclase domains are chemically homogeneous, although domain 1 has a number of sub-micron sized inclusions, appearing as tiny bright dots (circled areas in Fig. 7d). For both plagioclase domains, SAED patterns consist only an of unmodified anorthite structure, with no superlattice reflections (e.g. Fig. 7e). High-resolution TEM imaging shows dislocation-free regions of plagioclase are devoid of inclusions (e.g. Figs. 7f & 7g) down to the nanometer scale. In plagioclase domain 1, 10-to-20 nm-sized inclusions are associated with dislocations (e.g. Fig. 7f). EDS analyses of these inclusions indicate a phase enriched in Fe, Cr, and Si. Due to their small size, EDS spectra of the inclusions partially sample host anorthite

(Appendix EA6), making it difficult to properly identify the phase. Excluding the sparse dislocations and inclusions, the near-entirety of plagioclase in the Q44 FIB section has features consistent with M6 (e.g. Fig. 6) and Acfer 094 chondrule plagioclase (e.g. Appendix EA6).

# 4. DISCUSSION

## 4.1. Assessing the reliability of plagioclase used for Al-Mg isotope systematics.

The most important consideration of this work involves a critical evaluation of the mineralogical and chemical characteristics of plagioclase used for Al-Mg isochrons, in order to ensure the chronometer is valid. For CR chondrite chondrules this is especially important because the majority of their constituent plagioclase has no resolvable excess $^{26}$Mg (Fig 1b; Fig. 4). Therefore, it is necessary to confirm that unresolved plagioclase isochrons do not reflect later secondary processing, but are instead true signatures of later chondrule formation. In this regard, we find that QUE 99177 and MET 00426 chondrule plagioclase show no evidence of secondary processing, and phases other than plagioclase were largely avoided during their analysis. Here, we detail these findings.

**4.1.1. Analyzed regions of chondrule plagioclase are free of inclusions and secondary alteration.—**Two lines of evidence indicate foreign mineral inclusions were avoided during SIMS analysis of chondrule plagioclase. First, SIMS depth profile patterns of $^{27}$Al/$^{24}$Mg are similar to those collected on the anorthite glass standard (e.g. Figs. 3a–3c). EDS revealed micron-scale high-Ca pyroxene grains in only 3 of 60 plagioclase SIMS pits (e.g. Fig. 3d), and isotope signals from related cycles were eliminated from Al-Mg isotope data. Second, TEM analysis indicates the plagioclase has few-to-no inclusions at the sub-micron level (Figs. 6 and 7). Although plagioclase in the Q44 FIB section has 10–20 nm-sized Fe,Cr,Si rich inclusions (e.g. Fig. 7f), their abundance is low and the inclusions lack Al and Mg, meaning they likely have a negligible influence on plagioclase Al-Mg isotope systematics. Additionally, the plagioclase FIB/TEM samples show no evidence of replacement by other mineral phases during aqueous/thermal metamorphism, down to the nanometer scale. Several plagioclase SIMS pits show evidence of partially sampling weathering veins of an FeO-rich phase (e.g. Appendix EA4: Q19: #1, #3; Q44: #3; M3: #3, #4; M6: #2, #3; M23: #2-#4). However, these data show no systematic differences in $^{27}$Al/$^{24}$Mg and $*\delta^{26}$Mg, relative to plagioclase analyses that did not sample FeO-rich veins (Table 2), suggesting the influence of FeO-rich weathering veins on data quality is minimal. Support for this interpretation comes from the observation that at least some veins are < 100 nm in width (e.g. Appendix EA6), meaning they likely represent a minimal volume of material sputtered during a SIMS analysis, when present.

**4.1.2. Chondrule intermineral O-isotope comparisons suggest plagioclase was not disturbed.—**Seven of twelve chondrules we investigated have SIMS O-isotope data of coexisting plagioclase, olivine, and pyroxene (from Tenner et al., 2015; Fig. 8). For each chondrule, plagioclase data are within 2‰ of coexisting olivine and pyroxene data on a three-oxygen isotope plot, and often the data overlap. This suggests that, for a given chondrule: (1) plagioclase, pyroxene, and olivine crystallized from a melt that remained nearly-constant in its O-isotope ratio; and (2) the plagioclase O-isotope ratio is unaltered. This second point is important because experimental data extrapolations predict 10 $\mu m^2$ of oxygen diffusion in anorthite occurs per 1 Myr at sustained temperatures of ~500 °C and ~150 °C during dry and hydrous thermal metamorphism, respectively (Fig. 9). Therefore, the per-chondrule O-isotope agreement between plagioclase and coexisting olivine and pyroxene among MET 00426 and QUE 99177 chondrules (e.g. Fig. 8) suggests the plagioclase experienced secondary heating extents of less than 150 °C on the presumably hydrated CR chondrite parent body (e.g. Schrader et al., 2014b). Although the susceptibility of oxygen and Mg isotope systems to disturbance are not related, at temperatures this low, Mg diffusion could also be negligible; however, experimental data for anorthite Mg diffusion in a wet system are currently lacking. In a dry system, Mg and oxygen diffusion rates in anorthite are similar for extrapolations below 1000 °C (Fig. 9), and so it is reasonable to speculate that if oxygen isotopes of chondrule plagioclase appear unaltered in a wet system, then Mg isotopes could also be unaltered. Further support for this hypothesis comes from Kaba (CV3.1) chondrites, as they experienced hydrothermal alteration at ~300 °C, and plagioclase is systematically $^{16}$O-depleted relative to coexisting phases in chondrules and CAIs (Krot et al., 2019). Yet, Al-Mg isotope systematics of Kaba chondrules appear undisturbed (Nagashima et al., 2017).

### 4.1.3. The importance of excess Si in plagioclase and other compositional relationships for evaluating the Al-Mg isotope systematics of chondrules.—

Ten of the twelve chondrules investigated have plagioclase with a resolvable excess silica ($[\ ]Si_4O_8$) component (Table 1). As data from $An_{78}$ and $An_{95}$ standards by EPMA are consistent with their reference compositions (Table 1), the measured excess silica in chondrule plagioclase is unlikely due to analytical error. Excess silica is common in anorthite-rich plagioclase from lunar basalts (Dymek et al., 1975; Longhi, 1976; Beaty et al., 1979; Baldridge et al., 1979; Appendix EA1), and was recently found in Pasamonte eucrite plagioclase (Mittlefehldt et al., 2017). According to 1 atm. experiments along the join $CaAl_2Si_2O_8$–$SiO_2$ (e.g. Longhi and Hays, 1979), excess silica is incorporated at high temperatures (~1100 to 1500 °C) and comprises up to several percent of the plagioclase endmember composition in a silica saturated system.

In addition to excess silica, we observe high anorthite contents (0.793 to 0.999, when normalized to anorthite, albite, and K-feldspar components), and appreciable MgO concentrations of 0.5 to 1.4 wt.%, within MET 00426 and QUE 99177 chondrule plagioclase (Table 1). Mg incorporation is most likely achieved by substitution involving the $Ca(Fe,Mg)Si_3O_8$ endmember (e.g. Longhi et al., 1976; Table 1). Collectively, similar plagioclase characteristics are reported among other FeO-poor CR chondrite chondrules (e.g. Nagashima et al., 2014; Schrader et al., 2017; Appendix EA1), and there are no systematic differences in excess silica, anorthite content or MgO, as a function of excess $^{26}$Mg abundance (Figs. 10a and 10b).

When comparing FeO-poor chondrule plagioclase from petrologic type <3.1 chondrites (less thermally metamorphosed) to those from petrologic type ≥3.1 chondrites (more thermally metamorphosed), there are distinct compositional differences. For example, Acfer 094 (ungr. C3.00) and L/LL 3.01–3.05 chondrites have FeO-poor chondrule plagioclase with similar ranges of excess silica, anorthite, and MgO as CR chondrite chondrules (Figs. 10c–10f). FeO-poor chondrule plagioclase from Yamato 81020 (CO3.05) has a slightly lower abundance of excess silica, on average (Fig. 10e), but otherwise has a similar range of MgO and anorthite content as that among CR chondrite chondrules (Fig. 10f). Thus, the combination of excess silica, high MgO and high anorthite content in FeO-poor chondrule plagioclase appears to be characteristic of petrologic type 3.00–3.05 chondrites, and of CR2 chondrites with minimal hydrothermal alteration. In contrast, FeO-poor chondrule plagioclase from type ≥3.1 chondrites, including those from CO, CV, and LL chondrites (Appendix EA1), have reduced proportions of excess silica, anorthite component, and MgO. In particular, data from 31 of 45 of such chondrules are silica deficient ($[\ ]Si_4O_8 < 0$), and the extent of deficiency becomes more pronounced as anorthite components decrease to values of ~0.7 (Fig. 10g). Further, plagioclase MgO concentrations from type ≥3.1 FeO-poor chondrite chondrules are low compared to those from type <3.1 chondrites, mainly ranging from 0 to 0.8 wt.%. (Fig. 10h). This feature could represent diminished Mg solubility in plagioclase during thermal metamorphism. Specifically, plagioclase Mg solubility is enhanced with increasing temperature (see Fig. 2 from Van Orman et al., 2014 and associated discussion), meaning it would have been at a maximum upon crystallization from the final chondrule melt (1150−1200 °C; Fig. 1 from Ustunisik et al., 2014). During thermal metamorphism of type ≥3.1 chondrites (e.g. 300−700 °C; Miyamoto, 1991; Huss and Lewis, 1994; Brearley, 1997) (1) plagioclase Mg solubility would have been reduced; and (2) plagioclase Mg diffusion would have been relatively fast (e.g. Fig. 9), meaning chondrule plagioclase may have lost a portion of Mg sequestered during primary crystallization.

Among type ≥3.1 chondrites, some regions of FeO-poor chondrule plagioclase are replaced by nepheline ($NaAlSiO_4$) (e.g. Fig. 1 from Krot et al. 2002; Fig. 4 from Tomeoka and Itoh 2004; Fig. 2 from Wick and Jones 2012; Fig. 3d from Nagashima et al., 2017). As nepheline is silica-poor relative to albite ($NaAlSi_3O_8$), we speculate that if EPMA measurements co-sampled plagioclase and nepheline, it could explain a trend of decreasing silica with apparently increasing albite component (i.e. decreasing anorthite component in Fig. 10g) among FeO-poor type ≥3.1 chondrite chondrules. The replacement of chondrule plagioclase by nepheline is commonly interpreted as a reaction product during thermal metamorphism (e.g. Kimura and Ikeda, 1995; 1997; 1998; Ichimura et al., 2017), and could explain disturbed Al-Mg isotope systematics among type ≥3.1 chondrite chondrules with this feature (e.g. Sano et al., 2014; Nagashima et al., 2017). Finally, we note that the extent of thermal metamorphism is often variable throughout a chondrite sample, meaning some FeO-poor chondrules with unaltered plagioclase may exist in type ≥3.1 chondrites. Importantly, electron microprobe analysis could identify such plagioclase based on the presence of excess silica, high MgO, and high anorthite content.

## 4.2. Chondrule formation in distinct environments I: Timing differences.

A key finding of this study is that chondrules with and without excess $^{26}Mg$ are distinguishable by Mg# and $\Delta^{17}O$. Those with excess $^{26}Mg$ have high Mg#'s (99.0 to 99.2), and a limited $\Delta^{17}O$ range (–4.2‰ to –5.3‰), while chondrules without excess $^{26}Mg$ have lower Mg#'s (94.2 to 98.7) and generally higher $\Delta^{17}O$ (–0.9 to –4.9‰) (Figs. 11a & 11b). This indicates two distinct physicochemical environments within the CR chondrite accretion region, and we can evaluate the chondrule-formation timing differences between these environments. If considering uncertainties, chondrule M23 has the oldest resolved age (2.2 −0.3/+0.4 Myr after CAIs; Table 2). If we compare the youngest possible formation age of chondrule M23 (2.6 Myr after CAIs) to the upper age limits of all chondrules without excess $^{26}$Mg (chondrules Q13, Q15, Q19, Q35, Q36, Q44, M3; Table 2), we determine resolved chondrule-formation timing differences of at least 0.3 to 1.1 Myr between the two environments. If we compare the oldest age (including uncertainties) from all chondrules with excess $^{26}$Mg (1.7 Myr after CAIs; chondrule Q38; Table 2) to the youngest upper age limit from all chondrules without excess $^{26}$Mg (>3.7 Myr after CAIs; chondrules Q15, Q36, and Q44; Table 2), chondrule-formation timing differences of more than 2.0 Myr may have existed between the two environments.

Kita and Ushikubo (2012) noted that, while many CR chondrite chondrules have lower $(^{26}Al/^{27}Al)_0$ than LL, CO, and Acfer 094 chondrules, with most lacking excess $^{26}$Mg (e.g. Fig. 1b), it was unknown if such isochrons were potentially influenced by aqueous alteration. Thus, our findings are important because we document that the chondrule plagioclase used for isochrons is unaltered (Section 4.1). This provides confidence that (1) some CR chondrite chondrules have resolvable timing differences exceeding 1 Myr (perhaps greater than 2 Myr), and that (2) at least some CR chondrite chondrules postdate those from LL, CO, and Acfer 094 chondrites by 1 to 2 Myr. Furthermore, the distribution of chondrule formation ages for a given type of chondrite may reflect the degree of local disk turbulence that controlled the time interval of parent body accretion. For example, Cuzzi et al. (2010) calculate that complete parent body accretion within 0.5 Myr would require no turbulence. LL, CO, and Acfer 094 parent bodies are consistent with this scenario based on the narrow standard deviations of their averaged chondrule ages (1SD: 0.4 Myr for each chondrite; Kita and Ushikubo, 2012). Such rapid accretion with no turbulence could explain why chondrules from LL, CO, and Acfer 094 chondrites cluster into discreet Mg# and O-isotope domains, as precursors may have been poorly mixed (e.g. Kita et al., 2010; Ushikubo et al., 2012; Tenner et al. 2013; we note that a small number of Acfer 094 chondrules have unique Mg#, oxygen isotope, and Al-Mg isotope relationships; Hertwig et al., 2019). In contrast, the longer duration of CR chondrite chondrule formation (> 1 million years) suggests a more turbulent environment, which extended the time for complete parent body accretion (e.g. Cuzzi et al., 2010). If true, then at least some CR chondrite chondrules could have formed after establishment of LL, CO, and Acfer 094 chondrite parent bodies. In turn, a more turbulent chondrule-forming environment could have fostered better mixing of solid precursors (e.g. dusts and ices) within the accretion region. This might explain why FeO-poor chondrules from CR chondrites show a continuous Mg# versus O-isotope trend (e.g. Fig 11b), as discussed below.

## 4.3. Chondrule formation in distinct environments II: Physicochemical characteristics.

**4.3.1 Redox conditions during chondrule formation: chondrule Mg# versus Al-Mg isotope systematics.—**By relating chondrule Mg#’s to their Al-Mg isotope systematics, redox conditions at the time of chondrule formation can be evaluated. Here, we report chondrule Mg#’s as defined in Tenner et al. (2015). From electron microprobe data per chondrule, average Mg#’s are calculated for olivine and for low-Ca pyroxene. If only one phase is analyzed, its average Mg# is defined as the chondrule Mg#. If both phases are analyzed, the averaged Mg#'s of each phase are weighted equally to define the chondrule Mg#. Chondrule Mg# uncertainties are reported as the range of all measured values. Although this definition does not account for modal abundances of olivine and low-Ca pyroxene within a chondrule (when both phases are present), it is observed among chondrites with petrologic types near 3.0, including QUE 99177 and MET 00426, that Mg#'s of coexisting olivine and low-Ca pyroxene are nearly identical per chondrule, typically differing by one unit or less (see Fig. 4 from Tenner et al., 2015 and associated references). Therefore, any additional uncertainty in chondrule Mg# stemming from olivine and low-Ca pyroxene modal abundances is likely minimal. Using defined chondrule Mg#'s, redox conditions are determined according to a regression constrained by equilibrium thermodynamic models (Ebel and Grossman, 2000; Fedkin and Grossman, 2006; Grossman et al., 2008):

$$\text{chondrule Mg\#} = 100 - \exp(([\log f\mathrm{O}_2 - \log \mathrm{IW}] + 3.444)/0.6649 \tag{2}$$

where IW is the Fe-wüstite buffer. Full details of Eqn. 2 are provided in Tenner et al. (2015).

Among the chondrules investigated, those that formed under the most reducing conditions are older than those produced at more oxidizing conditions (Fig. 11a). All chondrules with excess $^{26}$Mg (Q7, Q16, Q38, M6, and M23; Table 2; Fig. 4). formed 3.4 to 3.6 log units below IW, according to their Mg#'s (99.0 to 99.2; Eqn. 2). The remaining seven chondrules with no resolvable excess $^{26}$Mg formed 2.3 to 3.3 log units below IW, according to their Mg#'s (94.2 to 98.7; Eqn. 2). If one considers the role of early Solar System $H_2O$ ice as an oxidizing agent (e.g. Fedkin and Grossman, 2006; 2016; Connolly and Huss, 2010), these results suggest either (1) ice abundances within the CR chondrite chondrule-forming environment varied on temporal scales; or (2) that separate regions of the CR chondrite chondrule-forming environment coexisted with different $H_2O$ ice abundances, and produced chondrules over different time intervals. Either way, the oldest chondrules are predicted to have formed in a relatively anhydrous environment, while younger chondrules formed in a more ice-enhanced region.

In contrast to our findings, Schrader et al. (2017) report no relationship between redox conditions and Al-Mg isotope systematics among CR chondrite chondrules; they also include data from Nagashima et al. (2014) in their evaluation. However, these datasets have relatively few Al-Mg isotope data from Mg# ≥ 99 chondrules, which, according to our results, are systematically older. In addition, Schrader et al. (2017) calculate chondrule Fe#'s (= 100 − chondrule Mg#) in a manner that slightly differs from our definition described above. Specifically, (1) they use the averaged Fe# of chondrule olivine and the 2SD uncertainty as the equivalent for chondrule Fe#, even if a chondrule has accompanying low-Ca pyroxene EPMA data; and (2) they report the averaged Fe# of low-Ca pyroxene and the 2SD uncertainty as the equivalent for chondrule Fe#, when chondrules have EPMA measurements of only low-Ca pyroxene.

To provide consistency among datasets, we recalculated chondrule Mg#'s from Nagashima et al. (2014) and Schrader et al. (2017) in the same manner as our data. EPMA data related to Nagashima et al. (2014) were kindly provided to us by Kazuhide Nagashima (Appendix EA7). Regarding Mg# > 90 chondrules, all but two of the recalculated chondrule Mg#'s are within 0.4 units of those shown in Fig. 9 from Schrader et al. (2017). However, two chondrules, ED1-MK-#1 and NWA721-#7 from Nagashima et al. (2014) show larger differences. For chondrule ED1-MK-#1, only low-Ca pyroxene EPMA data were collected. Figure 9 from Schrader et al. (2017) shows ED1-MK-#1 has a chondrule Mg# (= 100 − Fe#) of 97.4 with a 2SD of 2.3, while we calculate a higher Mg# of 99.0 $+0.3/-0.2$ (Appendix EA7). This difference occurs because we excluded two EPMA point data with low cation totals of 3.95 and 3.96 formula units (assuming 6 oxygens), and with lower Mg#'s of 96.9 and 98.3, respectively. Regarding chondrule NWA721-#7, there are EPMA data from olivine, with an average Mg# of 99.2, and from low-Ca pyroxene, with an average Mg# of 98.0. Schrader et al. (2017) use only olivine data when reporting the chondrule Mg# (i.e. 99.2 ± 0.3; 2SD), while we calculate a slightly lower chondrule Mg# of 98.6 ± 0.7 when using the olivine and low-Ca pyroxene data (Appendix EA7). For type II chondrules (Mg# < 90), recalculated chondrule Mg#'s differ by 0 to 2.8 units relative to those shown by Schrader et al. (2017). These differences are minor within the context of $fO_2$ variability, as Mg# differences among type II chondrules are relatively insensitive in terms of their corresponding redox conditions (e.g. Eqn. 2; top axis of Fig. 11a).

Recalculated chondrule Mg#'s, and the $(^{26}Al/^{27}Al)_0$ data from Nagashima et al. (2014) and Schrader et al. (2017) are shown in Fig. 11a. We note one Al-rich chondrule from Schrader et al. (2017), PCA 91082,15 Ch14, is interpreted by the authors to have relict plagioclase, based on heterogeneous O-isotope ratios. This could suggest at least some portion of PCA 91082,15 Ch14 plagioclase did not crystallize from the final chondrule melt, meaning the inferred $(^{26}Al/^{27}Al)_0$ of PCA91082,15 Ch14 may not be related to its chondrule Mg#. Therefore, we omit PCA 91082,15 Ch14 data in Fig. 12, but note it has a chondrule Mg# of 99.1 $+0.3/-0.7$, a $(^{26}Al/^{27}Al)_0$ of $(-0.3 \pm 3.4) \times 10^{-6}$, and a $\Delta^{17}O$ of −5.6 ± 1.0‰.

If combining all data shown in Figure 11a, 7 of 8 chondrules with Mg#'s ≥ 99 have resolvable excess $^{26}Mg$, only 2 of 14 chondrules with Mg#'s between 98 and 99 have resolvable excess $^{26}Mg$, and no chondrules (0 of 7) with Mg#'s between 94 and 98 have resolvable excess $^{26}Mg$. As such, chondrules with Mg#'s > 99 appear to more consistently have excess $^{26}Mg$, while Mg# 94–99 chondrules do not. We note porphyritic and Al-rich chondrules are not distinguishable with respect to this relationship.

Three type II chondrule data from Nagashima et al. (2014) and Schrader et al. (2017) have Mg#'s ranging from 49.7 to 75.7 (Fig. 11a). Of these, two have resolvable excess $^{26}Mg$ and one does not. The small sample set and the large internal Mg# variabilities among these chondrules make it difficult to discern if a $(^{26}Al/^{27}Al)_0$ versus Mg# correlation exists among type II CR chondrite chondrules.

#### 4.3.2. Mg# and oxygen isotope relationships: quantifying the role of $^{16}O$-poor $H_2O$ ice—

In addition to the Mg# versus $(^{26}Al/^{27}Al)_0$ correlation shown in Figure 11a, FeO-poor CR chondrite chondrules produce a related trend in which decreasing chondrule Mg#'s correspond to increased $\Delta^{17}O$. This is illustrated in Fig. 11b, where chondrules with known O-isotope ratios and Al-Mg isotope systematics are highlighted (large solid symbols; from this study and from Schrader et al., 2017), along with additional data from Tenner et al. (2015) which were not studied for Al-Mg isotope systematics (small x symbols).

As mentioned earlier, it is hypothesized that increased proportions of $^{16}$O-poor $H_2O$ ice in CR chondrite chondrule precursors made the environment more oxidizing, forming lower Mg# chondrules with higher $\Delta^{17}O$. This seems plausible, as 1 atm. experiments show $H_2O$ vapor readily exchanges its O-isotopes with those from chondrule-like melts (e.g. Yu et al. 1995; Di Rocco and Pack 2015). Dust-to-gas ratios also likely controlled redox conditions of the chondrule-forming environment, according to equilibrium thermodynamic models (e.g. Ebel and Grossman, 2000; Grossman et al., 2008). Tenner et al. (2015) modeled the influence of $H_2O$ ice addition to chondrule precursors in a dust-enriched system by mass balance (Fig. 11b). The model splits chondrule precursors into four components: (1) Solar gas; (2) the silicate portion of dust; (3) $H_2O$ ice in dust; and (4) organic matter in dust. Compositions of each component are based on atomic abundances from Anders and Grevesse (1989) and Allende Prieto et al. (2001; 2002) (see Table 3 from Tenner et al., 2015). Oxygen fractions of each component are constrained at a given dust-to-gas ratio and ice enhancement factor, and $H_2O$ ice proportions are calculated relative to that within CI dust (~18 wt.% $H_2O$; Anders and Grevesse, 1989). Components are assigned the following $\Delta^{17}O$ values: (1) Solar gas: −28.4‰, from Solar wind measurements (McKeegan et al., 2011); (2) silicate in dust: −5.9‰, which comes from the lowest $\Delta^{17}O$ chondrule measured by Tenner et al. (2015); (3) $H_2O$ ice in dust: +5.1‰, which satisfies $\Delta^{17}O$ values of the lowest Mg# chondrules studied by Tenner et al. (2015) (~+0.5‰) when employing a mass balance consisting of CI dust; and (4) organic matter in dust: +11.3‰, which is the average value measured in CR chondrites (Hashizume et al., 2011). Chondrule Mg#'s are simultaneously parameterized by metal-silicate phase equilibria (e.g. eqn. 2), as the imposed oxygen fugacity is directly related to the atomic proportions of H, O, and C in the precursor assemblage (e.g. Eqn. 24 from Grossman et al., 2008; Eqn. 3 from Tenner et al., 2015).

Within these constraints, the model predicts most CR chondrite chondrules formed at dust-to-gas ratios between 100× and 200×. The trend of increasing chondrule $\Delta^{17}O$, from ~–6‰ to ~–1‰, as chondrule Mg#'s decrease from ~99 to ~94, is caused by an increasing proportion of $^{16}$O-poor $H_2O$ ice within the dust, from essentially anhydrous to ~0.8 times the abundance in CI dust (Fig. 12b). Type II chondrules formed in a different environment with higher dust-to-gas ratios (~1000× to ~2500×), and a greater proportion of $H_2O$ ice, corresponding to lower chondrule Mg#'s and higher $\Delta^{17}O$ (Fig. 11b).

**4.3.3. Temporal and spatial relationships of chondrule precursors—**The links between Al-Mg isotope systematics, Mg#'s, and oxygen isotope ratios of chondrules (Fig. 11) allow for interpreting the temporal and spatial relationships of dust, gas, and $H_2O$ ice within the CR chondrite accretion region. This is shown as a simple cartoon in Fig. 12, which considers ice migration into the CR chondrite accretion region as the protoplanetary disk cooled (e.g. Ciesla and Cuzzi, 2006).

For chondrules with excess $^{26}$Mg, Mg#'s ≥ 99, and with $\Delta^{17}O$ values near −5‰ (Fig. 12a), the mass balance model from Fig. 11b predicts formation in an environment depleted in $H_2O$

ice, with a dust to gas ratio of ~100×. Based on Al-Mg isotope systematics from this study (Table 2; Fig. 11a), these chondrules formed 2.2 (−0.5/+1.1) to 2.8 (−0.3/+0.5) Myr after CAIs.

After formation of the chondrules depicted in Fig. 12a, it is possible that upon cooling of the protoplanetary disk, the CR chondrite accretion region received an influx of $^{16}$O-poor $H_2O$ ice ($\Delta^{17}$O: ~+5‰; Fig. 12b). This would have increased the oxidation state and the bulk $\Delta^{17}$O of chondrule precursors. In addition, the mass balance model in Fig. 11b predicts the range of dust to gas ratios expanded, from 100× to 300×, also contributing to more oxidizing conditions. Flash heating events in this environment would have produced Mg# ~94 to ~99 chondrules with $\Delta^{17}$O values of ~−1‰ to ~−5‰, respectively (e.g. Fig. 11b). Such chondrules formed >2.9 to >3.7 Myr after CAIs, based on our inferred $(^{26}\text{Al}/^{27}\text{Al})_0$ upper limits.

CR chondrite chondrules are predominantly FeO-poor (constituting ~96% of the population; Schrader et al., 2011; 2015), meaning the scenario depicted in Figure 12 accounts for nearly all of the accretion region. Based on limited Al-Mg isotope systematics from Nagashima et al. (2014) and Schrader et al. (2017), the more minor, type II chondrule-forming environment (~4% of the chondrule population) appears to have produced chondrules over a broadly similar timeframe as Mg# < 99 FeO-poor chondrules (Fig. 11a).

### 4.4. Comparisons to other carbonaceous chondrites and from Wild 2 comet particles.

When comparing Al-Mg isotope systematics, Mg#'s, and $\Delta^{17}$O to other chondrite chondrules and cometary materials, chondrules from CR chondrites exhibit similarities in some cases, but in other instances there are differences. Comparisons are available for LL3 (Kita et al., 2000; 2010), Acfer 094 (Ushikubo et al., 2012; 2013), and CO3 chondrite chondrules (Kurahashi et al., 2008a; Tenner et al., 2013), as well for Stardust comet particles Iris (Ogliore et al., 2012) and Pyxie (Nakashima et al., 2012; 2015).

LL3, Acfer 094, and CO3 chondrite chondrules have distinct $\Delta^{17}$O and Mg# groups, even though they have similar ranges of $(^{26}\text{Al}/^{27}\text{Al})_0$ (Fig. 13a). LL3 chondrite chondrules have uniform $\Delta^{17}$O (~0–1‰) over a wide chondrule Mg# interval (75–96.3), indicating constant precursor O-isotope ratios, even though redox conditions varied (e.g. Eqn. 2). Acfer 094 and CO3 chondrite chondrules mainly cluster into two groups: those with Mg#'s ≥ 97 largely have $\Delta^{17}$O values of ~−5‰, while those with Mg#'s < 97 have $\Delta^{17}$O values near −2.5‰ (Fig. 13a). Like CR chondrites, the link between decreasing chondrule Mg# and increasing $\Delta^{17}$O among CO and Acfer 094 chondrites is attributed to increased $^{16}$O-poor $H_2O$ ice in chondrule precursors, and elevated dust-to-gas ratios (Ushikubo et al., 2012; Tenner et al., 2013). As chondrules from LL3, CO3, and Acfer 094 chondrites have similar $^{26}$Al age ranges, their distinct oxygen isotope signatures ($\Delta^{17}$O: ~0–1‰ for LL3; $\Delta^{17}$O: ~−2.5‰ and ~−5‰ for CO3 and Acfer 094) suggest the parent bodies were spatially separated. If true, this would support a hypothesis for physically separated ordinary and carbonaceous chondrite accretion regions, which is based on their distinct Cr, Ti, Mg and O-isotope relationships (Warren, 2011; Van Kooten et al., 2016; Gerber et al., 2017). This division is interpreted to have been caused by Jupiter's formation and its influence on dynamic properties of the protoplanetary disk, including pressure regimes, aerodynamic drag, and turbulence (Walsh et al., 2011; 2012; Desch et al., 2018).

CR chondrite chondrules with Mg#'s ≥ 99 and with $\Delta^{17}O$ values of ~−5‰ have similar $(^{26}Al/^{27}Al)_0$ as those from Mg# ≥ 97, $\Delta^{17}O$ ~−5‰ CO3 and Acfer 094 chondrite chondrules (e.g. Fig. 13b). This suggests an anhydrous and low dust density chondrule-forming environment that was common to multiple carbonaceous chondrites over a similar timeframe. In contrast, the lack of resolvable excess $^{26}Mg$ in most Mg# < 99 CR chondrite chondrules with $\Delta^{17}O$ higher than −5‰ (Fig. 14a) differs from lower Mg# CO and Acfer 094 chondrite chondrules, which also have higher $\Delta^{17}O$ (predominantly near −2.5‰), but have excess $^{26}Mg$ (Fig. 13a). Thus, while $H_2O$ ice abundances and dust to-gas ratios in the CO and Acfer 094 chondrule-forming environments varied spatially, these characteristics of the CR chondrite chondrule-forming environment likely varied temporally.

Mafic minerals from comet Wild 2 have Mg#-$\Delta^{17}O$ characteristics similar to those of CR chondrite chondrules (Nakashima et al., 2012; Defouilloy et al., 2017 and included references). Two comet particles, Iris (Ogliore et al., 2012) and Pyxie (Nakashima et al., 2012; 2015), have Mg#'s of 64 and 95, respectively, $\Delta^{17}O$ values of −0.3‰ and −1.1‰, respectively, and neither have resolvable excess $^{26}Mg$ (Fig. 13b). These features are similar to Mg# < 99 CR chondrite chondrules that are relatively $^{16}O$-poor and lack resolvable excess $^{26}Mg$ (Fig. 13b). One possibility for these similarities is that at least some CR chondrite-associated materials were transported to comet-forming regions, possibly involving disk wind (Cuzzi and Hogan, 2003). Evidence for such long-distance transport comes from the presence of CAI-like materials within Stardust particles (Brownlee et al., 2006; McKeegan et al., 2006; Zolensky et al., 2006, Ishii et al., 2010). Ciesla (2007a; 2007b) also show models of a viscously evolving protoplanetary disk induce large-scale outward flows about the midplane, with the ability to carry chondrule and CAI-sized materials to 10 AU.

### 4.5. Comparisons to other isotope systematics of CR chondrite chondrules

Budde et al. (2018) report a concordant mean age of CR chondrite chondrule formation when comparing Pb-Pb (3.66 ± 0.63 Myr after CAIs; Amelin et al., 2002), Al-Mg (3.7 +0.3/–0.2 Myr after CAIs; Nagashima et al., 2014; Schrader et al., 2017), and Hf-W isotope systematics (3.63 ± 0.62 Myr after CAIs; Budde et al., 2018). Although these isotope systems are concordant, the relationship between the mean age of CR chondrite chondrule formation and the true time interval over which chondrules formed requires further attention. For example, the Hf-W data from Budde et al. (2018) and the Pb-Pb data from Amelin et al. (2002) rely on chondrule aggregates/sets, meaning a bulk chondrule formation age is established, but the actual range of chondrule formation is not constrained. Regarding Al-Mg isotope systematics, although individual chondrule ages are routinely generated, many CR chondrite chondrules have unresolvable excess $^{26}Mg$, meaning only upper age limits are determined. Thus, although Al-Mg isotope systematics from this study indicate CR chondrite chondrules formed over a duration of at least 1.2 million years, the true interval is not fully constrained. Considering these limitations, estimates of the CR chondrite parent body accretion age, 3.5 ± 0.5 Myr after CAIs (Sugiura and Fujiya, 2014), as well as the age of CR chondrite parent body alteration, 4–5 Myr after CAIs (Jilly-Rehak et al., 2017), are useful, because they anchor the latest point CR chondrite chondrules could have formed. Nearly half of the chondrules studied here (5 of 12) have inferred ages of >3.6 Myr after CAIs, indicating a significant proportion formed immediately prior to parent body accretion. If there is a contingent of relatively old chondrules, as suggested by Al-Mg isotope systematics (this study, Nagashima et al., 2014; Schrader et al., 2017), and as suggested by Pb-Pb ages of some individual chondrules (Bollard et al., 2017), they likely represent a minor population, as hypothesized by Schrader et al. (2017).

With this in mind the mean CR chondrite chondrule formation age by Al-Mg isotope systematics can be refined, so that it reflects the proportions of chondrules with and without resolvable excess $^{26}$Mg. To do so, we use the relationship where Mg# ≥ 99 chondrules predominantly have resolvable, positive $(^{26}\mathrm{Al}/^{27}\mathrm{Al})_0$ (e.g. 7 of 8; Fig. 11a), and where most Mg# < 99 chondrules do not (e.g. 4 of 24; Fig. 11a). Next, we estimate the modes of Mg# > 99 and Mg# ≤ 99 chondrules using data from Tenner et al. (2015), who determined Mg#'s of every chondrule in the MET 00426,46 thin section, constituting 29 chondrules/chondrule fragments. Of these, five have Mg#'s ≥ 99 (17.2%), and 24 have Mg#'s below 99 (82.8%). We then refine the mean chondrule formation age by mass balance, using (1) the respective weighted mean Al-Mg isotope systematics of Mg# ≥ 99 and Mg# < 99 CR chondrite chondrules; and (2) the corresponding chondrule Mg# modes (Appendix EA8). In the following, we provide calculations using (1) only data from this study, and (2) the combined data shown in Fig. 11a, from this study, Nagashima et al. (2014) and Schrader et al. (2017).

In terms of $(^{26}\mathrm{Al}/^{27}\mathrm{Al})_0$, the mass balance generates a value of $(0.9 \pm 0.6) \times 10^{-6}$, using only data from this work, and a value of $(1.6 \pm 0.3) \times 10^{-6}$, using the combined data shown in Fig. 11a (Appendix EA8). Uncertainties are propagated errors coming from the weighted mean $(^{26}\mathrm{Al}/^{27}\mathrm{Al})_0$ of each Mg# mode. These $(^{26}\mathrm{Al}/^{27}\mathrm{Al})_0$ values correspond to refined mean chondrule formation ages of 4.2 (+1.2/−0.6) Myr, if using only data from this work, and 3.5 (+0.2/–0.1) Myr, if using the combined dataset shown in Fig. 11a. However, we stress that $(^{26}\mathrm{Al}/^{27}\mathrm{Al})_0$ values change exponentially with relative $^{26}$Al ages, meaning that an age calculated from a mean $(^{26}\mathrm{Al}/^{27}\mathrm{Al})_0$ is biased toward an older value when the collective duration of chondrule formation is longer than the $^{26}$Al half-life, which is the case for CR chondrite chondrules. Therefore, we refine the mass balance even further, by employing the mean relative ages of each chondrule Mg# mode, rather than their mean $(^{26}\mathrm{Al}/^{27}\mathrm{Al})_0$ values (Appendix EA8). By doing do, the mass balance generates a refined mean age of 3.8 ± 0.3 Myr after CAIs, if using the combined data shown in Fig. 11a. Here, the uncertainty is the propagated error coming from the mean ages of each Mg# mode. If considering only the data from this work, the mass balance cannot produce a fully constrained age in this manner, because the mean relative age of Mg# < 99 chondrules is only an upper limit. Thus, our preferred mean chondrule formation age for all CR chondrite chondrules is 3.8 ± 0.3 Myr after CAIs (if only considering Mg# ≥ 99 chondrules their mean formation age is 2.4 ± 0.1 Myr after CAIs, and for Mg# < 99 chondrules their mean age is 4.1 ± 0.3 Myr after CAIs) (Appendix EA8). This value is similar to the estimate from Schrader et al. (2017), but benefits from the added clarity of the chondrule Mg# mode/chondrule age relationship (e.g. Fig. 11a), and also accounts for the non-linearity between chondrule $(^{26}\mathrm{Al}/^{27}\mathrm{Al})_0$ and the corresponding relative age. As such, the mean Al-Mg age of CR chondrite chondrules is consistent with Pb-Pb and Hf-W isotope systematics of chondrule aggregates/sets (e.g.

Amelin et al., 2002; Budde et al., 2018). Finally, the relationship between chondrule ages, Mg#'s, and oxygen isotopes offers a pathway to improve the significance of Hf-W and Pb-Pb isotope systematics of CR chondrite chondrule aggregates, particularly if Mg# > 99 and Mg# ≤ 99 are measured separately. The latter would better constrain the mean age for CR chondrite chondrules that are too young to resolve by Al-Mg isotope systematics. However, care must be taken to identify samples that avoided disturbances related to the isotope system of interest.

## CONCLUSIONS

We investigated Al-Mg isotope systematics of twelve FeO-poor CR chondrite chondrules by SIMS, and assessed the quality of plagioclase that control slopes of mineral isochrons. We found that:

1. Five chondrules have resolvable excess $^{26}$Mg, with $(^{26}Al/^{27}Al)_0$ values of $(3.5 \pm 1.3) \times 10^{-6}$ to $(6.0 \pm 3.9) \times 10^{-6}$. Including isochron uncertainties, and using a canonical $(^{26}Al/^{27}Al)_0$ value of $5.23 \times 10^{-5}$, this corresponds to their formation 1.7 to 3.3 Myr after CAIs. These chondrules have high Mg#'s (99.0 to 99.2), and a narrow $\Delta^{17}O$ range (–4.2‰ to –5.3‰).
2. Seven chondrules lack resolvable excess $^{26}$Mg. Their $(^{26}Al/^{27}Al)_0$ upper limits range from $1.3 \times 10^{-6}$ to $3.2 \times 10^{-6}$, corresponding to formation >2.9 to >3.7 Myr after CAIs. They have lower Mg#'s (94.2 to 98.7) and generally higher $\Delta^{17}O$ (–0.9 to –4.9‰), relative to the five chondrules with excess $^{26}$Mg.
3. When comparing chondrules with and without excess $^{26}$Mg, the estimated chondrule formation duration was at least 1.1 Myr, and if considering uncertainties, may have extended beyond 2 Myr.
4. Several characteristics indicate the plagioclase used to establish chondrule isochrons have an undisturbed Al-Mg isotope system. First, SIMS depth profile patterns of $^{27}Al/^{24}Mg$ match those collected from anorthite glass standards. Second, TEM analysis shows little-to-no inclusions, and no replacement by other mineral phases during thermal metamorphism, even at the nanometer scale. Third, when comparisons are available, oxygen isotope ratios of chondrule plagioclase match those from coexisting olivine and pyroxene, indicating a low extent of thermal metamorphism (< 150°C in a wet system). Fourth, nearly all chondrule plagioclase studied has a resolvable "excess silica", $[\ ]Si_4O_8$ component, which is an anhydrous high-temperature primary crystallization feature. In addition, the chondrule plagioclase studied have high anorthite contents (0.793 to 0.999, when normalized to anorthite, albite, and K-feldspar components), and have relatively high concentrations of MgO (0.6 to 1.2 wt.%). These features are consistent with chondrule plagioclase from the least thermally altered 3.00 to 3.05 petrologic type chondrites.
5. Using relationships between chondrule $(^{26}Al/^{27}Al)_0$, Mg#, and $\Delta^{17}O$, we interpret spatial and temporal features related to dust, gas, and $H_2O$ ice abundances within the FeO-poor CR chondrite chondrule-forming environment.

We estimate that from 2.2 (−0.5/+1.1) to 2.8 (−0.3/+0.5) Myr after CAIs the environment was relatively anhydrous, with a dust-to-gas ratio of ~100× that produced Mg# ≥ 99, $\Delta^{17}$O ~−5‰ chondrules with resolvable excess $^{26}$Mg. After formation of these chondrules, we interpret that $^{16}$O-poor $H_2O$ ice migrated into this chondrule-forming region, and that the dust-to-gas ratio increased (100× to 300×), leading to the production of more oxidized Mg# 94–99 chondrules with higher $\Delta^{17}$O (−5‰ to –1‰), and with no resolvable excess $^{26}$Mg.

**6.** Using data from this study and from previous work (Nagashima et al., 2014; Schrader et al., 2017), we establish a refined mean CR chondrite chondrule formation age of 3.8 ± 0.3 Myr after CAIs. This is accomplished via mass balance, employing (1) modal proportions of Mg# ≥ 99 and Mg# < 99 chondrules in CR chondrites; and (2) mean relative ages from each Mg# mode. This age is consistent with those from Pb-Pb and Hf-W isotope systematics of CR chondrite chondrule aggregates (3.66 ± 0.63 Myr after CAIs and 3.63 ± 0.62 Myr after CAIs, respectively; Amelin et al., 2002 and Budde et al., 2018, respectively).

## Supplementary Material

Refer to Web version on PubMed Central for supplementary material.

## ACKNOWLEDGEMENTS

We thank the ANSMET Program and Meteorite Working Group for providing the meteorite thin sections for this study. We thank John Fournelle for assistance with EPMA measurements, and Jim Kern for technical assistance during SIMS operations. Dr. Akira Yamaguchi helped to analyze phases by Raman spectroscopy at NIPR. We thank Kazuhide Nagashima and two anonymous reviewers, as well as associate editor Dimitri Papanastassiou, for constructive comments that improved the quality of this submission. This work is supported by NASA (NNX11AG62G, NNX14AG29G, NK; 80NSSC18K0589, MKW) and a Grant-in-aids of Monkashou, Japan (No. 26400510 to MK). WiscSIMS is partly supported by NSF (EAR03-19230, EAR10-53466, EAR13-55590). Through Los Alamos National Laboratory, this document is approved for unlimited release under LA-UR-18-30036.

## REFERENCES

Abreu NM and Brearley AJ (2010) Early solar system processes recorded in the matrices of two highly pristine CR3 carbonaceous chondrites, MET 00426 and QUE 99177. Geochim. Cosmochim. Acta 74, 1146–1171.

Alexander CMO'D and Ebel DS (2012) Questions, questions: Can the contradictions between the petrologic, isotopic, thermodynamic, and astrophysical constraints on chondrule formation be resolved? Meteorit. Planet. Sci 47, 1157–1175. Geochim. Cosmochim. Acta 123, 244–260.

Alexander CMO'D, Howard KT, Bowden R, Fogel ML (2013) The classification of CM and CR chondrites using bulk H, C, and N abundances and isotopic compositions. Geochim. Cosmochim. Acta 123, 244–260.

Allende Prieto C and Lambert DL (2001) The forbidden abundance of oxygen in the Sun. Astrophys. J 556, L63–L66.

Allende Prieto C and Lambert DL (2002) A reappraisal of the solar photospheric C/O ratio. Astrophys. J 573, L137–L140.

Amelin Y, Krot AN, Hutcheon ID and Ulyanov (2002) Lead isotopic ages of chondrules can calcium-aluminum-rich inclusions. Science 297, 1678–1683. [PubMed: 12215641]

Amelin Y, Kaltenbach A, Iizuka T, Stirling CH, Ireland TR, Petaev M, and Jacobsen SB (2010) U-Pb chronology of the Solar System's oldest solids with variable $^{238}$U/$^{235}$U. Earth Planet. Sci. Lett 300, 343–350.

Anders E and Grevesse N (1989) Abundances of the elements: meteoritic and solar. Geochim. Cosmochim. Acta 53, 197–214.

Baldridge WS, Beaty DW, Hill SMR, and Albee AL (1979) The petrology of the Apollo 12 pigeonite basalt suite. Proc. Lunar Planet. Sci. Conf. 10th, 141–179.

Baertschi P (1976) Absolute $^{18}$O content of standard mean ocean water. Earth Planet. Sci. Lett 31, 341–344.

Beaty DW and Albee AL (1980) Silica solid solution and zoning in natural plagioclase. Am. Miner 65, 63–74.

Beaty DW, Hill SMR, Albee AL, and Baldridge WS (1979) Apollo 12 feldspathic basalts 12031, 12038, and 12072: petrology, comparison and interpretations. Proc. Lunar Planet. Sci. Conf. 10th, 115–139.

Bogdanovski O, Papanastassiou DA and Wasserburg GJ (2002) Cr isotopes in Allende Ca-Al-rich inclusions. 33rd Lunar and Planet. Sci. Conf. CD-ROM. #1802.

Bollard J, Kawasaki N, Sakamoto N, Larsen K, Wielandt D, Schiller M, Connelly J, Yurimoto H and Bizzarro M (2015) Early disk dynamics inferred from isotope systematics of individual chondrules. Meteorit. Planet. Sci 50 (Suppl.), #5211 (abstr.).

Bollard J, Connelly JN, Whitehouse MJ, Pringle EA, Bonal L, Jørgensen JK, Nordlund Å, Moynier F and Bizzarro M (2017) Early formation of planetary building blocks inferred from Pb isotopic ages of chondrules. Sci. Adv 3, e1700407. doi:10.1126/sciadv.1700407 [PubMed: 28808680]

Bouvier A, Spivak-Birndorf LJ, Brennecka GA, and Wadhwa M (2011a) New constraints on early solar system chronology from Al-Mg and U-Pb isotope systematics in the unique basaltic achondrite Northwest Africa 2976. Geochim. Cosmochim. Acta 75, 5310–5323.

Bouvier A, Brennecka GA, and Wadhwa M (2011b) Absolute chronology of the first solids in the solar system Workshop on the formation of the first solids in the solar system. 11 7–9, 2011, Kaui, Hawai'i LPI Contribution No. 1639 (abstract #9054).

Bouvier A and Wadhwa M (2010) The age of the Solar System redefined by the oldest Pb-Pb age of a meteoritic inclusion. Nature Geosci. 3, 637–641.

Brearley AJ (1997) Disordered bipyriboles, amphibole, and talc in the Allende meteorite: Products of nebular or parent body alteration? Science 276, 1103–1105. [PubMed: 9148802]

Brooks C, Hart SR, and Wendt I (1972) Realistic use of two-error regression treatments as applied to rubidium-strontium data. Rev. Geophys. Space Phys 10, 551–577.

Brownlee D, Tsou P, Aléon J, Alexander CMO'D, Araki T, Bajt S, Baratta GA, Bastien R, Bland P, Bleuet P, Borg J, Bradley JP, Brearley A, Brenker F, Brennan S, Bridges JC, Browning ND, Brucato JR, Bullock E, Burchell MJ, Busemann H, Butterworth A, Chaussidon M, Chauvront A, Chi M, Cintala MJ, Clark BC, Clemett SJ, Cody G, Colangeli L, Cooper G, Cordier P, Daghlian C, Dai Z, D'Hendecourt L, Djouadi Z, Dominguez G, Duxbury T, Dworkin JP, Ebel DS, Economou TE, Fakra S, Fairey SAJ, Fallon S, Fermini G, Ferroir T, Fleckenstein H, Floss C, Flynn G, Franchi IA, Fries M, Gainsforth Z, Gallien J-P, Genge M, Gilles MK, Gillet P, Gilmour J, Glavin DP, Gounelle M, Grady MM, Graham GA, Grant PG, Green SF, Grossemy F, Grossman L, Grossman JN, Guan Y, Hagiya K, Harvey R, Heck P, Herzog GF, Hoppe P, Hörz F, Huth J, Hutcheon ID, Ignatyev K, Ishii H, Ito M, Jacob D, Jacobsen C, Jacobsen S, Jones S, Joswiak D, Jurewicz A, Kearsley AT, Keller LP, Khodja H, Kilcoyne ALD, Kissel J, Krot A, Langenhorst F, Lanzirotti A, Le L, Leshin LA, Leitner J, Lemelle L, Leroux H, Liu M-C, Luening K, Lyon I, MacPherson G, Marcus MA, Marhas K, Marty B, Matrajt, McKeegan K, Meibom A, Mennella V, Messenger K, Messenger S, Mikouchi T, Mostefaoui S, Nakamura T, Nakano T, Newville M, Nittler LR, Ohnishi I, Ohsumi K, Okudaira K, Papanastassiou DA, Palma R, Palumbo ME, Pepin RO, Perkins D, Perronnet M, Pianetta P, Rao W, Rietmeijer FJM, Robert F, Rost D, Rotundi A, Ryan R, Sandford SA, Schwandt CS, See TH, Schlutter D, Sheffield-Parker J, Simionovici A, Simon S, Sitnitsky I, Snead CJ, Spencer MK, Stadermann FJ, Steele A, Stephan T, Stroud R, Susini J, Sutton SR, Suzuki Y, Taheri M, Taylor S, Teslich N, Tomeoka K, Tomioka N, Toppani A, Trigo-Rodríguez JM, Troadec D, Tsuchiyama A, Tuzzolino AJ, Tyliszczak T, Uesugi K, Velbel M, Vellenga J, Vicenzi E, Vincze L, Warren J, Weber I, Weisberg M, Westphal AJ, Wirick S, Wooden D, Wopenka B, Wozniakiewicz P, Wright I, Yabuta H, Yano H, Young ED, Zare RN, Zega T, Ziegler K, Zimmerman L, Zinner E and Zolensky M (2006) Comet 81P/Wild 2 under a microscope. Science 314, 1711–1716. [PubMed: 17170289]

Budde G, Kleine T, Kruijer TS, Burkhardt C, and Metzler K (2016) Tungsten isotopic constraints on the age and origin of chondrules. Proc. Natl. Acad. Sci. U.S.A 113, 2886–2891. [PubMed: 26929340]

Budde G, Kruijer TS and Kleine T (2018) Hf-W chronology of CR chondrites: implications for the timescales of chondrule formation and the distribution of $^{26}$Al in the solar nebula. Geochim. Cosmochim. Acta 222, 284–304.

Catanzaro EJ, Murphy TJ, Garner EL, and Shields WR (1966) Absolute isotopic abundance ratios and atomic weights of magnesium. J. Res Natl. Bur. Stand 70a, 453–458.

Chaumard N, Defouilloy C and Kita NT (2018) Oxygen isotope systematics of chondrules in the Murchison CM2 chondrite and implications for the CO-CM relationship. Geochim. Cosmochim. Acta 228, 220–242. [PubMed: 30713349]

Ciesla FJ (2007a) Outward transport of high-temperature materials around the midplane of the Solar Nebula. Science 318, 613–615. [PubMed: 17962555]

Ciesla FJ (2007b) Two-dimensional transport of solids in viscous protoplanetary disks. Icarus 200, 665–671.

Ciesla FJ and Cuzzi JN (2006) The evolution of the water distribution in a viscous protoplanetary disk. Icarus 181, 178–204.

Clayton RN, Onuma N, Grossman L and Mayeda TK (1977) Distribution of the pre-solar component in Allende and other carbonaceous chondrites. Earth Planet. Sci. Lett 34, 209–224.

Connelly JN, Bizzarro M, Krot AN, Nordlund Å, Wielandt D, and Ivanova MA (2012) The absolute chronology and thermal processing of solids in the solar protoplanetary disk. Science 338, 651–655. [PubMed: 23118187]

Connolly HC Jr. and Huss GR (2010) Compositional evolution of the protoplanetary disk: oxygen isotopes of type-II chondrules from CR2 chondrites. Geochim. Cosmochim. Acta 74, 2473–2483.

Cuzzi JN and Hogan RC (2003) Blowing in the wind: I. Velocities of chondrule-sized particles in a turbulent protoplanetary nebula. Icarus 164, 127–138.

Cuzzi JN, Hogan RC and Bottke WF (2010) Towards initial mass functions for asteroids and Kuiper Belt Objects. Icarus 208, 518–538.

Davis AM, Richter FM, Mendybaev RA, Janney PE, Wadhwa M and McKeegan KD (2015) Isotopic mass fractionation laws for magnesium and their effects on $^{26}$Al-$^{26}$Mg systematics in solar system materials. Geochim. Cosmochim. Acta 158, 245–261.

Defouilloy C, Nakashima D, Joswiak DJ, Brownlee DE, Tenner TJ, and Kita NT (2016) Origin of crystalline silicates from Comet 81P/Wild 2: combined study on their oxygen isotopes and mineral chemistry. Earth Planet. Sci. Lett 465, 145–154.

Desch SJ, Morris MA, Connolly HC Jr., and Boss AP (2012) The importance of experiments: constraints on chondrule formation models. Meteorit. Planet. Sci 47, 1139–1156.

Desch SJ, Kalyaan A and Alexander CMO'D (2018) The effect of Jupiter's formation on the distribution of refractory elements and inclusions in meteorites. Astrophys J Suppl S, 238, 11 (31pp).

Di Rocco T and Pack A (2015) Triple oxygen isotope exchange between chondrule melt and water vapor: an experimental study. Geochim. Cosmochim. Acta 164, 17–34.

Dymek RF, Albee AL, and Chodos AA (1975) Comparative mineralogy and petrology of Apollo 17 mare basalts: Samples 70215, 71055, 74255, and 75055. Proc. Lunar Sci. Conf. *6th*, 49–77.*th*

Ebel DS and Grossman L (2000) Condensation in dust-enriched systems. Geochim. Cosmochim. Acta 64, 339–366.

Fedkin AV and Grossman L (2006) The fayalite content of chondritic olivine: obstacle to understanding the condensation of rocky material In Meteorites and the Early Solar System II (eds. Lauretta DS and McSween HY). Univ. of Arizona Press, Tucson, pp. 279–294.

Fedkin AV and Grossman L (2016) Effects of dust enrichment on oxygen fugacity of cosmic gases. Meteorit. Planet. Sci 51, 843–850.

Gerber S, Burkhardt C, Budde G, Metzler K and Kleine T (2017) Mixing and transport of dust in the early solar nebula as inferred from titanium isotope variations among chondrules. Astrophys. J. Lett 841, L17 (7 pp).

Gilbert B, Frazer BH, Naab F, Fournelle J, Valley JW and De Stasio G (2003) X-ray absorption spectroscopy of silicates for in situ, sub-micrometer mineral identification. Am. Miner 88, 763–769.

Giletti BJ, Semet MP, and Yund RA (1978) Studies in diffusion−III. Oxygen in feldspars: an ion microprobe determination. Geochim. Cosmochim. Acta 42, 45–57.

Grossman L, Beckett JR, Fedkin AV, Simon SB and Ciesla FJ (2008) Redox conditions in the solar nebula: observational, experimental, and theoretical constraints In Reviews in Mineralogy and Geochemistry, vol. 68 (ed. MacPherson GJ). Mineralogical Society of America, Washington, D.C., pp. 93–140.

Harju ER, Rubin AE, Ahn I, C. B-G, Ziegler K, and Wasson JT (2014) Progressive aqueous alteration of CR carbonaceous chondrites. Geochim. Cosmochim. Acta 139, 267–292.

Hashizume K, Takahata N, Naraoka H and Sano Y (2011) Extreme oxygen isotope anomaly with a solar origin detected in meteoritic organics. Nature Geosci. 4, 165–168.

Hertwig A, Kita NT and Defouilloy C (2018) Formation of chondrules in a moderately high dust enriched disk: evidence from oxygen isotopes of chondrules from the Kaba CV3 chondrite. Geochim. Cosmochim. Acta 224, 116–131. [PubMed: 30713348]

Hewins RH and Radomsky PM (1990) Temperature conditions for chondrule formation. Meteoritics 25, 309–318.

Howard KT, Alexander CMO’D, Schrader DL, and Dyl KA (2015) Classification of hydrous meteorites (CR, CM ad C2 ungrouped) by phyllosilicate fraction: PSD-XRD modal mineralogy and planetesimal environments. Geochim. Cosmochim. Acta 149, 206–222.

Hu Y, Harrington MD, Sun Y, Yang Z, Konter J and Teng F-Z (2016) Magnesium isotopic homogeneity of San Carlos olivine: a potential standard for Mg isotopic analysis by multi-collector inductively coupled plasma mass spectrometry. Rapid Commun. Mass Spectrom 30, 2123–2132. [PubMed: 27477120]

Huss GR and Lewis RS (1994) Noble gases in presolar diamonds II: Component abundances reflect thermal processing. Meteoritics 29, 811–829.

Huss GR, MacPherson GJ, Wasserburg GJ, Russell SS, and Srinivasan G (2001) Aluminum-26 in calcium-aluminum-rich inclusions and chondrules from unequilibrated ordinary chondrites. Meteorit. Planet. Sci 36, 975–997.

Hutcheon ID, Marhas KK, Krot AN, Goswami JN, Jones RH (2009) $^{26}$Al in plagioclase-rich chondrules in carbonaceous chondrites: evidence for an extended duration of chondrule formation. Geochim. Cosmochim. Acta 73, 5080–5099.

Hutcheon ID and Hutchison R (1989) Evidence from the Semarkona ordinary chondrite for $^{26}$Al heating of small planets. Nature 337, 238–241.

Ichimura S, Seto Y and Tomeoka K (2017) Nepheline formation in chondrite parent bodies: Verification through experiments. Geochim. Cosmochim. Acta 210, 114–131.

Ishii HA, Stadermann FJ, Floss C, Joswiak D, Bradley JP, Teslich N, Brownlee DE, Matrajt G, MacPherson G and McKeegan KD (2010) Lack of evidence for in situ decay of aluminum-26 in comet 81P/Wild 2 CAI-like refractory particles ‘Inti’ and ‘Coki’. 41st Lunar and Planet. Sci. Conf. CD-ROM. #2317.

Jacobsen B, Yin Q-Z Moynier F, Amelin Y, Krot AN, Nagashima K, Hutcheon ID, and Palme H (2008) $^{26}$Al/$^{26}$Mg and $^{207}$Pb-$^{206}$Pb systematics of Allende CAIs: Canonical solar initial $^{26}$Al/$^{27}$Al ratio reinstated. Earth Planet. Sci. Lett 272, 353–364.

Jarosewich E, Nelen JA and Norberg JA (1980) Reference samples for electron microprobe analysis. Geostandards Newsletter 4, 43–47.

Jilly-Rehak CE, Huss GR and Nagashima K (2017) $^{53}$Mn-$^{53}$Cr radiometric dating of secondary carbonates in CR chondrites: timescales for parent body aqueous alteration. Geochim. Cosmochim. Acta 201, 224–244.

Jones RH and Schilk AJ (2009) Chemistry, petrology and bulk oxygen isotope compositions of chondrules from the Mokoia CV3 carbonaceous chondrite. Geochim. Cosmochim. Acta 73, 5854–5883.

Kerrick DM, Eminhizer LB and Villaume JF (1970) The role of carbon film thickness in electron microprobe analysis. Am. Miner 58, 920–925

Kimura M and Ikeda Y (1995) Anhydrous alteration of Allende chondrules in the solar nebula II: Alkali-Ca exchange reactions and formation of nepheline, sodalite, and Ca-rich phases in chondrules. Proc. NIPR Symp. Antarct. Meteorites 8, 123–128.

Kimura M and Ikeda Y. (1997) Comparative study of anhydrous alteration of chondrules in reduced and oxidized CV chondrites. Proc. NIPR Symp. Antarct. Meteorites 10, 191–202.

Kimura M and Ikeda Y (1998) Hydrous and anhydrous alteration of chondrules in Kaba and Mokoia CV chondrites. Meteorit. Planet. Sci 33, 1139–1146.

Kimura M, Grossman JN, and Weisberg MK (2008) Fe-Ni metal in primitive chondrites: Indicators of classification and metamorphic conditions for ordinary and CO chondrites. Meteorit. Planet. Sci 43, 1167–1177.

Kita NT and Ushikubo T (2012) Evolution of protoplanetary disk inferred from 26Al chronology of individual chondrules. Meteorit. Planet. Sci 47, 1108–1119.

Kita NT, Nagahara H, Togashi S, and Morishita Y (2000) A short duration of chondrule formation in the solar nebula: Evidence from $^{26}$Al in Semarkona ferromagnesian chondrules. Geochim. Cosmochim. Acta 64, 3913–3922.

Kita NT, Lin Y, Kimura M, and Morishita Y (2004a) The $^{26}$Al-$^{26}$Mg chronology of a type C CAI and POIs in Ningqiang carbonaceous chondrite. 35th Lunar and Planet. Sci. Conf. CD-ROM. #1471.

Kita NT, Kimura M, and Morishita Y (2004b) The Al-Mg system in chondrules from the most primitive H chondrite Y82038. Papers presented to the 28th Symposium on Antarctic Meteorites pp. 33–34. June 1–3, 2004, National Institute of Polar Research, Tokyo.

Kita NT, Nagahara H, Tachibana S, Tomomura S, Spicuzza MJ, Fournelle JH and Valley JW (2010) High precision SIMS oxygen three isotope study of chondrules in LL3 chondrites: role of ambient gas during chondrule formation. Geochim. Cosmochim. Acta 74, 6610–6635.

Kita NT, Ushikubo T, Knight KB, Mendybaev RA, Davis AM, Richter FM, Fournelle JH (2012) Internal $^{26}$Al-$^{26}$Mg isotope systematics of a Type B CAI: Remelting of refractory precursor solids. Geochim. Cosmochim. Acta 86, 37–51.

Kita NT, Yin Q-Z, MacPherson GJ, Ushikubo T, Jacobsen B, Nagashima K, Kurahashi E, Krot AN, and Jacobsen SB (2013) $^{26}$Al-$^{26}$Mg isotope systematics of the first solids in the early solar system. Meteorit. Planet. Sci 48, 1383–1400.

Kita NT, Ushikubo T, Tenner TJ, Romaniello SJ and Wadhwa M (2016) Instrumental biases for SIMS magnesium isotope analyses. Goldschmidt conf #1538 (abstr.).

Kleine T, Hans U, Irving AJ and Bourdon B (2012) Chronology of the angrite parent body and implications for core formation in protoplanets. Geochim. Cosmochim. Acta 84, 186–203.

Kring DA (1988) The petrology of meteoritic chondrules: evidence for fluctuating conditions in the solar nebula. PhD thesis, Harvard Univ.

Krot AN and Keil K (2002) Anorthite-rich chondrules in CR and CH carbonaceous chondrites: Genetic link between calcium-aluminum-rich inclusions and ferromagnesian chondrules. Meteorit. Planet. Sci 37, 91–111.

Krot AN, Hutcheon ID, and Keil K (2002) Plagioclase-rich chondrules in the reduced CV chondrites: evidence for complex formation history and genetic links between calcium-aluminum-rich inclusions and ferromagnesian chondrules. Meteorit. Planet. Sci 37, 155–182.

Krot AN, Libourel G, and Chaussidon M (2006) Oxygen isotope compositions of chondrules in CR chondrites. Geochim. Cosmochim. Acta 70, 767–779.

Krot AN, Nagashima K, Fintor K and Pál-Molnár E (2019) Evidence for oxygen-isotope exchange in refractory inclusions from Kaba (CV3.1) carbonaceous chondrite during fluid-rock interaction on the CV parent asteroid. Geochim. Cosmochim. Acta 246, 419–435.

Kruijer TS, Kleine T, Fischer-Gödde M, Burkhardt C and Wieler R (2014) Nucleosynthetic W isotope anomalies and the Hf-W chronometry of Ca-Al-rich inclusions. Earth Planet. Sci. Lett 403, 317–27.

Kuffmeier M, Mogensen TF, Haugbølle T, Bizzarro M, Nordlund Å (2016) Tracking the distribution of $^{26}$Al and $^{60}$Fe during the early phases of star and disk evolution. Astrophys. J 826, 22 (15pp).

Kunihiro T, Rubin AE, McKeegan KD, and Wasson JT (2004) Initial $^{26}$Al/$^{27}$Al in carbonaceous-chondrite chondrules: too little $^{26}$Al to melt asteroids. Geochim. Cosmochim. Acta 68, 2947–2957.

Kurahashi E, Kita NT, Nagahara H, and Morishita Y (2008a) $^{26}$Al/$^{27}$Al systematics of chondrules in a primitive CO chondrite. Geochim. Cosmochim. Acta 72, 3865–3882.

Kurahashi E, Kita NT, Nagahara H, and Morishita Y (2008b) $^{26}$Al-$^{26}$Mg systematics and petrological study of chondrules in CR chondrites. Geochim. Cosmochim. Acta 72, A504.

Lamb WM and Valley JW (1988) Granulite facies amphibole and biotite equilibria, and calculated peak-metamorphic water activities. Contrib. Mineral. Petrol 100, 349–360.

Larsen KK, Trinquier A, Paton C, Schiller M, Wielandt D, Ivanova MA, Connelly JN, Nordlund Å, Krot AN, and Bizzarro M (2011) Evidence for magnesium isotope heterogeneity in the solar protoplanetary disk. Astrophys. J 735, L37 (7pp).

LaTourrette T and Wasserburg GJ (1998) Mg diffusion in anorthite: implications for the formation of early solar system planetesimals. Earth Planet. Sci. Lett 158, 91–108.

Lee T, Papanastassiou DA, and Wasserburg GJ (1976) Demonstration of $^{26}$Mg excess in Allende and evidence for $^{26}$Al. Geophys. Res. Lett 3, 41–44.

Lofgren GE and Le L (2000) Experimental evidence for a partial melting origin for most porphyritic chondrules. 31st Lunar and Planet. Sci. Conf. CD-ROM. #1809.

Longhi J (1976) Iron, magnesium, and silica in plagioclase. PhD thesis, Harvard Univ.

Longhi J and Hays JF (1979) Phase equilibria and solid solution along the join $CaAl_2Si_2O_8$-$SiO_2$. Am. J. Sci 279, 876–890.

Longhi J, Walker D and Hays JF (1976) Fe and Mg in plagioclase. Proc. Lunar Sci. Conf. 7th, 1281–1300.

Ludwig KR (2003) Isoplot 3.00. A geochronological toolkit for Microsoft excel. Berkeley Geochronology center Special Publication No.4, 1–72.

MacPherson GJ, Bullock ES, Janney PE, Kita NT, Ushikubo T, Davis AM, Wadhwa M, and Krot AN (2010) Early solar system condensates with canonical, not supracanonical, initial $^{26}$Al/$^{27}$Al ratios. Astrophys. J 711, L117–L121.

Makide K, Nagashima K, Krot AN, Huss GR, Hutcheon ID, Hellebrand E, and Petaev M (2013) Heterogeneous distribution of $^{26}$Al at the birth of the solar system: evidence from corundum-bearing refractory inclusions in carbonaceous chondrites. Geochim. Cosmochim. Acta 110, 190–215.

Matson DW, Sharma SK, and Philpotts JA (1986) Raman spectra of some tectosilicates and of glasses along the orthoclase-anorthite and nepheline-anorthite joins. Am. Miner 71, 694–704.

McKeegan KD, Kallio APA, Heber VS, Jarzebinski G, Mao PH, Coath CD, Kunihiro T, Wiens RC, Nordholt JE, Moses RW, Reisenfeld DB, Jurewicz AJG and Burnett DS (2011) The oxygen isotopic composition of the Sun inferred from captured solar wind. Science 332, 1528–1532. [PubMed: 21700868]

Mittlefehldt DW, Le L and Berger EL (2017) Excess silica substitution in plagioclase grain in the Pasamonte eucrite. Meteorit. Planet. Sci 52, S1, A236.

Miyamoto M (1991) Thermal metamorphism of CI and CM carbonaceous chondrites: An internal heating model. Meteoritics 26, 111–115.

Mostefaoui S, Kita NT, Togashi S, Tachibana S, Nagahara H and Morishita Y (2002) The relative formation ages of ferromagnesian chondrules inferred from their initial aluminum-26/aluminum-27 ratios. Meteorit. Planet. Sci 37, 421–438.

Nagashima K, Krot AN, and Huss GR (2014) $^{26}$Al in chondrules from CR2 chondrites. Geochem. J 48, 561–570.

Nagashima K, Krot AN and Komatsu M (2017) $^{26}$Al-$^{26}$Mg systematics in chondrules from Kaba and Yamato 980145 CV3 carbonaceous chondrites. Geochim. Cosmochim. Acta 201, 303–319.

Nagashima K, Kita NT and Luu T-H (2018) $^{26}$Al-$^{26}$Mg systematics of chondrules In Chondrules: Records of Protoplanetary Disk Processes (eds. Russell SS, Connolly H Jr. and Krot AN). Cambridge University Press, Cambridge U.K., pp. 247–275.

Nakashima D, Ushikubo T, Joswiak DJ, Brownlee DE, Matrajt G, Weisberg MK, Zolensky ME, and Kita NT (2012) Oxygen isotopes in crystalline silicates of comet Wild 2: a comparison of oxygen isotope systematics between Wild 2 particles and chondritic materials. Earth Planet Sci. Lett 357-358, 355–365.-

Nakashima D, Ushikubo T, Kita NT, Weisberg MK, Zolensky ME, and Ebel DS (2015) Late formation of a comet Wild 2 crystalline silicate particle, Pyxie, inferred from Al-Mg chronology of plagioclase. Earth Planet Sci. Lett 410, 54–61.

Norris TL, Gancarz AJ, Rokop DJ, and Thomas KW (1983) Half-life of $^{26}$Al. J. Geophys. Res 88, B331–B333.

Nyquist LE, Kleine T, Shih C-Y, and Reese YD (2009) The distribution of short-lived radioisotopes in the early solar system and the chronology of asteroid accretion, differentiation, and secondary mineralization. Geochim. Cosmochim. Acta 73, 5115–5136.

Ogliore RC, Huss GR, Nagashima K, Butterworth AL, Gainsforth Z, Stodolna J, Westphal AJ, Joswiak D, and Tyliszczak (2012) Incorporation of a late-forming chondrule into comet Wild 2. Astrophys. J. Lett 745, L19 (5pp).

Olsen MB, Wielandt D, Schiller M, Van Kooten EMM and Bizzarro M (2016) Magnesium and $^{54}$Cr isotope compositions of carbonaceous chondrite chondrules − Insights into early disk processes. Geochim. Cosmochim. Acta 191, 118–138. [PubMed: 27563152]

Papanastassiou DA, Bogdanovski O and Wasserburg GJ (2002) $^{53}$Mn-$^{53}$Cr systematics in Allende refractory inclusions. Meteorit. Planet. Sci 37 (Supplement), A114.

Park C, Nagashima K, Krot AN, Huss GR, Davis AM and Bizzarro M (2017) Calcium-aluminum-rich inclusions with fractionation and unidentified nuclear effects (FUN CAI): II. Heterogeneities of magnesium isotopes and $^{26}$Al in the early Solar System inferred from *in situ* high-precision magnesium-isotope measurements. Geochim. Cosmochim. Acta 201, 6–24.

Rudraswami NG and Goswami JN (2007) $^{26}$Al in chondrules from unequilibrated L chondrites: onset and duration of chondrule formation in the early solar system. Earth Planet. Sci. Lett 257, 231–244.

Rudraswami NG, Goswami JN, Chattopadhyay B, Sengupta SK, Thapliyal AP (2008) $^{26}$Al records in chondrules from unequilibrated ordinary chondrites: II. Duration of chondrule formation and parent body thermal metamorphism. Earth Planet. Sci. Lett 274, 93–102.

Rudraswami NG, Ushikubo T, Nakashima D and Kita NT (2011) Oxygen isotope systematics of chondrules in the Allende CV3 chondrite: High precision ion microprobe studies. Geochim. Cosmochim. Acta 75, 7596–7611.

Russell SDJ, Longstaffe FJ, King PL and Larsen TE (2010) The oxygen-isotope composition of chondrules and isolated forsterite and olivine grains from the Tagish Lake carbonaceous chondrite. Geochim. Cosmochim. Acta 74, 2484–2499.

Ryerson FJ and McKeegan KD (1994) Determination of oxygen self-diffusion in åkermanite, anorthite, diopside, and spinel: implications for oxygen isotopic anomalies and the thermal histories of Ca-Al-rich inclusions. Geochim. Cosmochim. Acta 58, 3713–3734.

Sakamoto N, Seto Y, Itoh S, Kuramoto K, Fujino K, Nagashima K, Krot AN and Yurimoto H (2007) Remnants of the early solar system water enriched in heavy oxygen isotopes. Science 317, 231–233. [PubMed: 17569827]

Sanders IS and Scott ERD (2012) The origin of chondrules and chondrites: debris from low-velocity impacts between molten planetesimals? Meteorit. Planet. Sci 47, 2170–2192.

Sano Y, Takada M, Takahata N, Fujiya W and Sugiura N (2014) Ion microprobe Al-Mg dating of single plagioclase grains in an Efremovka chondrule. Geochem. J 48, 133–144.

Schiller M, Baker JA and Bizzarro M (2010) $^{26}$Al-$^{26}$Mg dating of asteroidal magmatism in the young Solar System. Geochim. Cosmochim. Acta 74, 4844–4864.

Schiller M, Connelly JN, Glad AC, Mikouchi T and Bizzarro M (2015) Early accretion of protoplanets inferred from a reduced inner solar system $^{26}$Al inventory. Earth Planet. Sci. Lett 420, 45–54. [PubMed: 27429474]

Schrader DL, Franchi IA, Connolly HC Jr., Greenwood RC, Lauretta DS and Gibson JM (2011) The formation and alteration of the Renazzo-like carbonaceous chondrites I: implications of bulk-oxygen isotopic composition. Geochim. Cosmochim. Acta 101, 302–327.

Schrader DL, Connolly HC Jr., Lauretta DS, Nagashima K, Huss GR, Davidson J and Domanik KJ (2013) The formation and alteration of the Renazzo-like carbonaceous chondrites II: Linking O-isotope composition and oxidation state of chondrule olivine. Geochim. Cosmochim. Acta 101, 302–327.

Schrader DL, Nagashima K, Krot AN, Ogliore RC, Hellebrand E (2014a) Variations in the O-isotope composition of gas during the formation of chondrules from the CR chondrites. Geochim. Cosmochim. Acta 132, 50–74.

Schrader DL, Davidson J, Greenwood RC, Franchi IA and Gibson JM (2014b) A water-ice rich minor body from the early Solar System: The CR chondrite parent asteroid. Earth Planet. Sci. Lett 407, 48–60.

Schrader DL, Connolly HC Jr., Lauretta DS, Zega TJ, Davidson J and Domanik KJ (2015) The formation and alteration of the Renazzo-like carbonaceous chondrites III: towards understanding the genesis of ferromagnesian chondrules. Meteorit. Planet. Sci 50, 15–50.

Schrader DL, Nagashima K, Krot AN, Ogliore RC, Yin Q-Z, Amelin Y, Stirling CH, and Kaltenbach A (2017) Distribution of $^{26}$Al in the CR chondrite chondrule-forming region of the protoplanetary disk. Geochim. Cosmochim. Acta 201, 275–302.

Spivak-Bindorf L, Wadhwa M and Janney P (2009) $^{26}$Al-$^{26}$Mg systematics in D'Obrigny and Sahara 99555 angrites: implications for high-resolution chronology using extinct chronometers. Geochim. Cosmochim. Acta 73, 5202–5211.

Sugiura N and Fujiya W (2014) Correlated accretion ages and $\varepsilon^{54}$Cr of meteorite parent bodies and the evolution of the solar nebula. Meteorit. Planet. Sci 49, 772–787.

Teng F-Z, Li W-Y, Ke S, Marty B, Dauphas N, Huang S, Wu F-Y and Pourmand A (2010) Magnesium isotopic composition of the Earth and chondrites. Geochim. Cosmochim. Acta, 74, 4150–4166.

Tenner TJ, Ushikubo T, Kurahashi E, Kita NT and Nagahara H (2013) Oxygen isotope systematics of chondrule phenocrysts from the CO3.0 chondrite Yamato 81020: evidence for two distinct oxygen isotope reservoirs. Geochim. Cosmochim. Acta 102, 226–245.

Tenner TJ, Nakashima D, Ushikubo T, Kita NT, Weisberg MK (2015) Oxygen isotope ratios of FeO-poor chondrules in CR3 chondrites: influence of dust enrichment and $H_2O$ during chondrule formation. Geochim. Cosmochim. Acta 148, 228–250.

Tenner TJ, Kimura M and Kita NT (2017) Oxygen isotope characteristics of chondrules from the Yamato-82094 ungrouped carbonaceous chondrite: Further evidence for common O-isotope environments sampled among carbonaceous chondrites. Meteorit. Planet. Sci 52, 268–294.

Tomeoka K and Itoh D (2004) Sodium metasomatism in chondrules in CO3 chondrites: relationship to parent body thermal metamorphism. Meteorit. Planet. Sci 39, 1359–1373.

Ushikubo T, Kimura M, Kita NT and Valley JW (2012) Primordial oxygen isotope reservoirs of the solar nebula recorded in chondrules in Acfer 094 carbonaceous chondrite. Geochim. Cosmochim. Acta, 90, 242–264.

Ushikubo T, Nakashima D, Kimura M, Tenner TJ, and Kita NT (2013) Contemporaneous formation of chondrules in distinct oxygen isotope reservoirs. Geochim. Cosmochim. Acta 109, 280–295.

Ushikubo T, Tenner TJ, Hiyagon H and Kita NT (2017) A long duration of the $^{16}$O-rich reservoir in the solar nebula, as recorded in fine-grained refractory inclusions from the least metamorphosed carbonaceous chondrites. Geochim. Cosmochim. Acta 201, 103–122.

Ustunisik G, Ebel DS, Walker D, and Boesenberg JS (2014) Experimental investigation of condensation predictions for dust-enriched systems. Geochim. Cosmochim. Acta 142, 27–38.

Van Kooten EMME, Wielandt D, Schiller M, Nagashima K, Thomen A, Larsen KK, Olsen MB, Nordlund Å, Krot AN and Bizzarro M (2016) Isotopic evidence for primordial molecular cloud material in metal-rich carbonaceous chondrites. Proc. Natl. Acad. Sci 113, 2011–2016. [PubMed: 26858438]

Van Orman JA, Cherniak DJ and Kita NT (2014) Magnesium diffusion in plagioclase: Dependence on composition, and implications for thermal resetting of the $^{26}$Al-$^{26}$Mg early solar system chronometer. Earth Planet. Sci. Lett 385, 79–88.

Villeneuve J, Chaussidon M, and Libourel G (2009) Homogeneous distribution of $^{26}$Al in the solar system from the Mg isotopic composition of chondrules. Science 325, 985–988. [PubMed: 19696348]

Wadhwa M, Kita NT, Nakashima D, Bullock ES, MacPherson GJ and Bouvier A (2014) High precision $^{26}$Al-$^{26}$Mg isotope systematics for an almost pristine refractory inclusion: implications for the absolute age of the solar system. 45th Lunar and Planet. Sci. Conf. CD-ROM. #2698.

Walsh KJ, Morbidelli A, Raymond SN, O'Brien DP and Mandell A (2011) Sculpting of the inner solar system by gas-driven orbital migration of Jupiter. Nature 475, 206–209. [PubMed: 21642961]

Walsh KJ, Morbidelli A, Raymond SN, O'Brien DP and Mandell A (2012) Populating the asteroid belt from two parent source regions due to the migration of giant planets− "The Grand Tack". Meteorit. Planet. Sci 47, 1941–1947.

Warren PH (2011) Stable-isotopic anomalies and the accretionary assemblage of the Earth and Mars: A subordinate role for carbonaceous chondrites. Earth Planet. Sci. Lett 311, 93–100.

Weisberg MK, Prinz M, Clayton RN and Mayeda TK (1993) The CR (Renazzo-type) carbonaceous chondrite group and its implications. Geochim. Cosmochim. Acta 57, 1567–1586.

Wick MJ and Jones RH (2012) Formation conditions of plagioclase-bearing type I chondrules in CO chondrites: a study of natural samples and experimental analogs. Geochim. Cosmochim. Acta 98, 140–159.

Yamanobe M, Nakamura T and Nakashima D (2018) Oxygen isotope reservoirs in the outer asteroid belt inferred from oxygen isotope systematics of chondrule olivines and isolated forsterite and olivine grains in Tagish Lake-type carbonaceous chondrites, WIS 91600 and MET 00432. Polar Sci. 15, 29–38.

Young ED and Russell SS (1998) Oxygen reservoirs in the early solar nebula inferred from an Allende CAI. Science 282, 452–455.

Yu Y, Hewins RH, Clayton RN and Mayeda TK (1995) Experimental study of high temperature oxygen isotope exchange during chondrule formation. Geochim. Cosmochim. Acta 59, 2095–2104.

Zanda B, Bourot-Denise M, Perron C and Hewins RH (1994) Origin and metamorphic redistribution of silicon, chromium, and phosphorous in the metal of chondrites. Science 265, 1846–1849. [PubMed: 17797224]

Zolensky ME, Zega TJ, Yano H, Wirick S, Westphal AJ, Weisberg MK, Weber I, Warren JL, Velbel MA, Tsuchiyama A, Tsou P, Toppani A, Tomioka N, Tomeoka K, Teslich N, Taheri M, Susini J, Stroud R, Stephan T, Stadermann FJ, Snead CJ, Simon SB, Simionovici A, See TH, Robert F, Rietmeijer FJM, Rao W, Perronnet MC, Papanastassiou DA, Okudaira K, Ohsumi K, Meibom A, Matrajt G, Marcus MA, Leroux H, Lemelle L, Le L, Lanzirotti A, Langenhorst F, Krot AN, Keller LP, Kearsley AT, Joswiak D, Jacob D, Ishii H, Harvey R, Hagiya K, Grossman L, Grossman JN, Graham GA, Gounelle M, Gillet P, Genge MJ, Flynn G, Ferroir T, Fallon S, Ebel DS, Dai ZR, Cordier P, Clark B, Chi M, Butterworth AL, Brownlee DE, Bridges JC, Brennan S, Brearley A, Bradley JP, Bleuet P, Bland PA, Bastien R (2006) Mineralogy and petrology of Comet 81P/Wild 2 nucleus samples. Science 314, 1735–1739. [PubMed: 17170295]

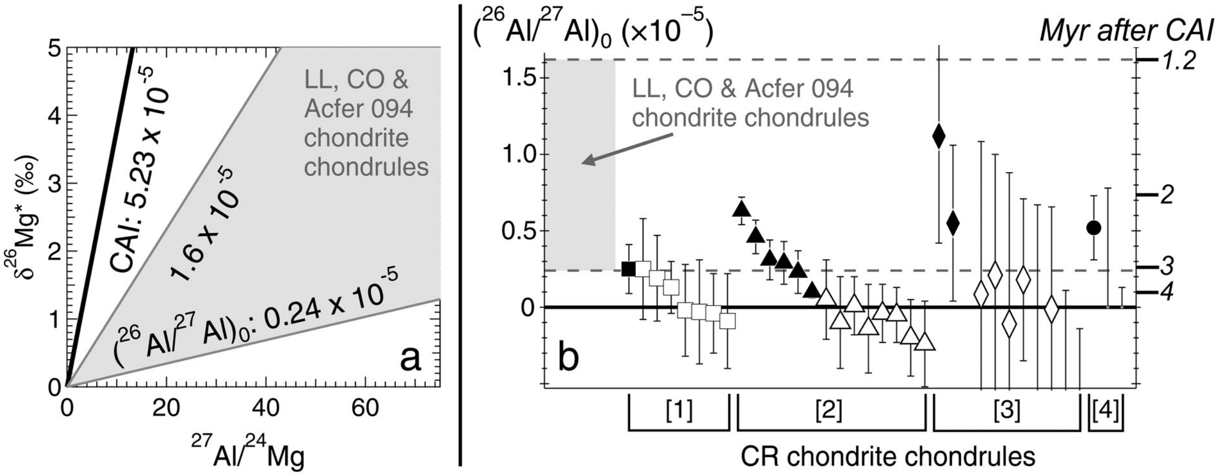

**Fig. 1.**

(a) Representative isochrons for canonical CAIs (e.g. Jacobsen et al. 2008; MacPherson et al. 2010) and the ranges from Semarkona (LL3.01), Yamato 81020 (CO3.05), and Acfer 094 (ungr. C3.00) chondrite chondrules (Hutcheon and Hutchison 1989; Kita et al. 2000; Kunihiro et al. 2004; Kurahashi et al. 2008a; Rudraswami et al. 2008; Villeneuve et al. 2009; Hutcheon et al. 2009; Ushikubo et al. 2013). *δ$^{26}$Mg is defined in Section 2.5.1 of the main text. Slopes of isochrons correspond to inferred $(^{26}Al/^{27}Al)_0$. (b) CR chondrite chondrule $(^{26}Al/^{27}Al)_0$ values (symbols) versus the range of chondrule $(^{26}Al/^{27}Al)_0$ from LL3, CO3, and Acfer 094 chondrites (gray shading and dashed lines). Relative ages are calculated using the canonical $(^{26}Al/^{27}Al)_0$ shown in (a), and a $^{26}$Al half-life of 0.705 Myr (Norris et al. 1983). For CR chondrite chondrule data, references 1–4 correspond to Schrader et al. (2017), Nagashima et al. (2014), Hutcheon et al. (2009), and Kurahashi et al. (2008b), respectively. Closed and open symbols correspond to chondrules with and without resolvable excess $^{26}$Mg, respectively. Three chondrules from Hutcheon et al. (2009) were re-measured by Nagashima et al. (2014); only the data from the latter study are shown. $(^{26}Al/^{27}Al)_0$ values and uncertainties from Hutcheon et al. (2009) were determined using Isoplot. Data from Kurahashi et al. (2008b) with unresolvable excess $^{26}$Mg are only reported as $(^{26}Al/^{27}Al)_0$ upper limits (hence, no symbols are shown).

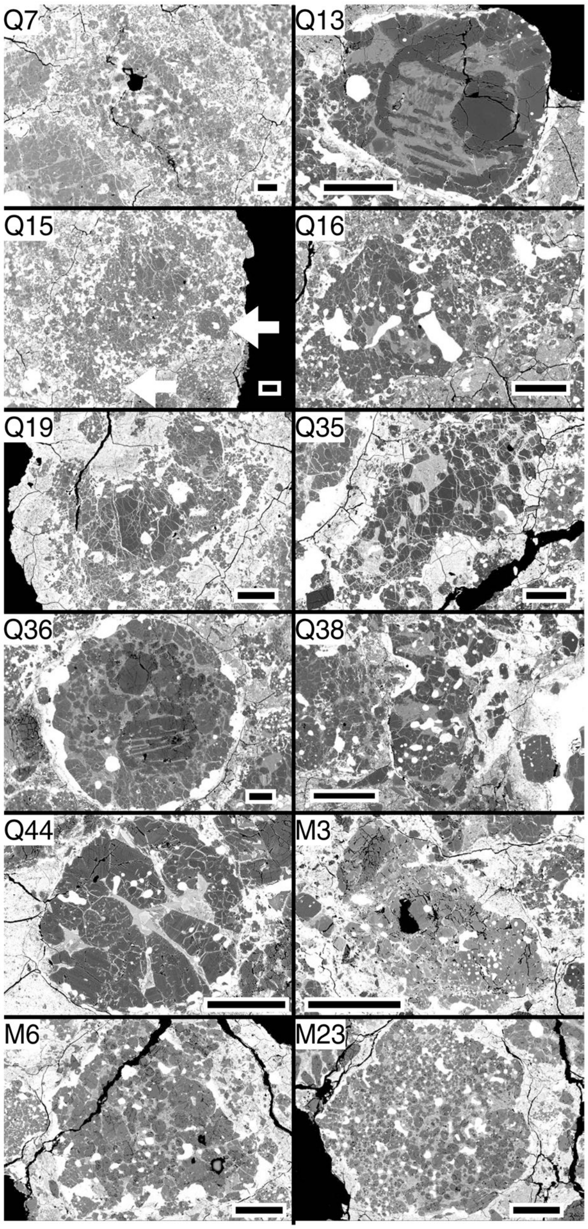

**Fig. 2.**

Backscattered electron images of QUE 99177 (Q-designation) and MET 00426 (M-designation) chondrules studied for their Al-Mg isotope systematics. Scale bars are 200 μm. All chondrules are FeO-poor; Q7, Q16, Q19, Q35, Q38, Q44, M6, and M23 are type I porphyritic olivine-pyroxene (POP: 20–80% modal olivine, when considering only olivine and pyroxene); M3 is type I porphyritic pyroxene (PP: <20% modal olivine); Q13 and Q36 are type I compound chondrules, each with barred olivine (BO) and POP features; Q15 is a layered chondrule that is type I POP textured with smaller chondrules along the periphery (white arrows).

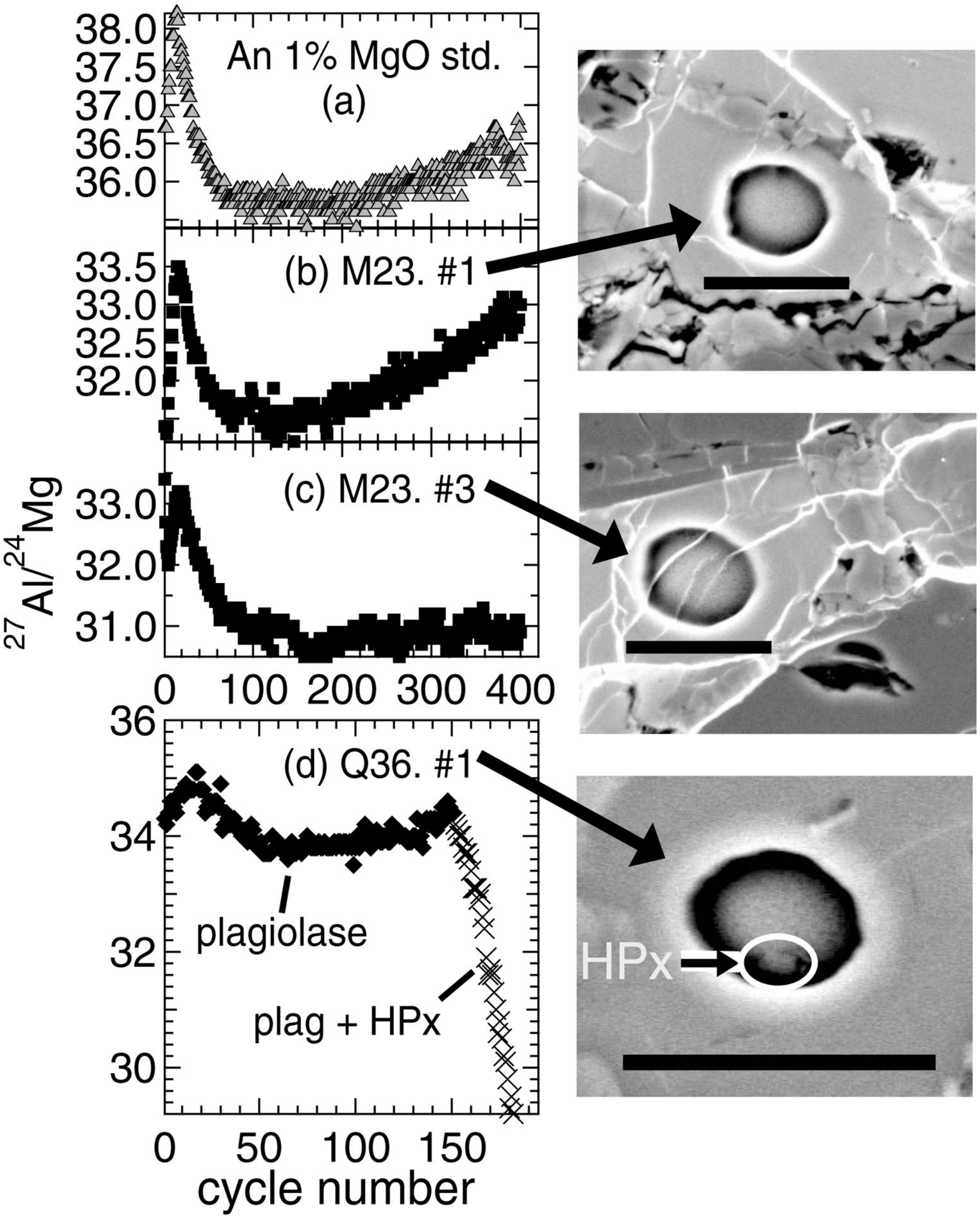

**Fig. 3.**

Example $^{27}$Al/$^{24}$Mg ratios versus cycle number for (a) the anorthite glass running standard with 1 wt. % MgO, and for (b-d) chondrule plagioclase. Increasing cycle numbers represent greater sputtering depth into samples. The shape of the $^{27}$Al/$^{24}$Mg versus cycle number trend is likely related to the SIMS sputtering behavior of the sample, while differences in $^{27}$Al/$^{24}$Mg ranges among samples represent variability in plagioclase compositions. BSE images of SIMS pits associated with (b-d) are also shown, where scale bars are 10 µm. In (b) and (c), chondrule $^{27}$Al/$^{24}$Mg versus cycle number patterns approximate that of the anorthite running standard, suggesting the analyses were not compromised by inadvertent measurement of pyroxene grains. The image affiliated with (c) demonstrates that overlap with thin strands of an Fe-rich phase does not compromise data quality. In (d) the significant

$^{27}$Al/$^{24}$Mg decrease after the first 150 cycles indicates partial analysis of an unwanted phase. SEM imaging and EDS of the subsequent SIMS pit confirmed the presence of a small high-Ca pyroxene (HPx) grain. Therefore, only the first 150 cycles of this analysis were used to calculate the Al-Mg isotope systematics.

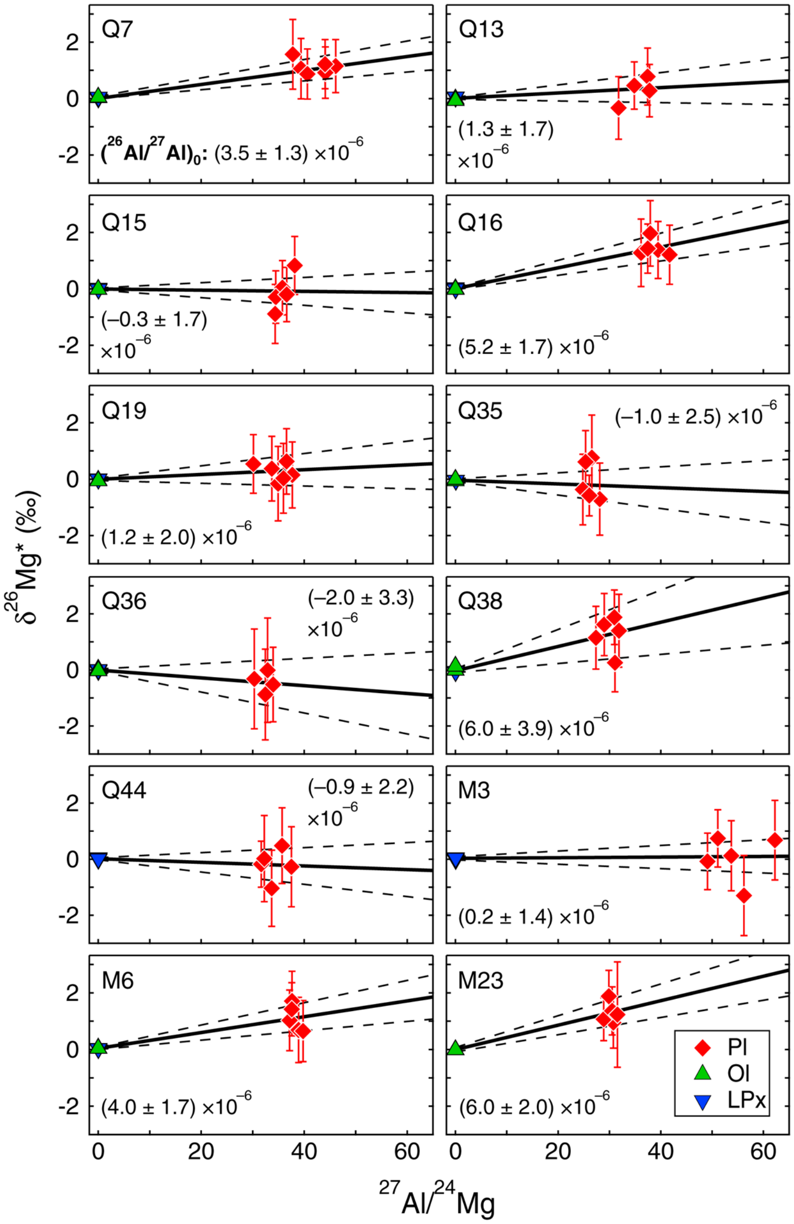

**Fig. 4.**

Al-Mg isochron diagrams from each chondrule studied. Error envelopes are 95% confidence. Inferred initial $(^{26}Al/^{27}Al)_0$ ratios are determined from slopes of regression lines. Mineral data are from Table 2.

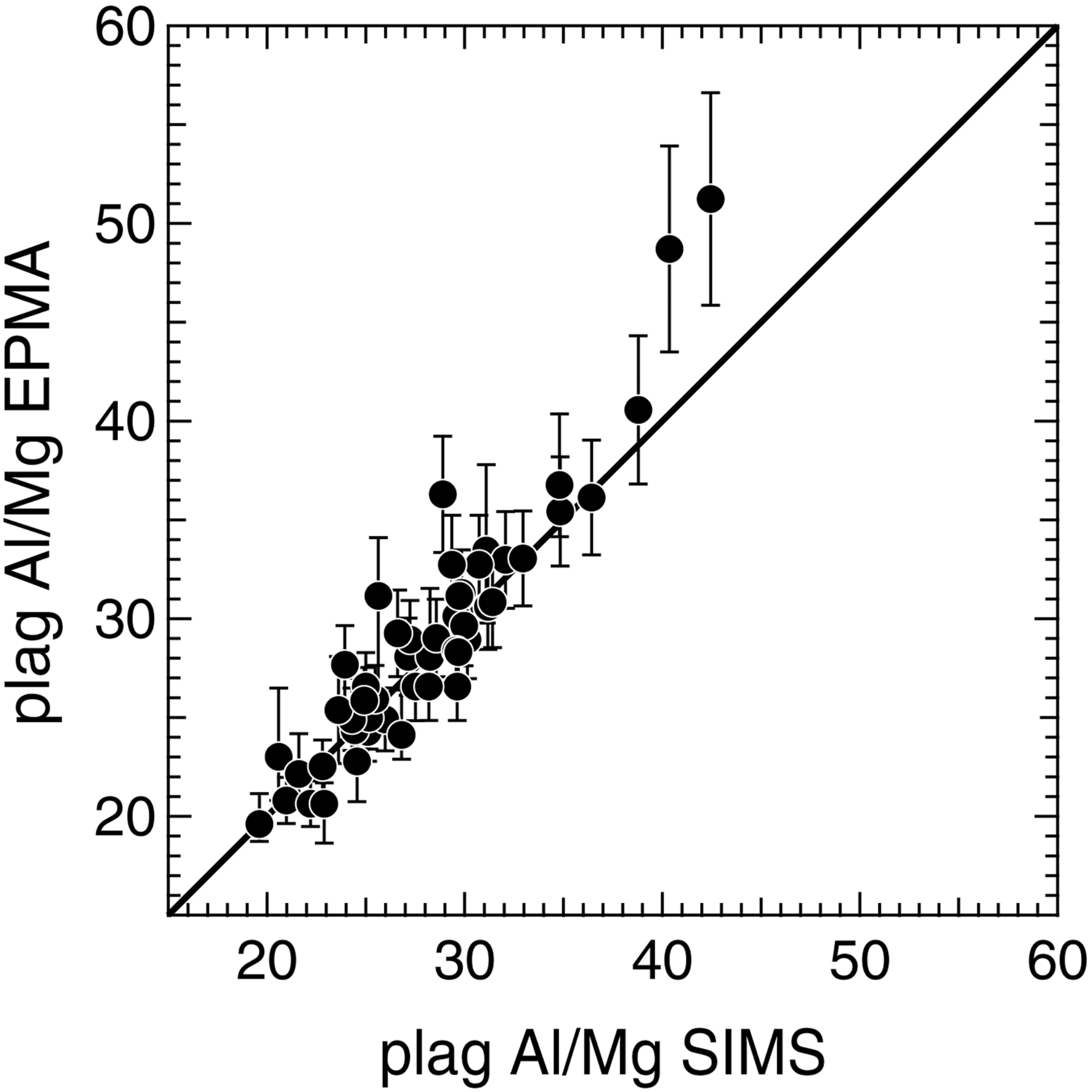

**Fig 5.**

Plagioclase Al/Mg comparisons of regions analyzed by EPMA and by SIMS. Al/Mg ratios by SIMS are calculated by multiplying the measured $^{27}Al/^{24}Mg$ by the fraction of Mg measured as $^{24}Mg$. EPMA uncertainties represent the maxima of (1) the range of values per region analyzed (1 to 5 EPMA measurements were collected per spot analyzed by SIMS); or (2) the uncertainties of Al and Mg from measurements of plagioclase standards as unknowns (Table 1). SIMS uncertainties are the $^{27}Al/^{24}Mg$ values given in Table 2, and are smaller than the symbols.

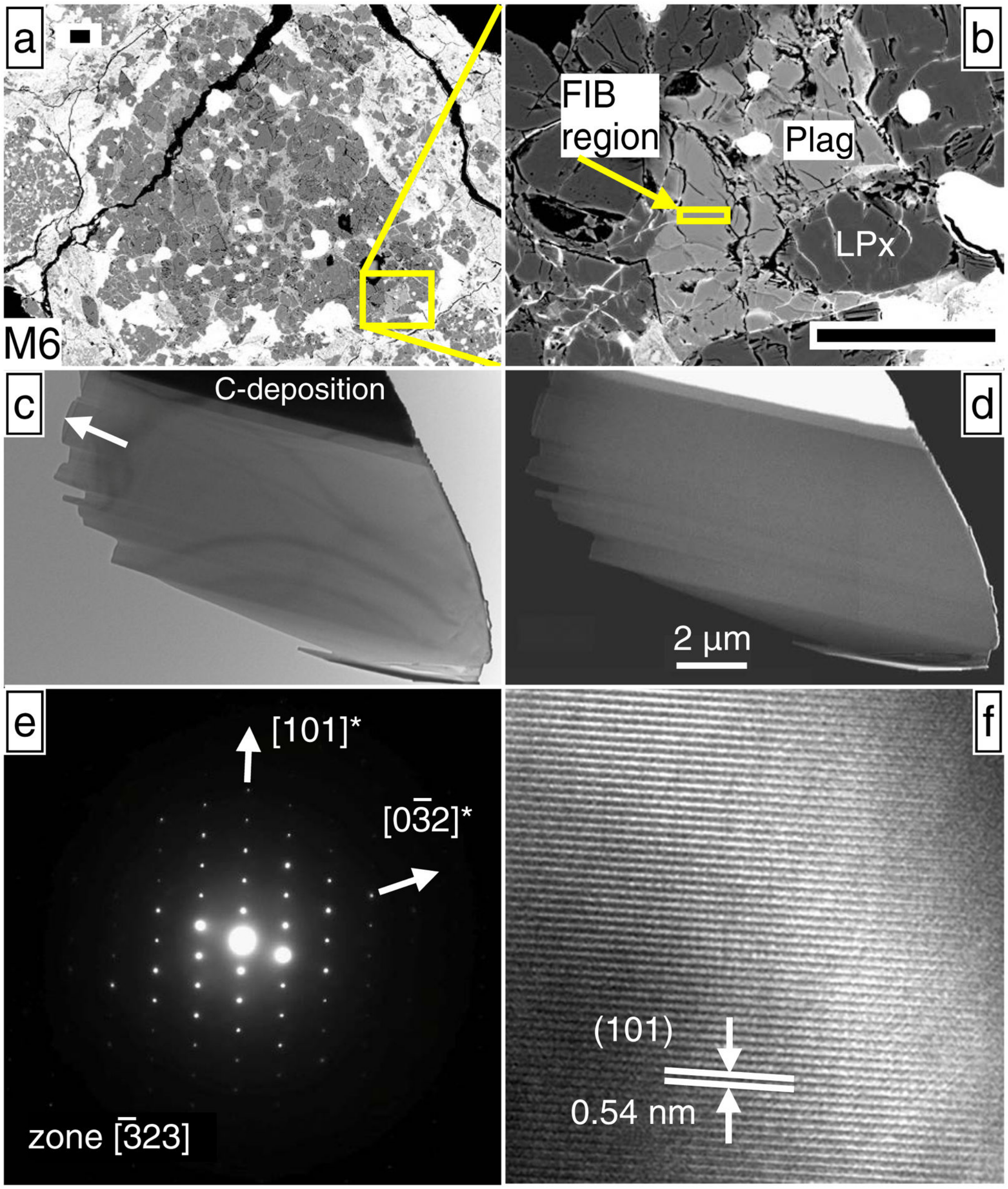

**Fig. 6.**

Electron micrographs of plagioclase from chondrule M6, which has resolvable excess $^{26}$Mg (Table 2; Fig. 4). (a) and (b) SEM images of plagioclase sectioned by FIB, where scale bars are 50 µm. (c) Bright-field TEM image of the plagioclase section. The sample appears as a single crystal, largely free of inclusions and defects, except for a small number of dislocations in the bottom right corner. The arrow corresponds to the surface of the meteorite thin section; about 1/3 of the FIB section was lost due to a pre-existing crack. (d) HAADF-STEM (Z-contrast image), showing the sample is chemically homogeneous (elemental EDS maps also show homogeneity in Electronic Appendix EA6). (e) Selected area electron diffraction (SAED) pattern consistent with only an unmodified anorthite structure and showing no superlattice reflections. (f) High resolution TEM (HRTEM) image, showing no inclusions are present, even down to the nm-scale.

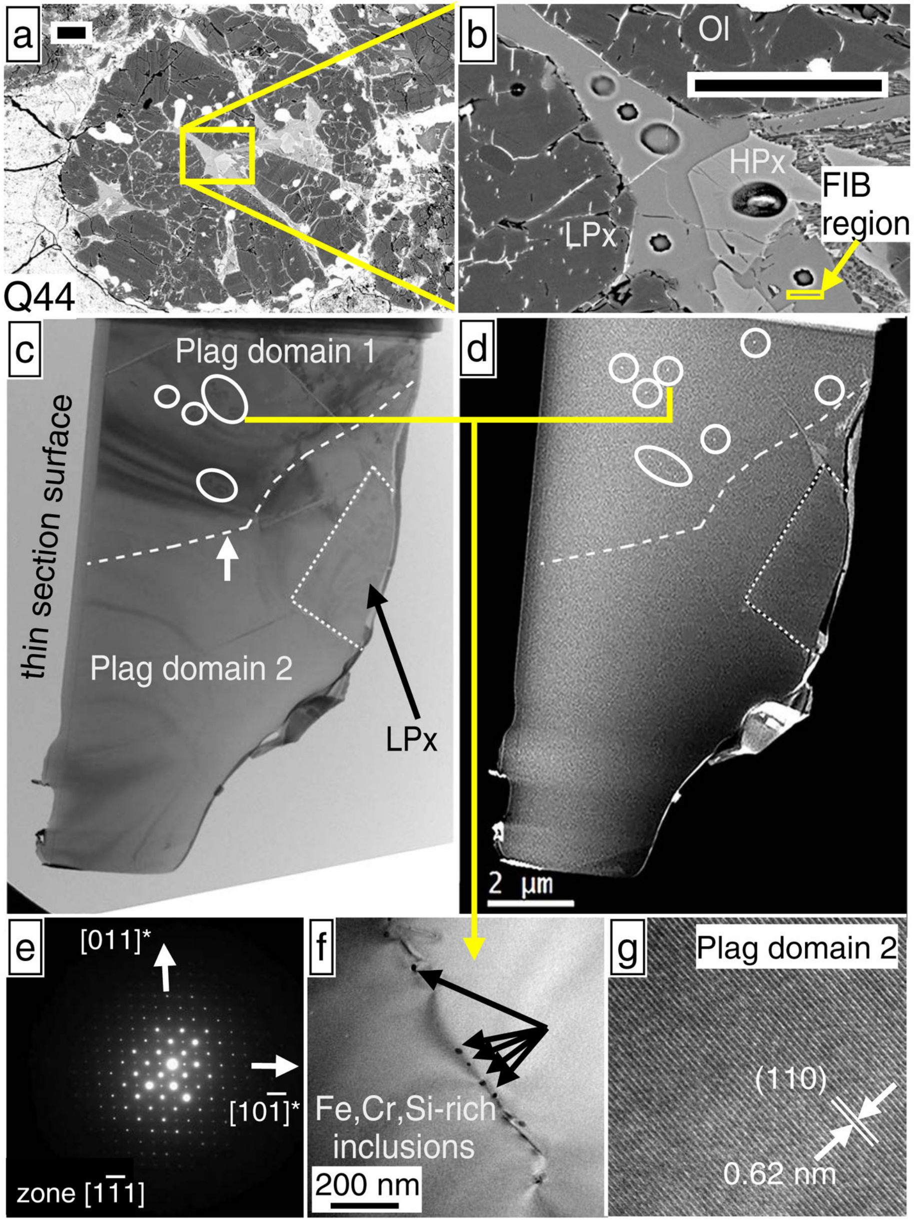

**Fig. 7.**

Electron micrographs of plagioclase from chondrule Q44, which has no resolvable excess $^{26}$Mg (Table 2; Fig. 4). (a) and (b) SEM images of plagioclase sectioned by FIB, where scale bars are 50 μm. SIMS pits from plagioclase Al-Mg isotope analyses, as well as a high-Ca pyroxene O-isotope analysis, are visible in (b). (c) thin-foil TEM image of the plagioclase section, consisting of a plagioclase grain and a low-Ca pyroxene grain, separated by a dotted line. The plagioclase is divided into two domains (dashed line; white arrow) by a subgrain boundary consisting of dislocation arrays. Color bands in the image correspond to thickness fringes. The thin gray layer running parallel to the thin section surface is a carbon deposit. Circled regions correspond to free dislocations. (d) HAADF-STEM Z-contrast image. Circled regions depict sub-micron-sized inclusions appearing as tiny bright dots. With the exception of these inclusions, the plagioclase is chemically homogeneous (elemental EDS maps are provided in Electronic Appendix EA6). (e) SAED pattern of plagioclase, showing a diffraction pattern consistent with only an unmodified anorthite structure and showing no superlattice reflections. (f) Bright-field TEM image of a dislocation region in plagioclase domain 1 and associated Fe,Cr,Si-rich inclusions as determined by EDS. (g) HRTEM image of a region analyzed in plagioclase domain 2, which does not have dislocations or inclusions down to the nm-scale.

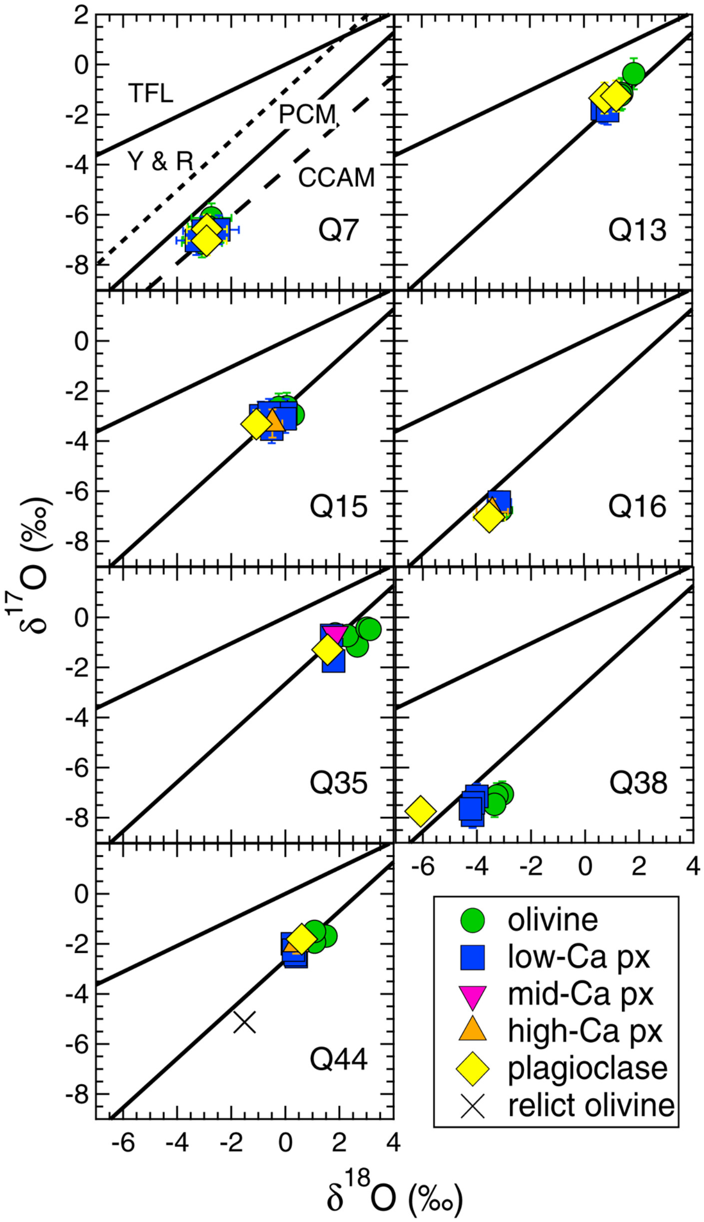

**Fig. 8.**

Inter-mineral oxygen isotope ratios of chondrules from this study that have plagioclase data for comparison. Oxygen isotope data are from Tenner et al. (2015). Low-, mid-, and high-Ca pyroxene data have wollastonite endmember contents of 0.8–3, 7–9, and 33–37, respectively. Uncertainties are the 2SD external reproducibility of bracketing standard measurements. Shown are the primitive chondrule mineral (PCM; Ushikubo et al. 2012), carbonaceous chondrite anhydrous mineral (CCAM; Clayton et al. 1977), Young and Russell (1998), and terrestrial fractionation lines.

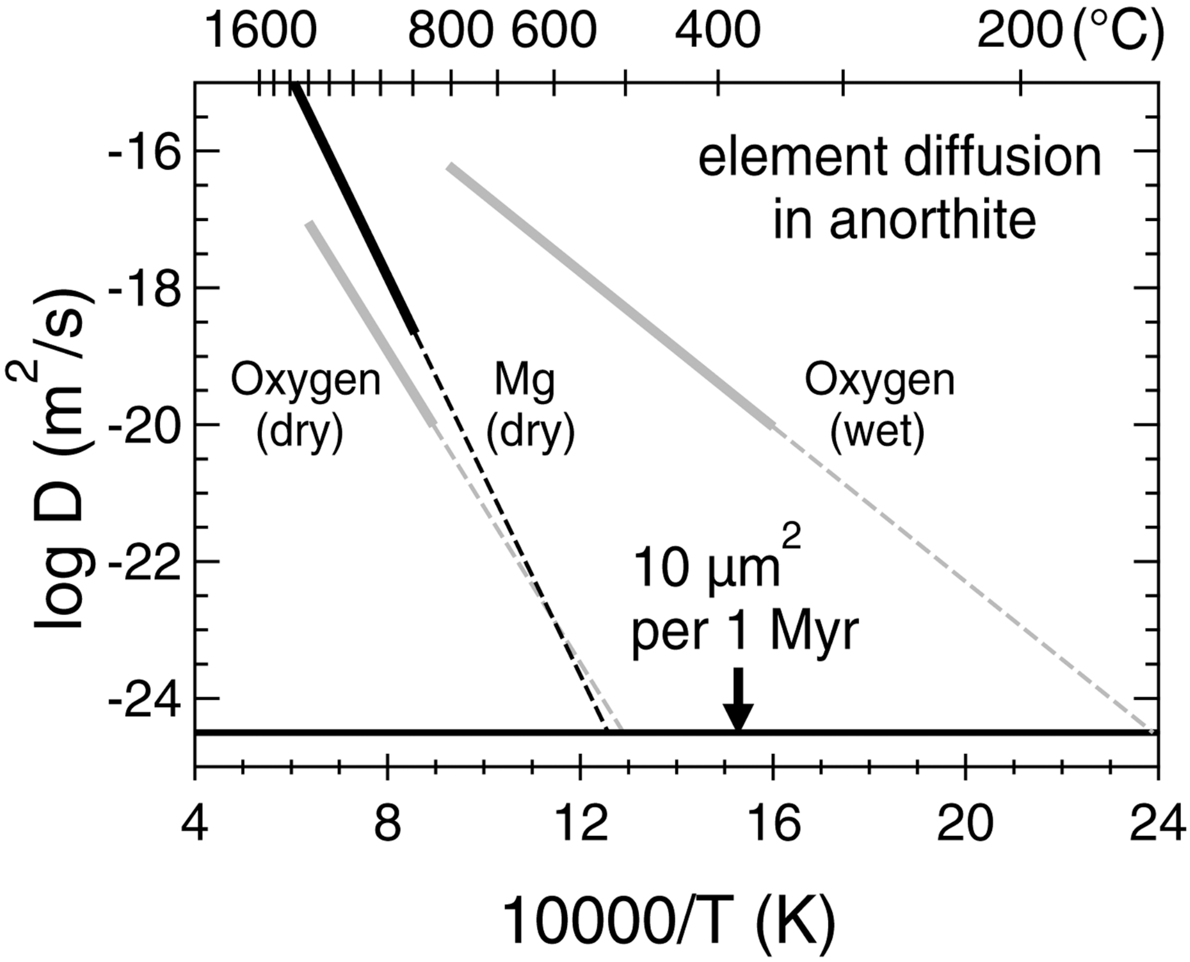

**Fig. 9.**

Oxygen and Mg diffusion in anorthite. Solid lines are fits to experimental data, and dashed lines are extrapolations to sustained temperatures required for 10 µm$^2$ of diffusion per 1 million years. Dry oxygen diffusion data: Ryerson and McKeegan (1994). Wet oxygen diffusion data: Giletti et al. (1978). Dry Mg diffusion data: LaTourrette and Wasserburg (1998) and Orman et al. (2014).

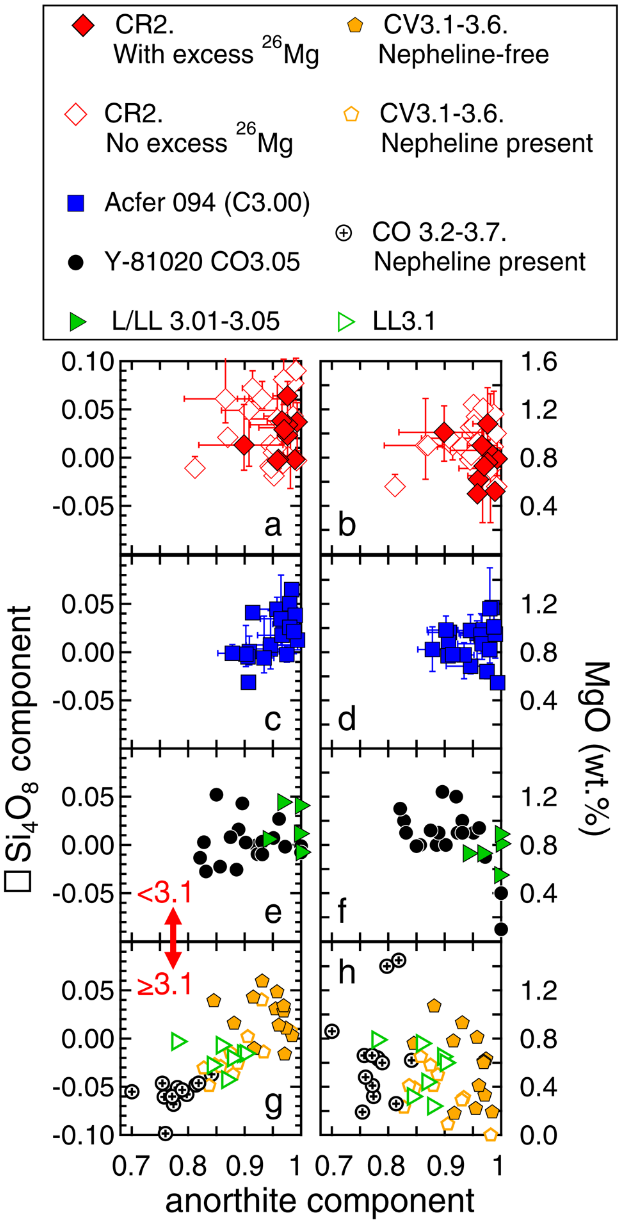

**Fig. 10.**

Plagioclase excess silica (left panels) and MgO (right panels) as a function of anorthite content from various carbonaceous and ordinary chondrite FeO-poor chondrules. For reference, the reported anorthite content is normalized only to the An + Ab + K-feldspar contents. All EPMA data are compiled in Appendix EA1, and plagioclase components are calculated according to methods used in Beaty and Albee (1980). Data sources: CR2 data: Nagashima et al. (2014); Schrader et al. (2017); this study. Acfer 094 data: Appendix EA1, from chondrules studied by Ushikubo et al. (2012). Y-81020 CO3.05 data: Kurahashi et al. (2008); Tenner et al. (2013). L/LL3.01–3.05 data: Hutcheon and Hutchison (1989); Kita et al. (2000); Rudraswami and Goswami (2007). CV3.1–3.6 data: Kimura and Ikeda (1995; 1998); Krot et al. (2002); Jones and Schilk (2009); Nagashima et al. (2017). CO3.2–3.7 data:

Tomeoka and Itoh (2004); Wick and Jones (2012). L and LL3.1 data: Mostefaoui et al. (2002); Rudraswami and Goswami (2007). When available, uncertainties represent the range of values from EPMA datasets (Appendix EA1).

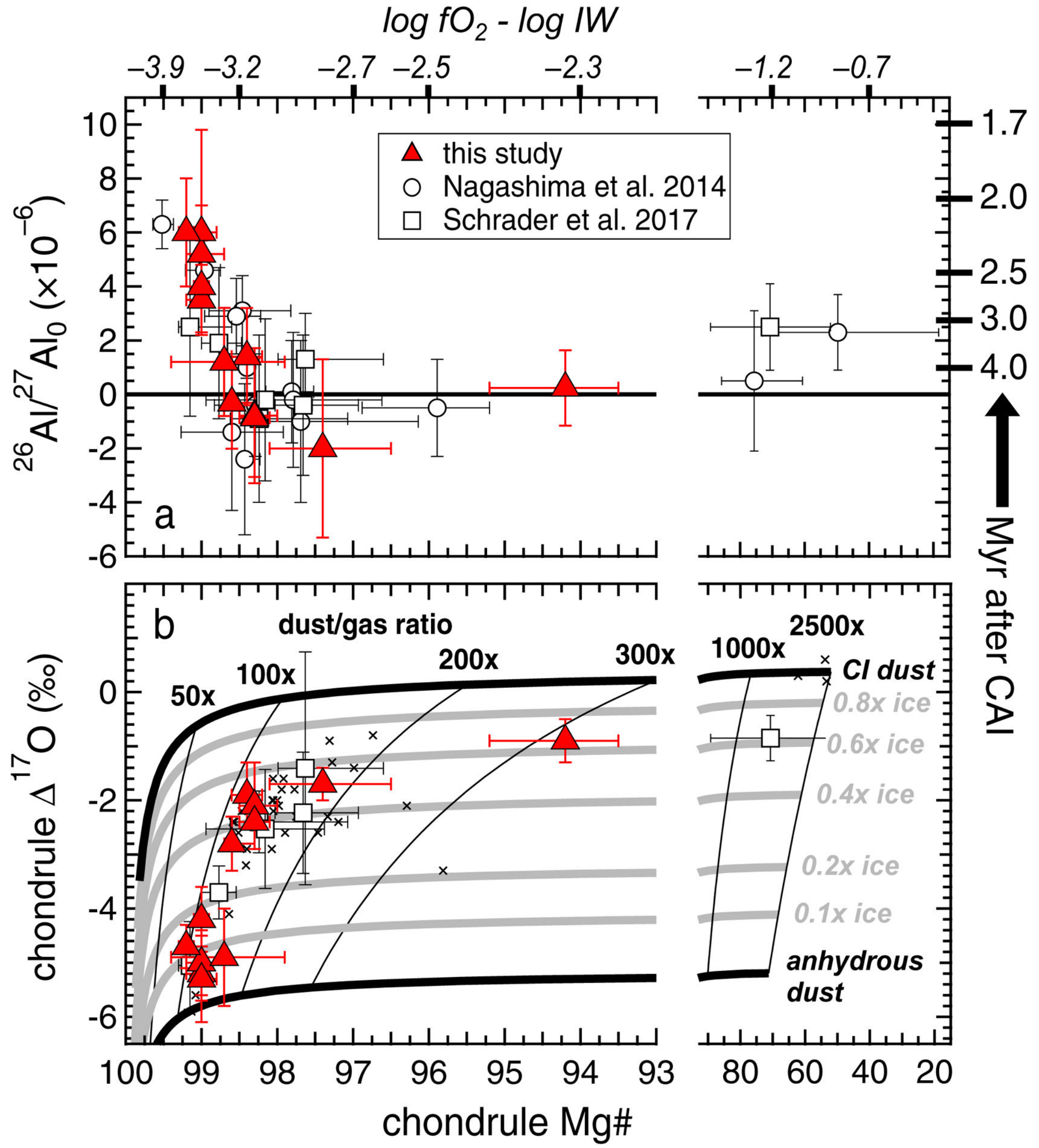

**Fig. 11.**

(a) Chondrule Mg# versus $(^{26}Al/^{27}Al)_0$. Relative ages are calculated according to Eqn. 1 in the text, using a canonical $(^{26}Al/^{27}Al)_0$ of $5.23 \times 10^{-5}$. In order to provide a direct comparison, chondrule Mg#'s and uncertainties from Nagashima et al. (2014) (Appendix EA7) and Schrader et al. (2017) are recalculated using definitions from Tenner et al. (2015), as detailed in 4.3.1 of the text. Oxygen fugacities (relative to the Fe-wüstite buffer) during chondrule formation are based on metal-silicate phase equilibria (Eqn. 2 in the text). (b) Corresponding chondrule Mg# versus $\Delta^{17}O$ data from this study and from Schrader et al. (2017). Small cross symbols are additional data from Tenner et al. (2015) that have no current Al-Mg isotope systematics. $\Delta^{17}O$ data from Tenner et al. (2015) and Schrader et al. (2017) are the average and 2SD of all individual measurements per chondrule, excluding relict grains. Shown also is the mass balance model from Tenner et al. (2015), in which dust and gas compositions are based on those from Anders and Grevesse (1989) and Allende Prieto et al. (2001; 2002). Dust to gas ratios are shown as thin semi-vertical lines, and $H_2O$ ice abundances in the dust (thick semi-horizontal lines) are given relative to that in CI dust. Details of the model are given in Section 4.3.2.

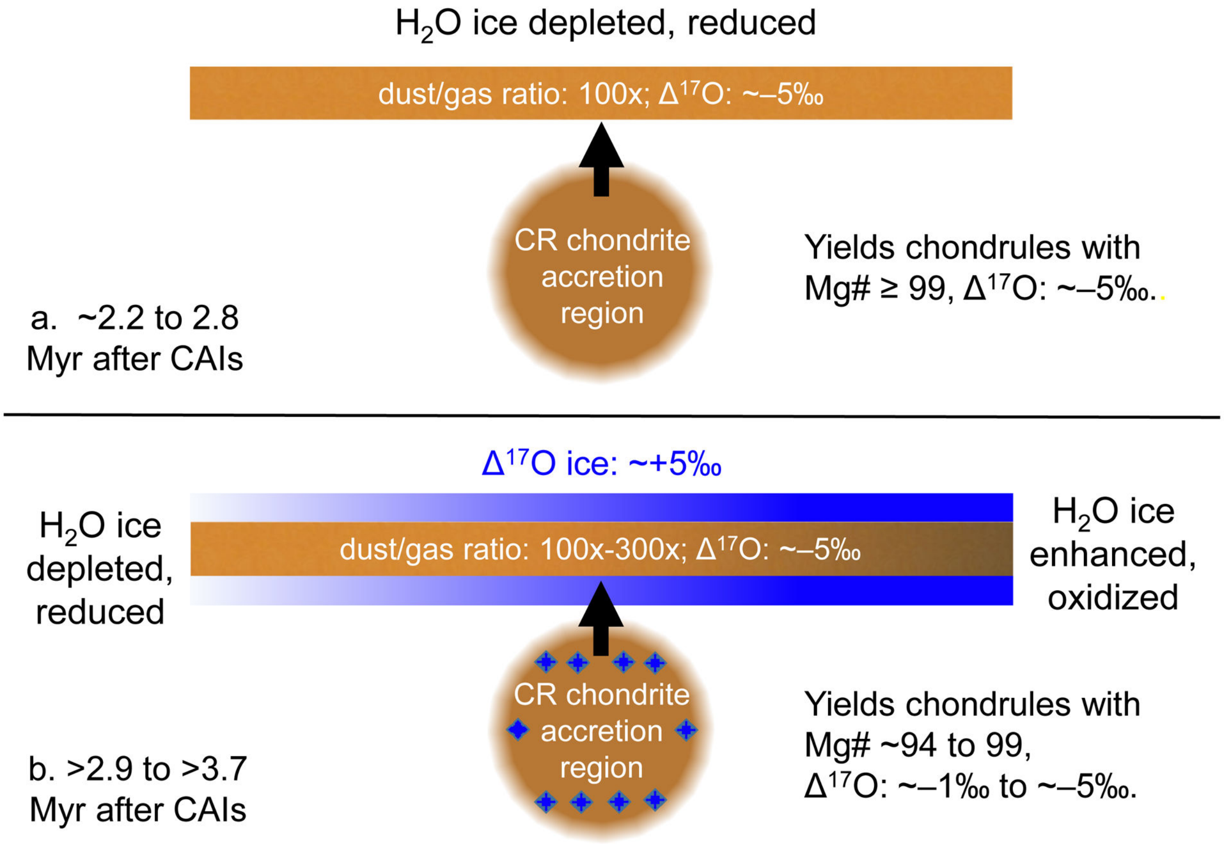

**Fig. 12.**

Cartoon interpretation of ice migration into the CR chondrite chondrule forming environment, based on (1) the Mg#'s, $\Delta^{17}$O values, and inferred $(^{26}\text{Al}/^{27}\text{Al})_0$ values of chondrules from this study, and (2) dust enrichment and ice enhancement parameters modeled by Tenner et al. (2015). See also: Fig. 11.

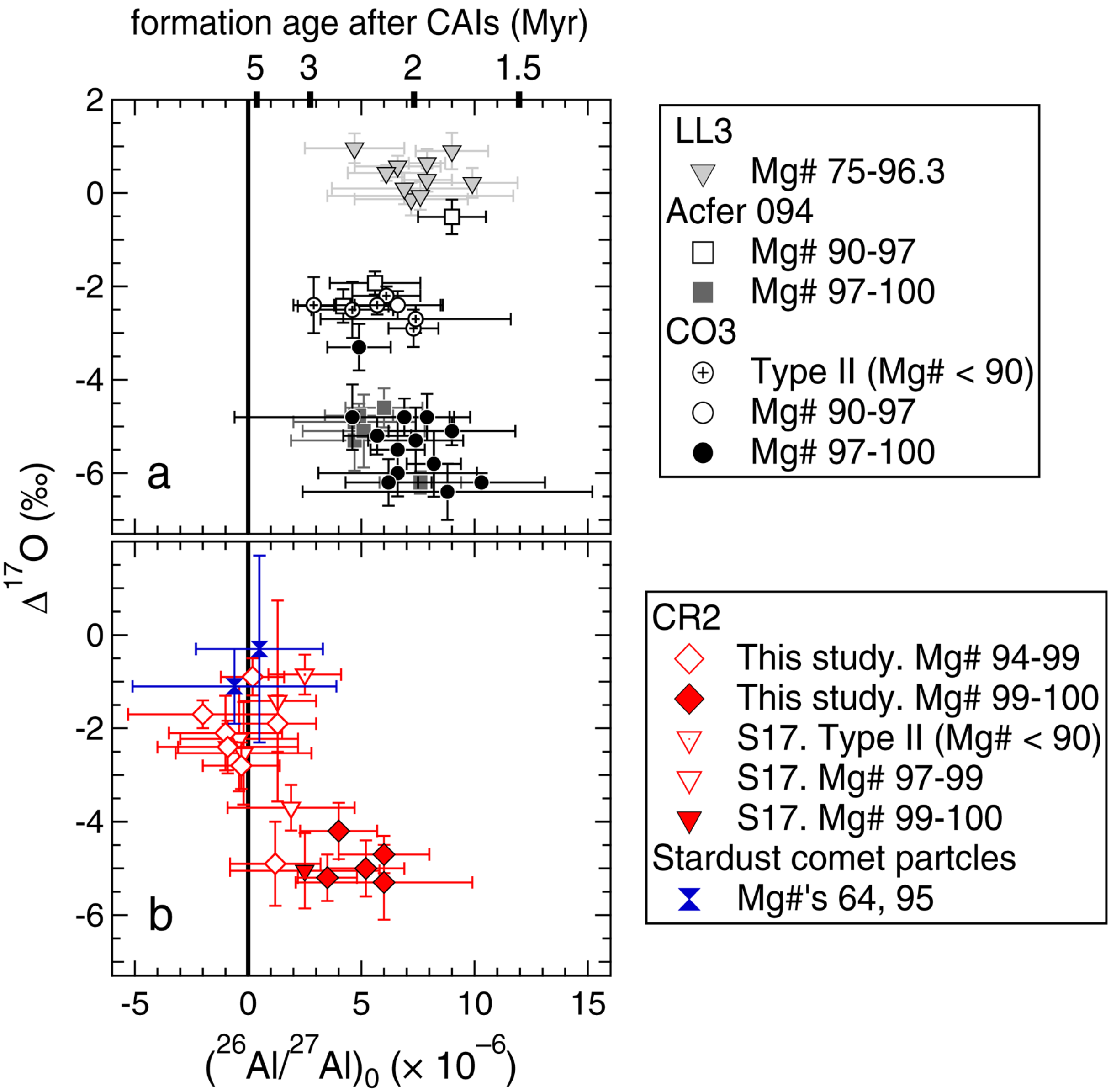

**Fig. 13.**

$(^{26}Al/^{27}Al)_0$ vs. $\Delta^{17}O$ for (a) LL3 (Kita et al. 2000; 2010), Acfer 094 (Ushikubo et al., 2012; 2013), and CO3 (Kurahashi et al., 2008; Tenner et al. 2013) chondrite chondrules, and for (b) CR2 chondrite chondrules (this study; Schrader et al., 2017: S17) and Stardust comet particles Iris (Ogliore et al., 2012) and Pyxie (Nakashima et al., 2012; 2015). Mg# ranges and uncertainties are as reported in each study, with the exception of chondrule Mg#'s from Schrader et al., 2017, which are recalculated as described in section 4.3.1.. Relative ages are calculated according to Eqn. 1 and use a canonical CAI $(^{26}Al/^{27}Al)_0$ of $5.23 \times 10^{-5}$ (Jacobsen et al., 2008; MacPherson et al., 2010).

## Table 1.

Plagioclase EPMA data from chondrules and standards analyzed in the same session

| | Q7 | ±(a) | Q13 | ± | Q15 | ± | Q16 | ± | Q19 | ± | Q35 | ± | $An_{78}$ std as unk | ± | $An_{78}$ std value(e) |
|---|---|---|---|---|---|---|---|---|---|---|---|---|---|---|---|
| **wt. %** | | | | | | | | | | | | | | | |
| $SiO_2$ | 46.36 | *0.74,0.72* | 47.28 | *1.32,1.80* | 47.03 | *0.85,1.08* | 46.90 | *2.24,1.16* | 49.99 | *0.57,0.89* | 49.11 | *1.88,1.17* | 49.16 | *0.36,0.31* | 49.00 |
| $AI2O_3$ | 33.29 | *0.97,0.86* | 32.10 | *1.71,1.20* | 32.62 | *0.73,0.57* | 33.02 | *0.60,1.70* | 30.69 | *0.97,0.88* | 30.80 | *1.14,1.45* | 32.49 | *0.32,0.41* | 32.90 |
| FeO | 0.39 | *0.66,0.20* | 0.23 | *0.38,0.24* | 0.59 | *0.37,0.26* | 0.52 | *0.48,0.29* | 0.33 | *0.26,0.12* | 0.55 | *0.58,0.39* | 0.40 | *0.13,0.15* | 0.37 |
| MgO | 0.79 | *0.09,0.14* | 0.92 | *0.26,0.31* | 0.89 | *0.23,0.20* | 0.86 | *0.09,0.10* | 0.90 | *0.11,0.12* | 1.16 | *0.19,0.29* | 0.13 | *0. 04,0.06* | 0.12 |
| CaO | 19.11 | *0.52,0.44* | 18.55 | *0.51,0.66* | 18.85 | *0.47,0.35* | 18.90 | *0.54,1.38* | 17.34 | *0.34,0.68* | 18.30 | *0. 58,1.42* | 15.51 | *0. 30,0.29* | 15.75 |
| $Na_2O$ | 0.07 | *0.06,0.05* | 0.42 | *0.60,0.31* | 0.14 | *0.10,0.08* | 0.24 | *0.66,0.22* | 0.83 | *0.17,0.11* | 0.12 | *0.09,0.05* | 2.49 | *0.09,0.09* | 2.53 |
| total | 100.01 | *0.84,1.20* | 99.50 | *1.28,0.80* | 100.22 | *0.66,0.62* | 100.44 | *0.41,1.07* | 100.07 | *0.70,0.89* | 100.14 | *0.89,1.01* | 100.35 | *0.38,0.58* | 100.74 |
| *n* | 72 | | 46 | | 27 | | 25 | | 8 | | 37 | | 11 | | |
| **cations**(b) | | | | | | | | | | | | | | | |
| Si | 2.137 | *0.028,0.038* | 2.185 | *0.054,0.074* | 2.165 | *0.026,0.039* | 2.152 | *0.090,0.042* | 2.283 | *0.038,0.042* | 2.251 | *0.091,0.046* | 2.242 | *0.015,0.011* | 2.228 |
| Al | 1.807 | *0.040,0.035* | 1.747 | *0.080,0.070* | 1.768 | *0.048,0.048* | 1.785 | *0.037,0.096* | 1.650 | *0.052,0.038* | 1.662 | *0.058,0.075* | 1.745 | *0.015,0.015* | 1.761 |
| Fe2+ | 0.015 | *0.025,0.007* | 0.009 | *0.014,0.009* | 0.022 | *0.029,0.010* | 0.020 | *0.018,0.011* | 0.013 | *0.010,0.005* | 0.021 | *0.023,0.015* | 0.015 | *0.005,0.006* | 0.014 |
| Mg | 0.054 | *0.006,0.010* | 0.063 | *0.019,0.021* | 0.061 | *0.015,0.013* | 0.059 | *0.006,0.006* | 0.061 | *0.007,0.008* | 0.079 | *0.013,0.020* | 0.009 | *0. 003,0.004* | 0.008 |
| Ca | 0.943 | *0.024,0.022* | 0.918 | *0.027,0.032* | 0.929 | *0.026,0.022* | 0.929 | *0.028,0.073* | 0.848 | *0.011,0.029* | 0.898 | *0.026,0.068* | 0.757 | *0.013,0.015* | 0.766 |
| Na | 0.007 | *0.005,0.005* | 0.037 | *0.054,0.027* | 0.012 | *0.011,0.008* | 0.021 | *0.058,0.020* | 0.074 | *0.015,0.010* | 0.011 | *0.008,0.004* | 0.220 | *0.007,0.007* | 0.223 |
| total | 4.963 | *0.023,0.017* | 4.960 | *0.034,0.034* | 4.957 | *0.017,0.020* | 4.966 | *0.035,0.029* | 4.928 | *0.020,0.013* | 4.923 | *0.018,0.052* | 4.996 | *0.008,0.009* | 5.001 |
| **endmembers**(c) | | | | | | | | | | | | | | | |
| $Ca(Fe,Mg)Si_3O_8$ | 0.056 | *0.018,0.010* | 0.068 | *0.023,0.020* | 0.067 | *0.042,0.011* | 0.063 | *0.009,0.011* | 0.066 | *0.017,0.010* | 0.086 | *0.020,0.032* | 0.013 | *0.010,0.010* | 0.011 |
| $NaAISi_3O_8$ | 0.007 | *0.005,0.005* | 0.037 | *0.054,0.027* | 0.012 | *0.011,0.008* | 0.021 | *0.058,0.020* | 0.074 | *0.015,0.010* | 0.011 | *0.008,0.004* | 0.220 | *0.007,0.007* | 0.223 |
| $CaAl_2Si_2O_8$ | 0.887 | *0.018,0.019* | 0.850 | *0.044,0.034* | 0.862 | *0.035,0.027* | 0.866 | *0.026,0.074* | 0.781 | *0.019,0.029* | 0.812 | *0.017,0.052* | 0.744 | *0.010,0.007* | 0.756 |
| $(Fe,Mg)Al_2Si_2O_8$ | 0.013 | *0.021,0.017* | 0.005 | *0.011,0.019* | 0.016 | *0.017,0.014* | 0.016 | *0.006,0.014* | 0.007 | *0.001,0.013* | 0.014 | *0.010,0.020* | 0.011 | *0.010,0.008* | 0.012 |
| $[\ ]Si_4O_8$ | 0.037 | *0.020,0.030* | 0.040 | *0.044,0.032* | 0.043 | *0.023,0.019* | 0.034 | *0.033,0.032* | 0.072 | *0.018,0.014* | 0.077 | *0.061,0.018* | 0.007 | *0.008,0.006* | −0.005 |
| normalized An(d) | 0.993 | *0.006,0.006* | 0.958 | *0.031,0.059* | 0.986 | *0.009,0.052* | 0.976 | *0.022,0.066* | 0.914 | *0.009,0.018* | 0.987 | *0.007,0.012* | 0.768 | *0.006,0.008* | 0.769 |

| | **Q36** | ± | **Q38** | ± | **Q44** | ± | **M3** | ± | **M6** | ± | **M23** | ± | **$An_{95}$ std as unk** | ± | **$An_{95}$ std value$^{(f)}$** |
|---|---|---|---|---|---|---|---|---|---|---|---|---|---|---|---|
| **wt. %** | | | | | | | | | | | | | | | |
| $SiO_2$ | 50.29 | *1.74,1.00* | 48.60 | *0.58,0.66* | 49.28 | *1.25,1.25* | 48.01 | *0.28,0.36* | 47.05 | *1.70,1.12* | 47.66 | *0.66,0.81* | 44.31 | *0.31,0.42* | 44.00 |
| $Al_2O_3$ | 30.03 | *1.10,1.55* | 31.42 | *0.60,0.54* | 31.86 | *0.61,0.93* | 32.60 | *0.20,0.65* | 32.35 | *1.07,0.83* | 31.32 | *0.97,0.43* | 35.33 | *0.42,0.32* | 36.03 |
| FeO | 0.40 | *0.34,0.16* | 0.52 | *0.63,0.31* | 0.28 | *0.20,0.10* | 0.64 | *0.35,0.29* | 0.44 | *0.86,0.32* | 0.42 | *0.61,0.20* | 0.45 | *0.07,0.10* | 0.62 |
| MgO | 0.90 | *0.39,0.28* | 1.08 | *0.30,0.14* | 0.89 | *0.12,0.10* | 0.56 | *0.10,0.06* | 0.90 | *0.16,0.15* | 1.01 | *0.22,0.24* | 0.06 | *0.01,0.03* | 0.02 |
| CaO | 16.61 | *0.74,0.88* | 18.33 | *0.40,0.66* | 17.80 | *0.63,0.94* | 16.57 | *0.30,0.28* | 18.64 | *0.65,0.59* | 18.14 | *0.65,1.30* | 19.07 | *0.16,0.21* | 19.09 |
| $Na_2O$ | 1.30 | *0.79,0.36* | 0.23 | *0.24,0.13* | 0.68 | *0.43,0.36* | 2.01 | *0.09,0.03* | 0.34 | *0.26,0.27* | 1.02 | *0.81,0.68* | 0.49 | *0.12,0.04* | 0.53 |
| total | 99.71 | *0.76,0.80* | 100.31 | *0.85,1.11* | 100.79 | *0.15,0.71* | 100.40 | *0.29,1.18* | 99.68 | *0.84,0.87* | 99.66 | *1.15,1.00* | 99.74 | *0.49,0.48* | 100.29 |
| n | 30 | | 24 | | 17 | | 7 | | 28 | | 32 | | 6 | | |
| **cations**$^{(b)}$ | | | | | | | | | | | | | | | |
| Si | 2.308 | *0.070,0.042* | 2.227 | *0.018,0.030* | 2.239 | *0.052,0.044* | 2.199 | *0.023,0.014* | 2.175 | *0.058,0.034* | 2.205 | *0.021,0.039* | 2.056 | *0.006,0.012* | 2.033 |
| Al | 1.623 | *0.045,0.091* | 1.696 | *0.033,0.027* | 1.704 | *0.041,0.053* | 1.758 | *0.013,0.025* | 1.756 | *0.052,0.054* | 1.706 | *0.052,0.025* | 1.931 | *0.014,0.008* | 1.960 |
| Fe2+ | 0.015 | *0.013,0.006* | 0.020 | *0.024,0.012* | 0.011 | *0.008,0.004* | 0.025 | *0.013,0.011* | 0.017 | *0.033,0.012* | 0.016 | *0.024,0.008* | 0.017 | *0.003,0.004* | 0.023 |
| Mg | 0.061 | *0.026,0.019* | 0.074 | *0.020,0.009* | 0.060 | *0.008,0.007* | 0.038 | *0.007,0.004* | 0.062 | *0.011,0.011* | 0.070 | *0.014,0.017* | 0.004 | *0.001,0.002* | 0.001 |
| Ca | 0.816 | *0.037,0.044* | 0.900 | *0.020,0.036* | 0.865 | *0.031,0.048* | 0.812 | *0.014,0.007* | 0.922 | *0.030,0.037* | 0.898 | *0.033,0.069* | 0.947 | *0.007,0.016* | 0.944 |
| Na | 0.116 | *0.070,0.033* | 0.020 | *0.021,0.012* | 0.060 | *0.037,0.032* | 0.178 | *0.008,0.003* | 0.030 | *0.023,0.024* | 0.091 | *0.072,0.061* | 0.044 | *0.011,0.004* | 0.047 |
| total | 4.939 | *0.031,0.040* | 4.936 | *0.016,0.010* | 4.939 | *0.013,0.010* | 5.011 | *0.009,0.010* | 4.962 | *0.026,0.024* | 4.987 | *0.034,0.038* | 5.000 | *0.006,0.005* | 5.010 |
| **endmembers**$^{(c)}$ | | | | | | | | | | | | | | | |
| $Ca(Fe,Mg)Si_3O_8$ | 0.070 | *0.035,0.018* | 0.078 | *0.019,0.015* | 0.057 | *0.017,0.010* | 0.043 | *0.013,0.004* | 0.069 | *0.024,0.021* | 0.088 | *0.017,0.013* | 0.013 | *0.006,0.009* | 0.006 |
| $NaAlSi_3O_8$ | 0.116 | *0.070,0.033* | 0.020 | *0.021,0.012* | 0.060 | *0.037,0.032* | 0.178 | *0.008,0.003* | 0.030 | *0.023,0.024* | 0.091 | *0.072,0.061* | 0.044 | *0.011,0.004* | 0.047 |
| $CaAl_2Si_2O_8$ | 0.746 | *0.024,0.058* | 0.822 | *0.019,0.032* | 0.808 | *0.024,0.049* | 0.770 | *0.007,0.012* | 0.853 | *0.028,0.041* | 0.810 | *0.037,0.061* | 0.934 | *0.008,0.007* | 0.938 |
| $(Fe,Mg)Al_2Si_2O_8$ | 0.007 | *0.004,0.018* | 0.016 | *0.012,0.019* | 0.014 | *0.012,0.014* | 0.020 | *0.003,0.021* | 0.010 | *0.021,0.015* | −0.003 | *0.018,0.019* | 0.008 | *0.101,0.007* | 0.019 |
| $[\ ]Si_4O_8$ | 0.061 | *0.047,0.025* | 0.064 | *0.015,0.009* | 0.061 | *0.018,0.010* | −0.011 | *0.012,0.001* | 0.038 | *0.025,0.024* | 0.013 | *0.042,0.026* | 0.001 | *0.007,0.003* | −0.010 |
| normalized An$^{(d)}$ | 0.866 | *0.034,0.073* | 0.976 | *0.011,0.026* | 0.931 | *0.035,0.044* | 0.812 | *0.002,0.010* | 0.966 | *0.027,0.026* | 0.899 | *0.069,0.080* | 0.955 | *0.004,0.012* | 0.952 |

[(a)] uncertainties represent the range of measured values;

[(b)] normalized to 8 oxygens;

[(c)] endmembers are calculated following the methods from Beaty and Albee (1980) *(d):* normalized to reported $NaAlSi_3O_8$ and $CaAl_2Si_2O_8$ endmembers;

*(e):* value reported in Gilbert et al. (2003) with corrected $SiO_2$;

*(f):* value reported in Jarosewich (1980); $K_2O$ (not shown) is 0.07 wt. %

*: averaged $K_2O$ values for the $An_{78}$ standard are 0.08 wt. %; all other $TiO_2$, $Cr_2O_3$, MnO, and $K_2O$ data are below detection limits.

## Table 2.

Al-Mg istotope systematics of QUE 99177,49 and MET 00426,46 chondrules.

| chondrule | spot/phase | $^{27}$Al/$^{24}$Mg (2SE) | *δ$^{26}$Mg (2SE) |
|---|---|---|---|
| Q7. | 1. Pl | 44.11 ± 0.31 | 0.92 ± 0.91 |
| Mg#: 99.0 (+0.2,−0.1)(a) | 2. Pl | 44.05 ± 0.31 | 1.22 ± 0.87 |
| Δ$^{17}$O: −5.2 (± 0.5)‰(b) | 3. Pl | 46.11 ± 0.33 | 1.15 ± 0.94 |
| isochron MSWD: 0.2 | 4. Pl | 37.80 ± 0.27 | 1.57 ± 1.24 |
| *δ$^{26}$Mg$_0$: 0.04 ± 0.04 | 5. Pl | 39.37 ± 0.27 | 1.06 ± 1.07 |
| ($^{26}$Al/$^{27}$Al)$_0$: (3.5 ± 1.3) × 10$^{-6}$ | 6. Pl | 40.61 ± 0.28 | 0.87 ± 0.89 |
| Myr after CAIs: 2.8 (−0.3/+0.5) | 7. LPx | 0.0230 ± 0.00230(c) | 0.02 ± 0.07 |
| | 8. LPx | 0.0298 ± 0.00298 | 0.05 ± 0.07 |
| | 9. Ol | 0.0004 ± 0.00004 | 0.03 ± 0.08 |
| | 10. Ol | 0.0003 ± 0.00003 | 0.05 ± 0.08 |
| Q13. | 1. Pl | 37.44 ±0.14 | 0.78 ± 1.02 |
| Mg#: 98.4 (+0.2,−0.2) | 2. Pl | 37.81 ±0.20 | 0.28 ± 0.93 |
| Δ$^{17}$O: −1.9 (± 0.6)‰ | 3. Pl | 34.84 ±0.13 | 0.46 ± 0.84 |
| isochron MSWD: 1.6 | 4. Pl | 31.78 ±0.15 | −0.34 ± 1.11 |
| *δ$^{26}$Mg$_0$: 0.01 ± 0.04 | 5. Ol | 0.0017 ±0.00017 | −0.02 ± 0.08 |
| ($^{26}$Al/$^{27}$Al)$_0$: (1.3 ± 1.7) × 10$^{-6}$ | 6. Ol | 0.0027 ±0.00027 | −0.07 ± 0.08 |
| Myr after CAIs: >2.9 | 7. LPx | 0.0281 ±0.00281 | 0.05 ± 0.07 |
| | 8. LPx | 0.0341 ±0.00341 | 0.06 ± 0.07 |
| Q15. | 1. Pl | 35.77 ±0.25 | 0.04 ± 0.96 |
| Mg#: 98.6 (+0.1,−0.3) | 2. Pl | 34.48 ±0.14 | −0.29 ± 0.93 |
| Δ$^{17}$O: −2.8 (± 0.5)‰ | 3. Pl | 38.15 ±0.14 | 0.83 ± 1.03 |
| isochron MSWD: 1.0 | 4. Pl | 36.59 ±0.26 | −0.20 ± 0.96 |
| *δ$^{26}$Mg$_0$: 0.00 ± 0.04 | 5. Pl | 34.36 ±0.24 | −0.89 ± 1.05 |
| ($^{26}$Al/$^{27}$Al)$_0$: (−0.3 ± 1.7) × 10$^{-6}$ | 6. LPx | 0.0149 ±0.00149 | 0.02 ± 0.07 |
| Myr after CAIs: >3.7 | 7. LPx | 0.0276 ±0.00276 | −0.01 ± 0.06 |
| | 8. Ol | 0.0007 ±0.00007 | −0.02 ± 0.08 |
| | 9. Ol | 0.0017 ±0.00017 | −0.02 ± 0.08 |
| Q16. | 1. Pl | 39.47 ±0.27 | 1.38 ± 1.01 |
| Mg#: 99.0 (+0.2,−0.3) | 2. Pl | 37.96 ±0.26 | 1.97 ± 1.16 |
| A$^{17}$O: −5.0 (± 0.6)‰ | 3. Pl | 36.16 ±0.25 | 1.28 ± 1.20 |
| isochron MSWD: 0.4 | 4. Pl | 37.45 ±0.26 | 1.43 ± 0.87 |
| *5$^{26}$Mg$_0$: 0.04 ± 0.01 | 5. Pl | 41.72 ±0.29 | 1.21 ± 1.05 |
| ($^{26}$Al/$^{27}$Al)$_0$: (5.2 ± 1.7) × 10$^{-6}$ | 6. Ol | 0.0003 ±0.00003 | 0.00 ± 0.08 |
| Myr after CAIs: 2.4 (−0.3/+0.4) | 7. Ol | 0.0003 ±0.00003 | −0.02 ± 0.08 |
| | 8. LPx | 0.0286 ±0.00286 | 0.04 ± 0.06 |
| | 9. LPx | 0.0166 ±0.00166 | 0.00 ± 0.06 |
| Q19. | 1. Pl | 30.13 ±0.31 | 0.54 ± 1.04 |

| **chondrule** | **spot/phase** | **$^{27}$Al/$^{24}$Mg (2SE)** | ***δ$^{26}$Mg (2SE)** |
|---|---|---|---|
| Mg#: 98.7 (+0.7,−0.8) | 2. Pl | 36.57 ±0.14 | 0.63 ± 1.16 |
| Δ$^{17}$O: −4.9 (± 0.9)‰ | 3. Pl | 37.70 ±0.14 | 0.15 ± 1.17 |
| isochron MSWD: 0.3 | 4. Pl | 33.71 ±0.17 | 0.37 ± 1.15 |
| *δ$^{26}$Mg$_0$: 0.00 ± 0.04 | 5. Pl | 34.93 ±0.27 | −0.16 ± 1.32 |
| ($^{26}$Al/$^{27}$Al)$_0$: (1.2 ± 2.0) × 10$^{-6}$ | 6. Pl | 35.98 ±0.19 | 0.03 ± 1.24 |
| Myr after CAIs: >2.9 | 7. Ol | 0.0014 ±0.00014 | −0.04 ± 0.13 |
| | 8. Ol | 0.0014 ±0.00014 | −0.06 ± 0.13 |
| | 9. LPx | 0.0175 ±0.00175 | 0.01 ± 0.06 |
| | 10. LPx | 0.0234 ±0.00234 | 0.00 ± 0.07 |
| Q35. | 1. Pl | 24.82 ±0.18 | −0.37 ± 1.25 |
| Mg#: 98.3 (+0.2,−0.3) | 2. Pl | 28.11 ±0.23 | −0.71 ± 1.28 |
| Δ$^{17}$O: −2.1 (± 0.8‰ | 3. Pl | 26.57 ±0.19 | 0.76 ± 1.51 |
| isochron MSWD: 1.0 | 4. Pl | 25.35 ±0.11 | 0.61 ± 1.11 |
| *δ$^{26}$Mg$_0$: −0.04 ± 0.05 | 5. Pl | 26.07 ±0.09 | −0.58 ± 0.72 |
| ($^{26}$Al/$^{27}$Al)$_0$: (−1.0 ± 2.5) × 10$^{-6}$ | 6. Ol | 0.0003 ±0.00003 | −0.06 ± 0.13 |
| Myr after CAIs: >3.6 | 7. Ol | 0.0003 ±0.00003 | −0.01 ± 0.13 |
| | 8. LPx | 0.0742 ±0.00742 | −0.04 ± 0.06 |
| Q36. | 1. Pl(d) | 33.95 ±0.33 | −0.52 ± 1.33 |
| Mg#: 97.4 (+0.7,−0.9) | 2. Pl | 30.31 ±0.22 | −0.32 ± 1.78 |
| Δ$^{17}$O: −1.7 (± 0.3)‰ | 3. Pl(d) | 32.89 ±0.12 | −0.01 ± 1.86 |
| isochron MSWD: 0.2 | 4. Pl | 32.45 ±0.23 | −0.88 ± 1.62 |
| *δ$^{26}$Mg$_0$: −0.01 ± 0.04 | 5. Ol | 0.0014 ±0.00014 | 0.02 ± 0.13 |
| ($^{26}$Al/$^{27}$Al)$_0$: (−2.0 ± 3.3) × 10$^{-6}$ | 6. LPx | 0.0238 ±0.00238 | −0.02 ± 0.06 |
| Myr after CAIs: >3.7 | 7. LPx | 0.0139 ±0.00139 | 0.01 ± 0.06 |
| | 8. Ol | 0.0023 ±0.00023 | −0.03 ± 0.13 |
| Q38. | 1. Pl | 28.98 ±0.11 | 1.62 ± 1.11 |
| Mg#: 99.0 (+0.1,−0.2) | 2. Pl | 31.86 ±0.12 | 1.40 ± 1.30 |
| Δ$^{17}$O: −5.3 (± 0.8)‰ | 3. Pl | 30.94 ±0.15 | 1.88 ± 0.97 |
| isochron MSWD: 2.1 | 4. Pl | 27.36 ±0.10 | 1.15 ± 1.12 |
| *δ$^{26}$Mg$_0$: −0.03 ± 0.07 | 5. Pl | 31.08 ±0.13 | 0.26 ± 1.04 |
| ($^{26}$Al/$^{27}$Al)$_0$: (6.0 ± 3.9) × 10$^{-6}$ | 6. Ol | 0.0006 ±0.00006 | −0.01 ± 0.12 |
| Myr after CAIs: 2.2 (−0.5/+1.1) | 7. Ol | 0.0004 ±0.00004 | 0.13 ± 0.12 |
| | 8. LPx | 0.0189 ±0.00189 | −0.05 ± 0.07 |
| | 9. LPx | 0.0317 ±0.00317 | −0.06 ± 0.06 |
| Q44. | 1. Pl | 37.51 ±0.26 | −0.27 ± 1.43 |
| Mg#: 98.3 (+0.2,−0.2) | 2. Pl | 31.65 ±0.12 | −0.18 ± 0.82 |
| Δ$^{17}$O: −2.4 (± 0.5)% | 3. Pl | 35.69 ±0.15 | 0.48 ± 1.35 |
| isochron MSWD: 0.7 | 4. Pl | 32.25 ±0.23 | 0.02 ± 1.54 |
| *δ$^{26}$Mg$_0$: 0.02 ± 0.04 | 5. Pl | 33.69 ±0.24 | −1.04 ± 1.36 |
| ($^{26}$Al/$^{27}$Al)$_0$: (−0.9 ± 2.2) × 10$^{-6}$ | 6. LPx | 0.0230 ±0.00230 | 0.00 ± 0.06 |

| chondrule | spot/phase | $^{27}$Al/$^{24}$Mg (2SE) | *δ$^{26}$Mg (2SE) |
|---|---|---|---|
| Myr after CAIs: >3.7 | 7. LPx | 0.0277 ±0.00277 | 0.05 ± 0.06 |
|  | 8. LPx | 0.0239 ±0.00239 | 0.01 ± 0.06 |
| M3. | 1. Pl | 49.10 ±0.25 | −0.08 ± 1.01 |
| Mg#: 94.2 (+1.0,−0.7) | 2. Pl | 51.11 ±0.25 | 0.74 ± 1.02 |
| Δ$^{17}$O: −0.9 (± 0.4)‰ | 3. Pl | 56.20 ±0.44 | −1.30 ± 1.43 |
| isochron MSWD: 1.2 | 4. Pl | 53.74 ±0.36 | 0.12 ± 1.25 |
| *δ$^{26}$Mg$_0$: 0.04 ± 0.06 | 5. Pl | 62.24 ±0.32 | 0.68 ± 1.42 |
| ($^{26}$Al/$^{27}$Al)$_0$: (0.2 ± 1.4) × 10$^{-6}$ | 6. LPx | 0.0466 ±0.00466 | −0.01 ± 0.10 |
| Myr after CAIs: >3.6 | 7. LPx | 0.0287 ±0.00287 | 0.05 ± 0.10 |
|  | 8. LPx | 0.0439 ±0.00439 | 0.04 ± 0.10 |
| M6. | 1. Pl | 38.90 ±0.21 | 0.69 ± 1.15 |
| Mg#: 99.0 (+0.1,−0.1) | 2. Pl | 37.16 ±0.21 | 1.03 ± 1.07 |
| Δ$^{17}$O: −4.2 (± 0.6)‰ | 3. Pl | 37.65 ±0.20 | 1.71 ± 1.05 |
| isochron MSWD: 0.5 | 4. Pl | 37.59 ±0.19 | 1.42 ± 0.94 |
| *δ$^{26}$Mg$_0$: 0.04 ± 0.04 | 5. Pl | 39.77 ±0.21 | 0.65 ± 1.08 |
| ($^{26}$Al/$^{27}$Al)$_0$: (4.0 ± 1.7) × 10$^{-6}$ | 6. Ol | 0.0007 ±0.00007 | 0.05 ± 0.08 |
| Myr after CAIs: 2.6 (−0.4/+0.6) | 7. Ol | 0.0013 ±0.00013 | 0.04 ± 0.08 |
|  | 8. LPx | 0.0163 ±0.00163 | 0.04 ± 0.08 |
|  | 9. LPx | 0.0265 ±0.00265 | 0.03 ± 0.07 |
| M23. | 1. Pl | 30.76 ±0.16 | 0.95 ± 0.90 |
| Mg#: 99.2 (+0.1,−0.1) | 2. Pl | 28.89 ±0.14 | 1.07 ± 0.76 |
| Δ$^{17}$O: −4.7 (± 0.4)% | 3. Pl | 29.89 ±0.16 | 1.88 ± 0.91 |
| isochron MSWD: 0.7 | 4. Pl | 30.54 ±0.34 | 1.36 ± 0.85 |
| *δ$^{26}$Mg$_0$: 0.00 ± 0.08 | 5. Pl(d) | 31.54 ±0.20 | 1.23 ± 1.86 |
| ($^{26}$Al/$^{27}$Al)$_0$: (6.0 ± 2.0) × 10$^{-6}$ | 6. Ol | 0.0004 ±0.00004 | −0.01 ± 0.08 |
| Myr after CAIs: 2.2 (−0.3/+0.4) |  |  |  |

(a) bracketed values represent the range of measured Mg#s, as reported in Tenner et al. (2015).

(b) bracketed values are the 2SD of multiPle measurements per chondrule used to define the averaged "host" chondrule Δ$^{17}$O, as reported in Tenner et al. (2015)

(c) $^{27}$Al/$^{24}$Mg uncertainties are estimated as 10% of the reported value.

See main text for details

(d) analyses inadvertantly profiled into high-Ca pyroxene grains. As a result, fewer Plagioclase cycles were used to determine $^{27}$Al/$^{24}$Mg and *δ$^{26}$Mg (215, 151, and 96 cycles for Q36 #'s 1 & 3, and M23 #5, respectively).